EPFL

Photo- and Thermally- induced Effects on the Absorption Spectroscopy of Au/SiO$_2$ and Au/TiO$_2$ Core-shell Nanoparticles

Lijie WANG

École
polytechnique
fédérale
de Lausanne

2022

Acknowledgments

First of all, I would like to thank Prof. Majed Chergui who trained me well during the past four years as my supervisor. Since I made a big jump from material science to ultrafast spectroscopy during the PhD, my learning process was so slow in the beginning but Majed did not give up on me and instead, he encouraged me all the time and patiently taught me even the very smallest details, including language problems. Gradually, I had experience on the laser set-up and data analysis, and gained the ability to analyse 'ultrafast data' quickly and proficiently. But the most important thing I learned from Majed is that the attitudes, methods and habits to scientific research, doing research is not simply publishing papers like I used to think, and is not a 'cooking' of different trying to make product better without understanding. The nature of doing science is to seek truth based on observable evidences, we may make mistakes but we have to be honest and respect objective results. I do not know how to describe my gratitude to Majed, he guided me at this critical stage of my life, there is an old saying in China 'a teacher for a day is a father for a lifetime' may represent this feeling.

During my PhD life, I would like to thank Dr. Malte Oppermann, Dr. Thomas Rossi, Dr. Michele Puppin, Dr. Lars Mewes and Dr. Benjamin Bauer for the help and nice discussions on the laser-setups, they taught me how to do laser experiments basically hand by hand and share with me useful literature, I always keep asking questions even though some questions are silly to them, but they are patient and friendly all the time. Secondly, when I was a fresh in the ultrafast field, and first came aboard to Switzerland, many of my colleagues and friends helped me, in this regard, I would like to thank Dr. Christopher Arrell, Dr. Edoardo Baldini, Dr. Yang Zhao, Dr. Tania Palmeri, Dr. Natalia Nagornova, Dr. Rebecca Ingle, Dr. Oliviero Cannelli, Mr. Huiyuan Chen, Dr. Ludmila Leroy, Dr. Luca Longetti, Dr. Serhii Polishchuk, Dr. Rolf Versteeg etc. Practically, Dr. Benjamin Bauer also helped me a lot in daily life, when I moved to a small town in canton Bern where many people only speak German, he did many translation work and making phone calls for my personal issues. A special thank to my officemate Dr. Katrin Oberhofer who is always nice and with special German temperament that I like very much. Additional thanks to our secretary Annick Gaudin who nearly took all the responsibly of LSU except for research work, she even helped me to look for living places when I was not familiar with Swiss life. Anyway, thanks to all LSU members, for the help and great time we spent together.

I would also like to thank my external collaborators during the PhD, Prof. Jianfang Wang, Dr. Tsz Him Chow from the Chinese University of Hong Kong who kindly provide the core-shell nanoparticles to me. Dr. Michele Magnozzi from the University of Genova who provides the measurements of temperature-dependent dielectric function on gold nanoparticles. They ensured that my PhD project went well during the past years.

Lausanne, 20th July 2021 Lijie Wang

Résumé

Les électrons générés par l'amortissement de Landau de l'excitation plasmonique sur les nanoparticules d'or peuvent être injectés dans un semi-conducteur adjacent, par exemple le TiO_2 anatase, ce qui améliore les capacités de récolte de la lumière des dispositifs de conversion de l'énergie solaire. La compréhension des processus d'injection d'électrons est cruciale pour l'optimisation des dispositifs. La première étape consiste à comprendre la nanoparticule d'or nue elle-même. Nous présentons donc des études d'absorption transitoire ultrarapide de nanoparticules d'or de ~25 nm de diamètre excitées par des plasmons de surface en solution, en surveillant la réponse de résonance plasmonique de surface dans le visible (1.7-3.0 eV) ainsi que les transitions inter et intra-bandes dans l'UV proche à profond (3.4-4.5 eV). Cependant, afin de distinguer les effets thermiques dans le spectre d'absorption des nanoparticules d'or, nous présentons des spectres d'absorption en fonction de la température (de la température ambiante à 80 °C) de nanoparticules Au/SiO_2 à cœur-coquille (diamètre du cœur : ~25 nm) dans la plage de 1.5 eV à 4.5 eV, qui englobe la résonance plasmonique de surface localisée et les transitions interbandes. Les changements des spectres d'absorption sont bien reproduits par des calculs théoriques basés sur la dépendance de la température mesurée expérimentalement de la partie réelle (ε_1) et imaginaire (ε_2) de la constante diélectrique des nanoparticules d'or. Nous comparons également les résultats aux spectres d'absorption transitoire photo-induits ultra-rapides lors de l'excitation de la bande plasmonique, et nous concluons que si la bande plasmonique peut être utilisée pour surveiller le chauffage des nanoparticules, la région interbande est peu affectée par les effets thermiques et est dominée par les effets électroniques. Nos résultats transitoires sur les nanoparticules d'or sondées par UV profond montrent qu'après les processus initiaux ultrarapides de diffusion électron-électron et électron-phonon, les électrons chauds de faible énergie au-dessus du niveau de Fermi restent en équilibre avec le réseau chaud pendant des dizaines ou des centaines de secondes. Ensuite, nous étudions le transfert et la relaxation des porteurs de charge photo-induits dans Au/TiO_2, nos résultats montrent que le blanchiment à la résonance d'extraction dans Au/TiO_2 a une vitesse de décroissance lente significative lors de l'excitation plasmonique, et son intensité d'absorption transitoire à long délai donne une dépendance quadratique de la fluence d'excitation, ce qui implique l'apparition d'une absorption à deux photons dans le TiO_2 anatase qui est renforcée par la résonance plasmonique de surface. De plus, dans les NPs Au/SiO_2 et Au/TiO_2, nous observons pour la première fois des vibrations acoustiques dans la région UV, mais avec des fréquences d'oscillation significativement différentes qui ont été attribuées aux différentes propriétés élastiques de la coquille.

Mots clés : Transient absorption spectroscopy ; Au/SiO_2 nanoparticles ; Au/TiO_2 nanoparticles ; electron injection ; two-photon absorption ; charge carrier relaxation ; thermal effects ; acoustic vibrations.

Abstract

Electrons generated by Landau damping of the plasmon excitation on gold nanoparticles that can be injected into an adjacent semiconductor e.g. anatase TiO_2, enhancing the light harvesting capabilities of solar energy conversion devices. The understanding of the electron injection processes is crucial for the optimization of the devices. The first step is to have a understanding of the bare gold nanoparticle itself, we thus report on ultrafast transient absorption studies of surface plasmon-excited ~25 nm diameter gold nanoparticles in solution, monitoring the surface plasmon resonance response in the visible (1.7-3.0 eV) as well as the inter- and intra-band transitions in the near-to-deep-UV (3.4-4.5 eV). However, in order to distinguish the thermal effects in absorption spectrum on gold NPs, we present temperature-dependent (from room temperature to 80 °C) absorption spectra of Au/SiO_2 core-shell nanoparticles (core diameter: ~25 nm) in the range from 1.5 eV to 4.5 eV, which encompasses the localized surface plasmon resonance and the interband transitions. The changes of absorption spectra are well reproduced by theoretical calculations based on the experimentally measured temperature-dependence of the real (ε_1) and imaginary (ε_2) part of the gold nanoparticle dielectric constant. We also compare the results to ultrafast photo-induced transient absorption spectra upon excitation of the plasmon band, and conclude that while the plasmon band can be used to monitor the heating of the nanoparticles, the interband region is little affected by thermal effects and is dominated by electronic ones. Our deep-UV probed transient results on gold nanoparticles show that after the initial ultrafast electron-electron and electron-phonon scattering processes, low-energy hot electrons above the Fermi level remain in equilibrium with the hot lattice for tens to hundreds of ps. Then we investigate the photo-induced charge carrier transfer and relaxation in Au/TiO_2, our results show that the bleach at the excion resonance in Au/TiO_2 has a significant slow decay speed upon plasmon excitation, and its transient absorption intensity at long term decay gives a quadratic dependence on excitation fluence, implying the appearance of two-photon absorption in anatase TiO_2 that enhanced by the surface plasmon resonance of gold nanoparticles. Besides, in the Au/SiO_2 and Au/TiO_2 NPs, we both observe acoustic vibrations in the UV region for the first time but with significantly different oscillation frequencies which were attributed to the different elastic properties of the shell.

Keywords: Transient absorption spectroscopy; Au/SiO_2 nanoparticles; Au/TiO_2 nanoparticles; electron injection; two-photon absorption; charge carrier relaxation; thermal effects; acoustic vibrations.

Contents

List of Figures

List of Tables

List of Acronyms

Localized surface plasmon resonance (LSPR)

Conduction band (CB)

Ultraviolet (UV)

Surface-enhanced Raman scattering (SERS)

Second harmonic generation (SHG)

Gold nanoparticles (Au NPs)

Face-centered cubic (fcc)

Valance band (VB)

Infrared (IR)

Temperature (T)

Transient absorption (TA)

Photovoltaic conversion efficiency (PCE)

Dye sensitized TiO_2 solar cell (DSSC)

Electron transfer (ET)

Metal-to-ligand charge transfer (MLCT)

Ground state bleaching (GSB)

Stimulate emission (SE)

Excited state absorption (ESA)

Non-collinear Optical Parametric Amplifier (NOPA)

Achromatic doubling (AD)

Beam splitter (BS)

Multi-layer Mirror (MM)

Chirped mirror (CM)

Spherical mirror (SM)

Off-axis parabolic mirror (PM)

Full-width half-maximum (FWHM)

Instrument response function (IRF)

Cross-phase modulation (CPM)

Group Velocity Dispersion (GVD)

Fermi level (E_F)

Density functional theory (DFT)

Local density approximation (LDA)

Generalized gradient approximation (GGA)

Angle-resolved photoelectron spectroscopy (ARPES)

X-ray scattering (XRS)

X-ray absorption spectroscopy (XAS)

Transition metal oxide (TMO)

Terahertz (THz)

Band gap (BG)

X-ray photoelectron spectroscopy (XPS)

Second harmonic generation (SHG)

Two-photon absorption (TPA)

Fast Fourier Transform (FFT)

Density of states (DOS)

Femtosecond (fs)

Nanosecond (ns)

Picosecond (ps)

Free electron lasers (FELs)

Room temperature (RT)

Introduction

Gold nanoparticles (Au NPs) have attracted wide interests in decades due to their potential applications in areas ranging from photovoltaics, photocatalysis to medical imaging and cancer therapy. The key aspect is the exploitation of the intense localized surface plasmon resonance (LSPR) absorption band in the visible range and the physical phenomena ensuing its excitation. After light absorption, plasmon resonances can be damped radiatively by re-emission of a photon or non-radiatively through the creation of hot electron-hole pairs via Landau damping. Landau damping is a pure quantum mechanical process in which a plasmon quantum is transferred into a single electron–hole pair excitation on sub-femtosecond (fs) timescale. The plasmon-induced electric field, which represents a time-dependent perturbation on the conduction band (CB) electrons of Au NPs, can induce transitions of electrons from occupied to unoccupied states.

Ultrafast spectroscopic methods have proved to be powerful tools to characterize the charge carrier (i.e. electrons and holes) generation and transfer in fs to nanosecond (ns) regimes. The Au NPs have already been intensely studied in the visible spectral region by probing the LSPR band. The general picture emerges is that after photoexcitation, electron-electron scattering takes place in hundreds of fs, then energy transfer to lattice via electron-phonon coupling in 2-5 ps. Finally, energy dissipation to the environment occurs in tens to hundreds of picosecond (ps). Therefore, probing the LSPR band provides a thermometer of the Au NPs, because the response are mostly governed by the temperature-induced change of dielectric function. In order to monitor the actual charge carriers, we extended the probe to the high-energy interband transitions in the ultraviolet (UV) region. In addition, disentangling the light- and thermal-induced effects is also curial in the time-resolved transient absorption (TA) experiments. Based on temperature-dependent steady-state absorption measurements and temperature-dependent dielectric properties, we are able to distinguish the electronic from thermal effects and give a qualitative assessment of the thermal response in TA spectroscopy.

In photovoltaics, Au NPs significantly increase the photo-energy conversion efficiency (PCE) as photosensitizer of transition metal oxides (TMOs), such as anatase TiO_2, ZnO and SnO_2. TMOs absorb light in the UV region, which accounts for less than 5% of the overall solar spectrum, while Au NPs can generate hot charge carriers upon absorbing visible light and then transfer electrons to the TMO substrate. Hence, understanding photo-induced charge transfer processes and the mechanisms in Au/TiO_2 is another key point in this dissertation.

Chapter 1 introduces the basic concepts of Au NPs and anatase TiO_2, aim to give a description of the background and motivation behind the proposed study. It discusses the advantages and disadvantages of the choice of materials, the unsolved problems concerning sensitized TiO_2 and the way we are going to investigate them. The potential applications are also mentioned, which are directly related to their physical, chemical and optical properties.

Chapter 2 reviews the current research from the literature, it focuses on the transient studies of Au NPs and Au/TiO$_2$, as well as the temperature effects in TA experiments. The available studies are only limited to the region from the visible to infrared (IR).

Chapter 3 describes the set-ups and the basic principles of TA spectroscopy. The visible TA set-up is designed to perform visible-pump/broadband visible-probe measurements. The deep-UV TA set-up has the ability to generate broadband UV probe light in the region of 260-360 nm where the interband transitions of Au and exciton resonance of anatase TiO$_2$ located. The pump pulses are tuneable from UV to visible spectral region. This chapter also depicts sample preparations and data treatment methods, e.g. determination of instrument response function (IRF), kinetic trace fitting etc.

Chapter 4 shows the TA results on Au NPs probed in the interband transition region. We present both visible and UV TA results and analyse the latter based on a band structure diagram of bulk Au. While the LSPR band reflects a thermal evolution of the NP lattice, probing the interband transitions maps the photo-excited electrons and holes above and below the Fermi level (E$_F$) as well as their relaxation. It is interesting to find that the relaxation of the charge carriers is slow in 150-180 ps timescale, and is commensurate with lattice thermal relaxation.

Chapter 5 investigates the light- and thermally- induced effects in absorption spectra on Au NPs. We firstly present experimental temperature-dependent steady-state absorption results and then compare them with the calculated differential absorption spectra which are based on the temperature-dependent dielectric function of Au NPs. The good agreement between the experimental data and calculations leads us to further compare the response exclusively due to temperature and the transient response in time-resolved experiments. We conclude that the transient behaviour of the LSPR is entirely governed by the temperature effects while the interband transition region is little affected.

Chapter 6 presents the deep-UV TA results on bare anatase TiO$_2$, Au/SiO$_2$ and Au/TiO$_2$ NPs. It shows a bleach with significant long-term decay at the excitonic transition (~3.8 eV) of anatase TiO$_2$ upon visible (below the band gap of TiO$_2$) excitation in Au/TiO$_2$ sample, the fluence dependence measurements implies a two photon process especially visible at long time delay where the signal of bare Au NPs dies away. The ~3.8 eV ultraslow decaying bleach signal is explained in terms of the overlapped contribution between the electron injection from Au core to CB of TiO$_2$ and two-photon excitation in TiO$_2$, in addition, this negative transient signal could be affected by laser heating.

Chapter 7 reports on the coherent acoustic phonons in Au/SiO$_2$ and Au/TiO$_2$ NPs probed via the interband transitions. We present the oscillations ridding on the kinetic signals along with the fits, and compare the oscillation behaviours with the ones probed in LSPR band. The frequency of Au/SiO$_2$ is found to be similar with that of bare Au NPs, while in Au/TiO$_2$ NPs, different oscillation frequency is observed.

Chapter 1 Basic concepts

1.1 Au nanoparticles

In history, Au has played an important role relying on its outstanding qualities among metals, it was used throughout human's development process especially for the royalty due to its shining, yellow characteristic. Pure metallic Au is non-toxic and non-irritating when ingested, it also be used as food component and medicine for hundreds of years. While, the first use of Au particles is intimately related to the history of red-coloured glass in 1400-1300 BCE[1], e. g. the famous *Lycurgus Cup*'s (late Roman, fourth century CE, in British Museum) colour is believed to originate from the presence of 10-30 ppm of Au or Au-Ag alloy particles[2]. Andreas Libavius (1540–1616), a German chemist and physician, mentioned the red colour of Au dissolved in a liquid to make red crystals[3]. In 1852, Michael Faraday first reported the optical properties of Au and other metals to their small size[4], and in 1908, Gustav Mie predicted the optical properties of spherical metal particles, that is, when the size of the Au particle is much smaller than the wavelength of light, an electromagnetic field induces a resonant at a certain frequency, a coherent oscillation of the metal free electrons is generated and called localized surface plasmon resonance (LSPR).

1.1.1 Surface plasmon resonance

Plasmonic metal nanoparticles - including Au, Ag and Cu particles, which are discrete metallic particles that have unique optical properties due to the LSPR. According to the Fermi liquid theory, plasmons can be described as a negatively charged electron cloud coherently displaced from its equilibrium position around a positively charged nuclei[5]. LSPR is a phenomenon in which these conduction band (CB) electrons at the surface of the metals are collective oscillating when their frequency matches that of the incident light electromagnetic radiation, excitation will cause displacements of the electron gas with respect to the equilibrium position around the positively charged nuclei, and only light with frequency in resonance with the oscillation is able to excite the LSPR, thus it shows a strong absorption within certain wavelength located in ultraviolet (UV) or visible region, as illustrated schematically in Figure 1.1. However, excitation of plasmons is not allowed in bulk metals, i.e. below metal skin depth, where plasmon and photon energy dispersion curves never cross each other[6]. The LSPR oscillation frequency depends on several properties: the density of electrons, the shape and size of the charge distribution at the surface, and the effective electron mass, therefore it can be tuned by engineering these factors (see Figure 1.2, shows different LSPR behaviours of plasmonic metal nanoparticles with different sizes, shapes) which enables designs of applications in photovoltaics, biological and chemical sensors etc., taking advantage of the enhanced light absorption at the LSPR. The simplest way to probe the LSPR is by measuring the optical extinction spectrum of the metal particles by steady-state absorption spectroscopy. For instance, the absorption spectrum of a colloidal solution of Au

nanoparticles (NPs) is characterized by an LSPR band at approximately 520 nm, although it is partially superposed to the tail of interband transitions at shorter wavelength.
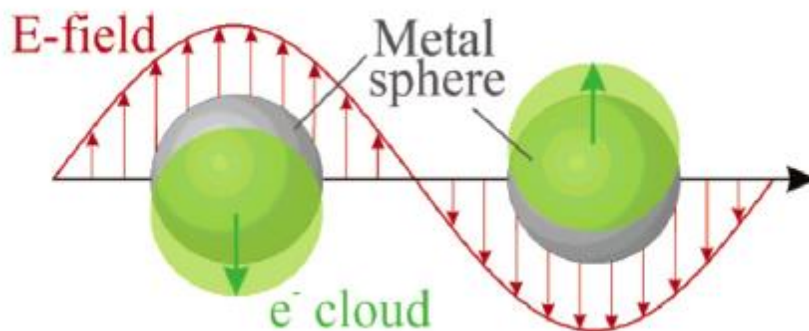
Figure 1.1 Schematic of plasmon oscillation for a nano-sphere particle, showing the displacement of the conduction electron charge cloud relative to the nuclei. Adopted from ref[7].

Of all plasmonic noble metals, in particularly, Au NPs have been attracting attention of researchers because of their electronic structure, structural dynamics, chemical stability, high redox potential, and strongly enhanced and tunable optical properties, which impact the important practical applications, including, for instance, surface-enhanced Raman scattering (SERS)[8,9], fluorescence yield[10], second harmonic generation (SHG)[11], solar energy conversion[12], medical imaging[13–15], etc. Besides, High quality, size controllable and high yield colloidal Au NPs can be quickly prepared by the well-known citrate reduction method[16], in the past decades, Au NPs with different shapes and structure including Au nanosphere, nanorod, nanowire, nanocube etc. all show great modifiability of their optical properties such as absorption and scattering.
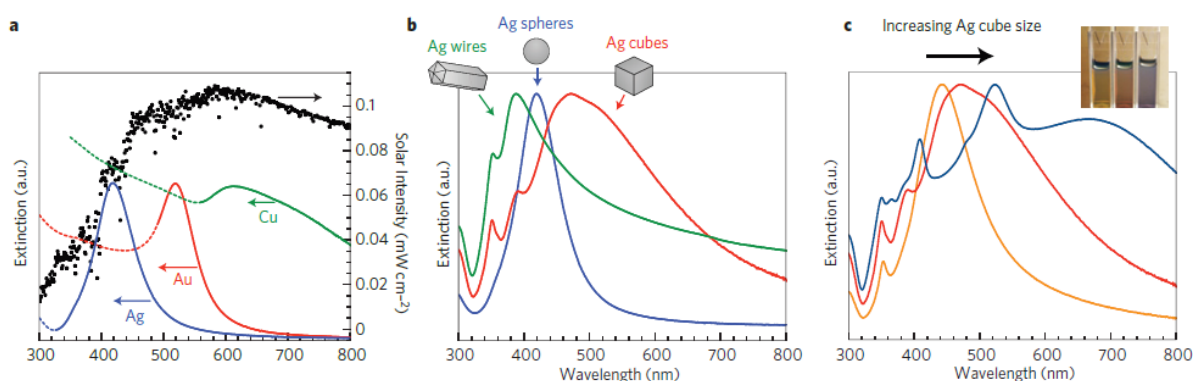
Figure 1.2 a: Normalized extinction spectra of spherical Cu (133 ±23 nm), Ag (38 ±12 nm diameter) and Au (25 ±5 nm) particles. The intensity of solar spectrum is also shown in black; b: Normalized extinction spectra for Ag sphere, cube and wire nanoparticles. Cubic particles are 79 ±12 nm edge length, wire-shaped particles are 90 ±12 nm diameter and >30 aspect ratio, the spherical particles are 38 ±12 nm diameter; c: Normalized extinction spectra for Ag nanocubes as a function of size (56 ±8 nm, 79 ±13 nm and 129 ±7 nm edge lengths correspond to orange, red and blue spectra respectively). The inset shows a photograph of the three nanocube samples suspended in ethanol. Adopted from ref[17].

1.1.2 Physical, chemical and optical properties

Au belongs to the periodic table's group 11 elements and is characterized by a distinct yellow colour, high chemical stability, and high redox potential, which are resulting from its electronic structure and relativistic effects. Bulk Au has excellent resistance to corrosion and high density, it crystallizes in the face-centered cubic (fcc) structure, resulting in its good malleability, the basic physical properties of bulk Au are shown in Table 1.1. The chemical behaviour of Au is mostly determined by the 5d band electrons properties and tendency of Au to acquire an electron for completion of the transition to the 6sp band. Its chemical stability means that Au does not have vigorous reactions with oxygen and sulphur compounds, because of the low stability of Au_2O_3. On the nanoscale, the significant large surface area-to-volume ratio than bulk Au and extremely small dimensions lead to the fact that the overall properties are governed by the surface. When the size of the Au particle is progressively increased/decreased, notable changes in physical properties and chemical reactivity can be observed. Colloidal Au NPs are usually characterized by a red colour (depending on size, shape etc.) which is determined by the electronic structure and LSPR absorption. The response of the Au to electromagnetic radiation contains important information on CB electrons which are highly mobile, bound d-band valence electrons, and the lattice vibrations. The relationship between Au NPs size, concentration and LSPR peak wavelength is given in Table 1.2.

Table 1.1 Physical properties of bulk Au[18]

property	Au
Atomic number	79
Atomic mass (amu)	196.9665
Structure	fcc
Density (g cm^{-3})	19.32
Melting temperature (K)	1337
Conduction electron density (1/cm^3)	5.90×10^{22}
Interband transition threshold (eV)	5d$\rightarrow$6s 1.84
Fermi temperature (K)	6.42×10^4
Heat capacity (J/gK)	0.129

Table 1.2 The relationship between Au nanoparticles size, concentration and LSPR peak wavelength (data from the nanoComposix, https://nanocomposix.com/pages/gold-nanoparticles-physical-properties)

Size (nm)	Mass Concentration (mg/mL)	Atomic Molarity (mmol/L)	Particle Concentration (particle/mL)	Au Mass Percent (%)	Max Optical Density (cm-1)	Peak Wavelength (nm)
5	0.05	0.254	4.0×10^{13}	0.005	0.80	520
10	0.05	0.254	4.9×10^{12}	0.005	0.82	520
20	0.05	0.254	6.2×10^{11}	0.005	0.85	520
30	0.05	0.254	1.8×10^{11}	0.005	1.1	520
40	0.05	0.254	7.7×10^{10}	0.005	1.1	520
50	0.05	0.254	3.9×10^{10}	0.005	1.5	525
100	0.05	0.254	4.9×10^{9}	0.005	1.0	555

The LSPR frequency is essentially determined by many factors and it can be written as:

$$\omega_{LSPR} \approx \sqrt{\frac{n_e e^2 / \epsilon_0 m}{1 + 2\epsilon_m}} = \frac{\omega_p}{\sqrt{1 + 2\epsilon_m}} \qquad \text{Eq. 1.1}$$

Where, ω_p is the plasma frequency of metal, n_e is the number of density of electron, e is the electronic charge, m is the effective mass of the electron, and ϵ_0 and ϵ_m are the permittivity of free space and the surrounding medium, respectively.

And $\omega_p = \frac{4\pi n_e e^2}{m}$ is directly related to the surface electron density. Hence, the LSPR can be adjusted either by changing the shape/size of the NPs: rods, cube, triangle, sphere etc. or changing the surrounding medium the particle.

The Fermi level (E_F) is defined as the surface in k-space, which separate the unoccupied and occupied levels of the CB at zero temperature. The electronic transitions in a medium between these energy levels determine its dielectric function and then the optical properties. In the case of Au metal, however, the energy bands overlap each other, i.e. the CB are partially filled. There is a continuous availability of electrons in these overlapped orbitals.

For the electrons bound to occupied valence band (VB) states, the electrons can jump up from the d-bands below the Fermi level to the CB only when excited by photons with high enough energy, which is the definition of interband transition. The interband transition threshold represents the energy that is required to excite electrons from the topmost 5d band into the 6sp CB (see Figure 1.3), which means that an optical wave corresponding to this energy threshold is able to excite this transition.
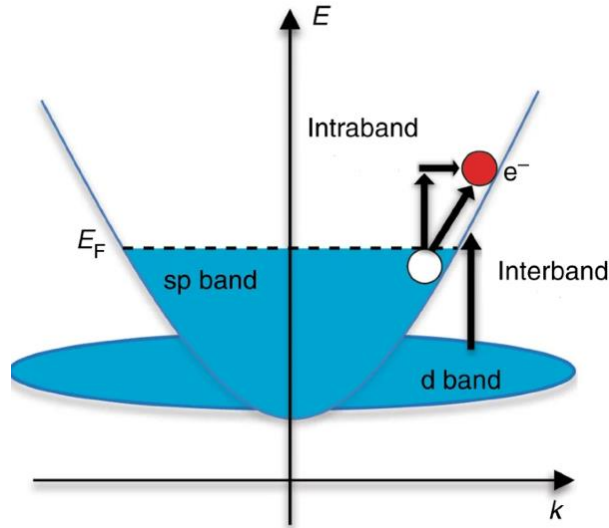
Figure 1.3 Schematic of the energy band structure of Au and its electronic transitions. Arrows indicate an interband transition from the 5d to the 6sp conduction band, and an intraband transition in the conduction band. The creation of an energetic electron (red) and a hole (white) is indicated[19].

1.1.3 Band structure diagram

It is already well established that the 5d-band density of states is larger and more strongly localized near the high symmetry critical points compared to the sp-band, which have a broaden distribution of allowed energy states[20]. In the visible spectral region, there are two different interband transitions, one located near the X symmetry with energy Δ_X of around 1.84 eV, and the other one near the L symmetry with energy gap Δ_L of around 2.3 eV (Figure 1.4). The contribution of X-transition and L-transition to the total absorption of Au is shown in Figure 1.5. Note that the threshold of the actual interband transition is not equivalent to the minimal distance of the energy bands at the X or L symmetry, it is the transition from the d bands to the Fermi level near X or L symmetry[21]. The values obtained from the band structure (BS) calculation and experiment are shown in Table 1.3, which gives the band parameters for optical transitions near L and X points of Brillouin zone.

Briefly, the BS diagram has been calculated for bulk Au by several groups using ab initio many-body perturbation theory at different levels of approximation[20,22,23]. Christensen and Seraphin's model[21] has been widely used as a reference to interpret experiment results. However, the Au BS calculated by density functional theory (DFT) within the local density approximation (LDA) or the generalized gradient approximation (GGA), presents an underestimation of the 5d-6sp interband gap by ~1.0 eV with respect to the available experimental data. In view of this situation, the diagram in Figure 1.4 is calculated using the quasiparticle self-consistent GW scheme[22], which we have selected for our data analysis because it provides the best agreement with angle-resolved photoelectron spectroscopy (ARPES) data on Au crystals[24] and is consistent with the calculation of the Au dielectric function[25]. The absorption coefficient spectrum of bulk Au, which reflects its energy BS, is characterized by several main structures that correspond to interband transitions[26]: the onset of the interband transition is

completely due to transitions from the top of the band 5d to above the E_F. The topmost 5d band below the E_F is shown in red, while the blue one is due to the 6sp band, which spans both the region below and above the E_F. In the meantime, we labelled the energy points from 1 for the first point above the E_F, in increasing order of decreasing energies. The band 3 and 4 to the sp band which occur near X symmetry, namely $X_{4/3} \rightarrow X_1$ (~3.5 eV); the band 2 to band 1 which occurs near L symmetry, namely $L_2 \rightarrow L_1$ (~4.3 eV).
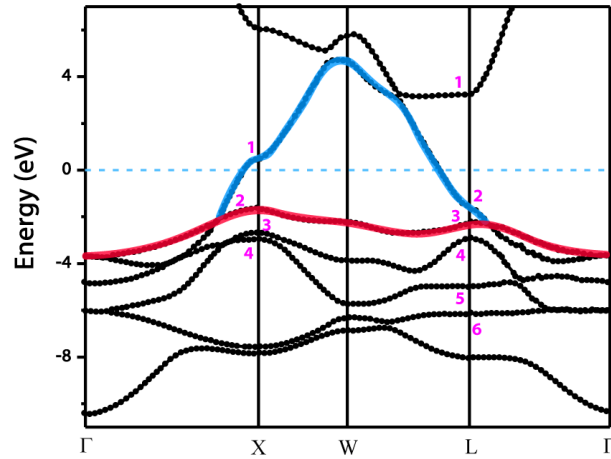
Figure 1.4 Calculated BS diagram of bulk Au[22]. The EF is set to 0 (dashed cyan line). The various critical energy points at the L and X symmetries are numbered starting from the first point above the Fermi level in an increasing order going to lower energies. The red line disentangles the 5d-character topmost occupied band, while the blue line indicates the 6sp band.
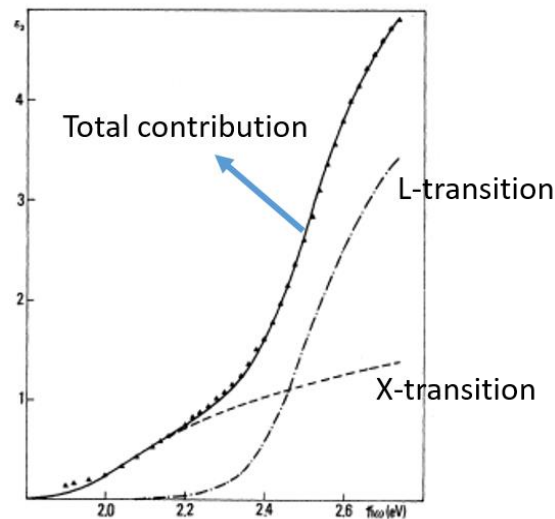
Figure 1.5 Imaginary part of the dielectric constant for Au, dashed line: X-transition contribution; dot-dahsed line: L-transition contribution[25].

Table 1.3 Theoretical and experimental values for the transition energies of bulk Au at the X and L points.

Transition	Assignment	Calc. from BS diagram[22]	ARPES data[24]
X_3-X_1		3.18	
X_4-X_1	d-sub band $\rightarrow$ 6sp	3.50	
X_4-E_F		2.99	
L_5-L_2	d-sub band $\rightarrow$ 6sp	3.50	3.95
L_5-L_3		2.70	2.55
L_5-L_4		2.16	1.75
L_6-L_2		4.58	5
L_3-E_F		2.23	
L_6-L_3		3.88	3.8
L_6-L_4		3.24	3
L_2-L_1	lower 6sp$\rightarrow$ upper 6sp	4.77	4.3

1.1.4 Drude theory

The CB free electrons in Au metal is often explained by the Drude theory. The Drude theory of the dielectric function is based on the motion of a charged particle, i.e., an electron, accelerated by an electromagnetic wave. It is given by:

$$\varepsilon^{Drude} = 1 - \frac{\omega_p{}^2}{\omega(\omega + i\frac{1}{\tau})}$$

Eq. 1.2

Where ω_p, the plasma frequency has been given before in eq. 1.1, and τ, the relaxation time is given by the following:

$$\tau = \frac{m}{\epsilon_0 n_e e^2}$$

Eq. 1.3

A dielectric function of a bulk material can be written as a sum of two contributions, Drude-like transitions and interband transitions:

$$\varepsilon_{metal} = \varepsilon_{Drude} + \varepsilon_{interband}$$

Eq. 1.4

As shown in Fig. 1.6, the real part of the permittivity for Au is negative from the UV to the IR, which results in an imaginary part of the refractive index. For metals, the imaginary part of the permittivity implies an energy dissipation that is relevant with the thermal motion of electrons. At IR longer than ~650 nm, the Drude model gives an accurate prediction of the permittivity of Au, which clearly have good agreements with the experimental data. However, there is a notable deviation of the imaginary part in the visible and UV region < ~650 nm. The measured imaginary part increases much more sharply than that calculated by the Drude model. This difference shows the presence of intense interband

transitions excited by the photons with higher energy and not taken into account in the Drude model. Therefore, in the region < 650 nm, the imaginary part of the dielectric function and the absorption are dominated by the interband transitions, while in > 650 nm region, the Drude-like transitions govern the picture.
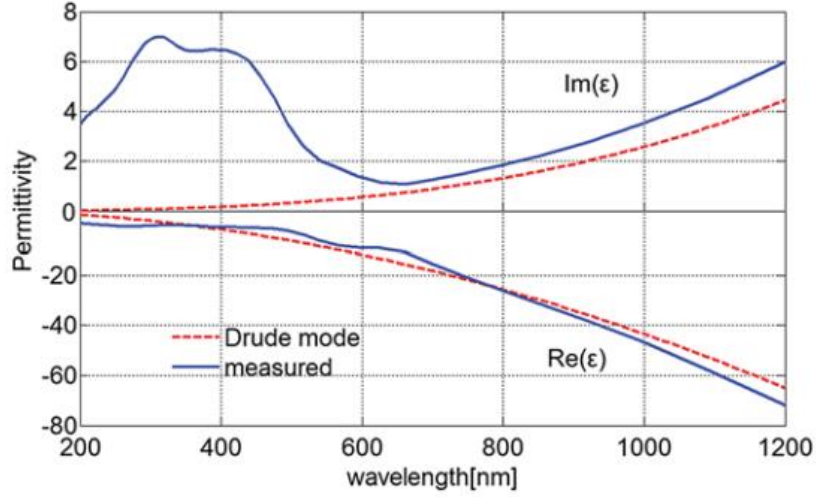
Figure 1.6 Permittivity of Au estimated by the Drude model (dotted line) and the experimental measurement (solid line). The experimental data is from Ref[27,28].

The light-NP interaction is dominated by absorption and the absorption coefficient is given by the first-order term of the Mie expansion:[29,30]

$$A(\omega) = \frac{9p\varepsilon_d^{3/2}}{c} \frac{\omega \varepsilon_2(\omega)}{[\varepsilon_1(\omega) + 2\varepsilon_d]^2 + \varepsilon_2^2(\omega)} \qquad \text{Eq. 1.5}$$

where $\varepsilon_{Au(\omega)=\varepsilon_1(\omega)+i\varepsilon_2(\omega)}$. p is the particle volume fraction and is very small ($\ll 1$) for particles dispersed in a colloidal solution, ε_d is the dielectric constant (a real quantity) of the surrounding medium. The optical response of Au NPs is characterized by a LSPR band in the proximity of 520 nm (2.38 eV), partially superposed to the tail of interband transitions at shorter wavelengths (see Figure 1.7). The extinction cross section of an Au NP is the sum of the absorption and the scattering:

$$\sigma_{ext} = \sigma_{abs} + \sigma_{scatt} \qquad \text{Eq. 1.6}$$

For Au NPs with size d $\ll$ λ, e.g. d=20 nm, where λ is the wavelength of the electromagnetic radiation, no scattering occurs and the particles only absorb radiation, thus, for NPs smaller than the wavelength of light, both absorption and scattering cross-sections are equivalent, and for larger particles, scattering dominates the overall extinction spectrum[31].
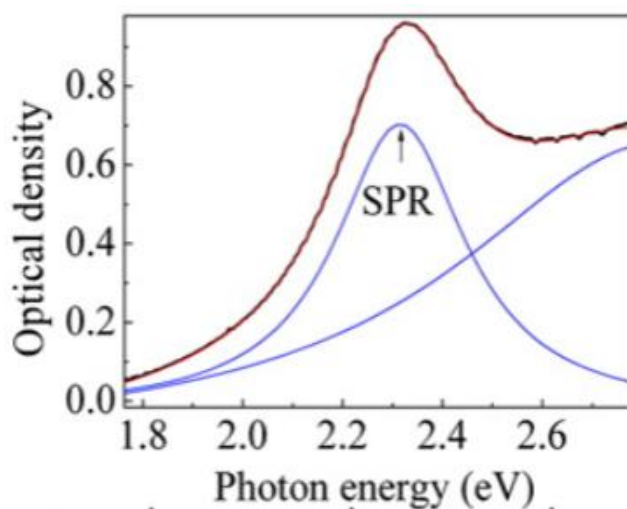
Figure 1.7 Absorption spectrum of Au nano-spheres (20nm diameter, in water solution), the blue curves illustrate the decomposition of the total spectrum to basic spectral Lorentzian contours, which are due to the plasmon band and the interband transitions[32].

1.1.5 Acoustic vibrations in Au NPs

Studies of acoustic vibrations in nanoscale metals can provide fundamental mechanical properties of the materials and enables a precisely characterize and control of the geometry and crystallinity in such materials, benefits for applications in optical communication[33], photoacoustic imaging, and nanoelectromechanical devices etc. In pump-probe experiments, the laser excitation generates a rapid temperature increase of the electron gas in Au metal, its subsequent cooling by energy transfer from electron to phonon produces a heating of the lattice, the latter results in a thermal dilation of the NP which periodically modulates the transmitted probe beam intensity, giving a 'breathing mode' oscillation signal[34–36]. Frequency and damping of the oscillations are thus directly reflecting the vibrational period of the breathing mode and its energy loss, and they are strongly depending on the size of the NPs, as well as the composition. A general picture of the Au NP after laser excitation occurs in time domain is shown in Figure 1.8, the internal electron-electron scattering happens within 100s of fs, the electron-phonon coupling takes place on time scale of 1-5 ps, while the acoustic vibrations launch after it and last from tens to hundreds of ps depending on the NP size.

In Au nanosphere, there is usually one radial mode can be experimentally observed, the relationship between the oscillation frequencies and NP size are plotted in Figure 1.9, the frequency changes from 1.0 cm^{-1} for 120 nm diameter NPs, to 11.6 cm^{-1} for 8.3 nm diameter NPs, and they can be well fitted a formula $f = (50.75 \pm 0.95)/R$, for R in nm[37].
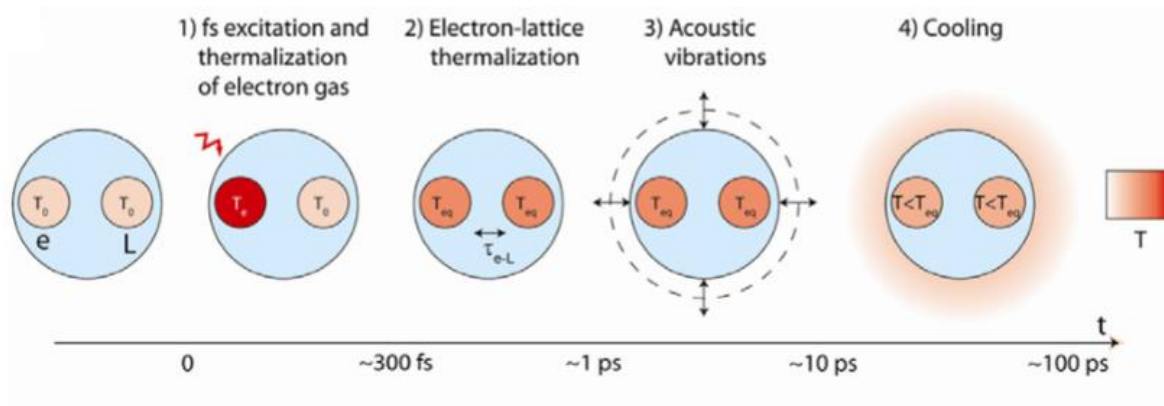
Figure 1.8 The time domain processes after laser-induced heating of the electron gas of a metal particle: electron thermalization, acoustic phonon vibrations, thermal and acoustic energy dissipating to the environment[36].
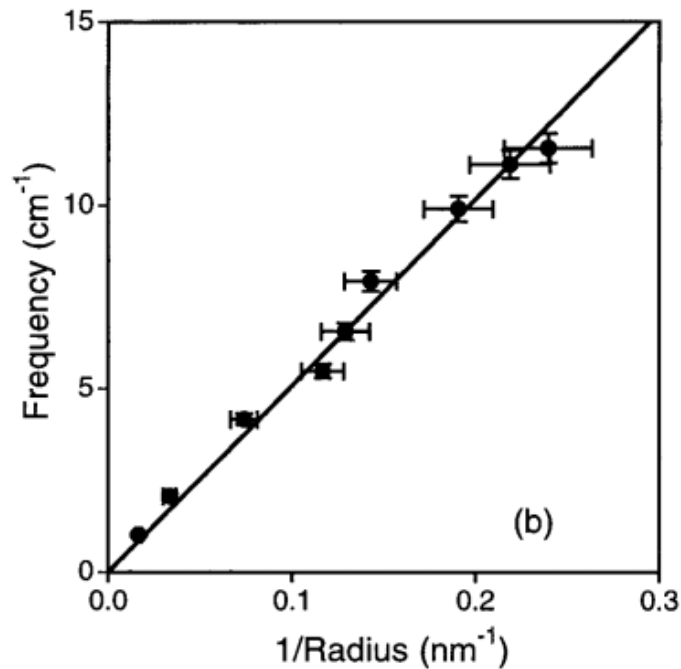
Figure 1.9 The measured frequencies vs 1/R for different Au NPs. The solid straight line represents the fit to the data[35].

1.2 Transition metal oxides

1.2.1 Anatase TiO$_2$

Anatase TiO$_2$ became a popular material for solar energy conversion after Fujishima and Honda reported that TiO$_2$ electrodes could photocatalytically split water into H$_2$ and O$_2$ in 1972[38]. This promising potential as alternative to silica-based solar cell drove an extremely intense research activity during the past three decades. It has many advantages such as cheap, abundant, nontoxic and stable; however, its ability to utilize sunlight as the primary energy source is very limited, because it only absorbs less than 5% of the solar energy in the UV region, due to its large band gap of 3.2 eV. Figure 1.10 shows a typical steady-state absorption spectrum of anatase TiO$_2$ NPs dispersed in aqueous solution, with its well-known UV absorption and a wing extending down to ~3 eV, due to scattering.

The optical properties of anatase TiO$_2$ are determined by its electronic structure, Figure 1.11 displays the calculated band structures of anatase TiO$_2$ (from ref.[39]), it shows that TiO$_2$ is an indirect semiconductor, i.e. the top of the VB and the bottom of the CB are not at the same symmetry of momentum space, the minimum energy difference between them is 3.2 eV. Within the band-gap bound electron-hole states, which called 'excitons', have many features analogous to those of atomic hydrogen, where the hole plays the role of proton[40], however, the binding energy is usually much lower (~250 meV). An ideal exciton can be considered as an electronically neutral quantum of electronic excitation energy, it can transport energy without transporting net electric charge, that is, the state itself is neutral, but it contains energy.
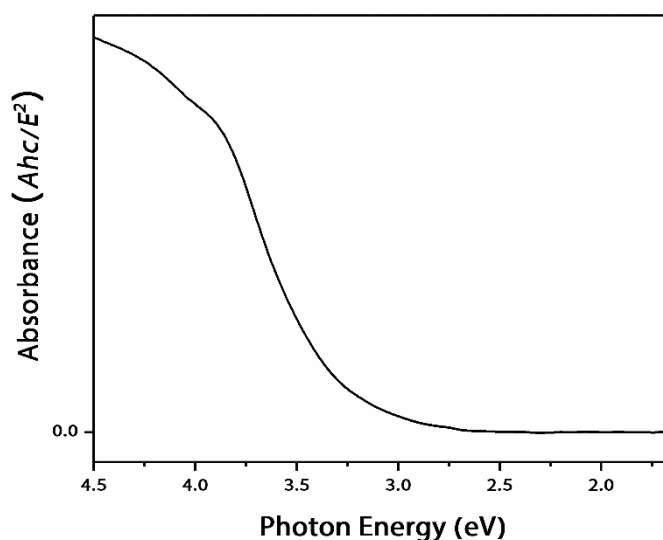
Figure 1.10 Steady-state absorption spectrum of anatase TiO$_2$ NPs (50 nm diameter) measured in aqueous solution at room temperature.
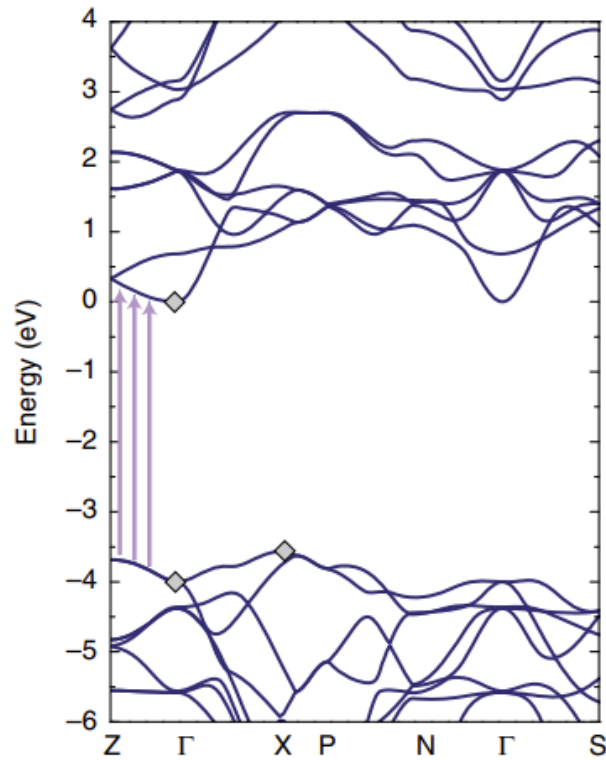
Figure 1.11 Band structure diagramme of anatase TiO_2 (from ref.[39]).

1.2.2 Sensitized TiO_2

Driven by the narrow range of the solar spectrum harvested by anatase TiO_2 which greatly limited its photovoltaic conversion efficiency (PCE), in 1991, Grätzel and co-workers[41] demonstrated the first dye sensitized TiO_2 solar cell (DSSC). Thereafter, DSSCs have been attracting attention of both researchers and industries worldwide because of their potential as alternatives to conventional silicon-based solar cells[42]. The use of sensitizers, i.e. species that absorb in the visible range and inject an electron into the CB of TiO_2 substrate, would then significantly improve the light harvesting efficiency (Figure 1.12). Alternative sensitizers are being explored such as cheaper metal-dyes, based on Fe-complexes[43], or noble metal sensitizers, in particular Au NPs[44–46]. The latter are interesting candidates because of their LSPR, which have large optical cross-sections of up to 10^5 larger than that of typical dye-sensitizers[31], and can be tuned by changing their shape, size and/or composition, enabling a good match with the solar spectrum[17,47].
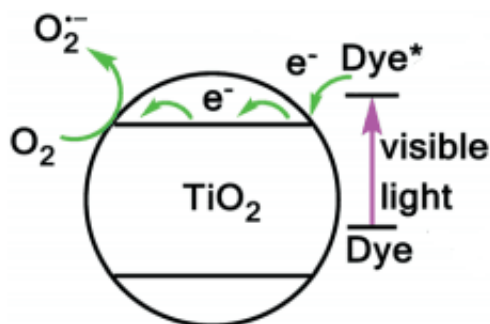
Figure 1.12 The proposed mechanism for visible light-induced dye-sensitized TiO_2 photocatalysis[48].

The visible light-excited Au/TiO_2 shows an ability to effectively convert visible light energy to electronic, chemical, or even thermal energy. The competition between photo-generated charge recombination and interfacial charge transfer between photo-excited TiO_2 and Au NPs limits the overall efficiency on the surface. The first electron transfer mechanism in Au/TiO_2, is analogous to that for the DSSC, was proposed by Tatsuma and co-workers[46] who introduced that an excited plasmon which decays through Landau damping in Au NP converts the energy of the impinging photons to hot electrons with sufficient energy to overcome the Schottky barrier (Figure 1.13) and be injected into the CB of the adjacent TiO_2, subsequently been involved for photo chemical reaction. For decades, Au/TiO_2 has been studied in various architectures: either Au NPs deposited on the surface of the TiO_2 NPs/films, or embedded in a film[12,17,47,49–51], it is worth stressing that the contact between Au NPs and TiO_2 as well as their interface quality strongly affect the PCE.
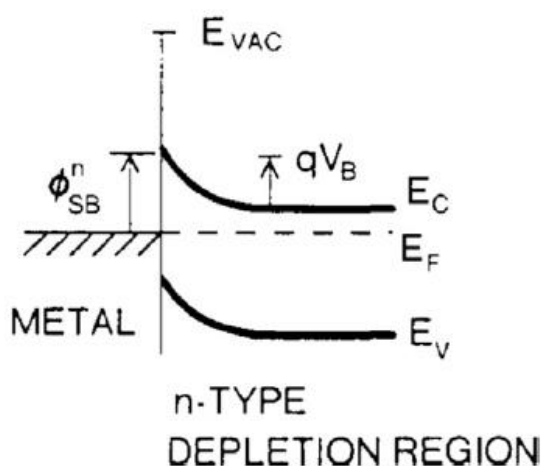
Figure 1.13 A typical energy diagram at a metal–semiconductor interface, after contact for a high work function metal and one n-type semiconductor[52].

Chapter 2 Review of the photo- and temperature- induced studies on Au and Au/TiO$_2$ NPs

2.1 Transient absorption studies on Au nanoparticles

The transient behaviour in the LSPR region has been well studied using visible TA spectroscopy[53–55], either in the form of bulk Au films[56], Au NPs embedded in silica glass[57] or in aqueous solution[58,59]. Time-resolved photoemission was used by Fann et al[60] to investigate the ultrafast electron thermalization process (electron-electron scattering) by probing of the evolution of the electron energy distribution following a 1.84 eV off-resonant optical pulse excitation, and found that the time of electrons from non-thermal to thermal distribution in 30 nm-thick Au film is tens to hundreds of fs and depend on the excitation density. The following energy transfer time from electron to the lattice was determined to be ~1 ps[61] by using multiple wavelength high-sensitivity transient reflectivity (TR)/transmissivity spectroscopy. A non-equilibrium electron distribution in Au thin film (20 nm) was created by free-carrier absorption of a visible (2.0 eV) fs pulse, and the relaxation processes were measured with a visible probe pulse. These studies focused on Au thin films because the band structure is well know[62], while EI-sayed and co-workers[54,55] performed TA spectroscopy upon interband excitation (near 400 nm) of 2-30 nm diameter Au NPs in an aqueous solution, and probed the LSPR band in the visible spectral region (typ. 450 to 700 nm, Figure 2.1). They concluded that the dynamics and spectral intensity changes are attributed to the reduction of the density of states for smaller NPs. It was also reported that the lifetime of electron-phonon interaction is around 2.5 ps. Similar work by Hartland and co-workers[63–67] examined the effects of size, shape on Au NPs (2-120 nm diameter) electron-phonon coupling with visible TA spectroscopy. It is shown that the coupling timescale is strongly dependent on the pump laser power: higher pump laser power created higher initial temperature of the electron gas which takes longer to equilibrate with the lattice. Interestingly, Del Fatti et al.[68] found that the energy transfer rate from electron to the lattice increase during the early stages of the electron thermalization, showing a non-instantaneous increase of the average electron-electron scattering rate, and the ensuing heat dissipation to the environment is strongly size- (typically from 10 ps for 4 nm particles to 400 ps for 50 nm ones in water)[69] and environment-dependent[70]. In addition, Hartland et al.[34,71] reported acoustic breathing modes (Figure 2.2) excited by the rapid lattice heating caused by the energy transfer from electrons, where the frequency (around 1-10 cm^{-1}) is size-dependent.

After the internal electron-electron scattering and electron-phonon coupling process have been completed, the hot NPs equilibrates with the environment[30,63]. Heat diffusion within the NP is usually neglected, as this is very fast for metals[72]. As is widely known[73], the electronic heat capacity is much smaller than the lattice heat capacity, which means that the initial electronic temperature after excitation is much higher than the temperature of the equilibrated electron-phonon system[30,63]. The increase in NP

lattice temperature from optical excitation is typically a few degrees to tens of degrees[74,75], and the cooling to the solvent was found to be significantly affected by the NP and its environment[29,76,77], and this process usually takes hundreds of ps. The transient response over long time delays contains information of the thermal cooling of the NP induced by energy exchange with its surrounding and heat diffusion to the latter. Vallée and co-workers[76,78–80] did works focusing on Au and Ag NPs cooling dynamics, the long-term cooling which comes from the phonon relaxation process is shown to have contributions both from the NP lattice and the environment. Since the lattice heat capacity is much larger than that of the electrons, the decrease in temperature of the electrons is much more significant than the temperature increase in lattice. After the system equalizes, the overall temperature is low and the long-term TA signal at plasmon band only reflects the heat dissipation.
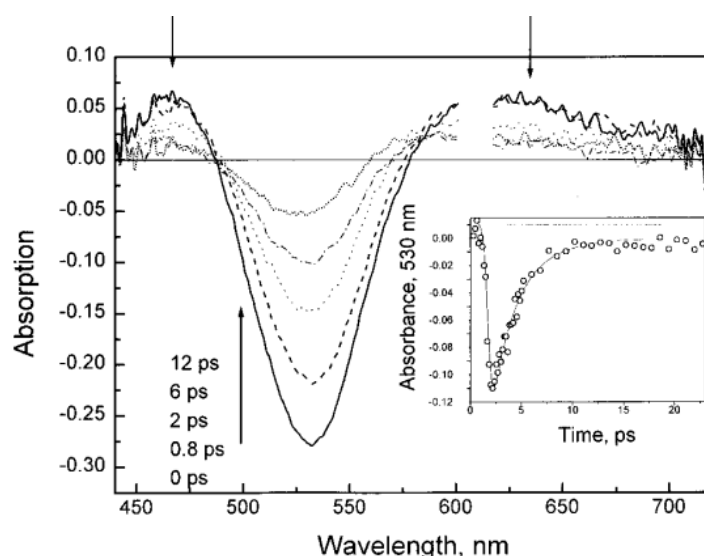
Figure 2.1 Transient absorption spectra of the ~15 nm Au NPs as a function of the time delay between the 600 nm pump and white light probe laser beams. The inset show the kinetics of the LSPR band following 600 nm excitation light[55].

Since increasing the temperature of the lattice will make an effect on the surface of the NPs, the LSPR was found to be red shift and broadening[81–84]. The coupling between the electrons and the electric field is very strong at the LSPR, and gives rise to an additional light scattering energy loss at LSPR, thus the thermal effect at LSPR band is more prominent and have a different evolution process compared to off-resonant conditions. Under the same excitation conditions, Del Fatti[27–28] found that the thermal interface conductance between water solvent and Au NPs is 110 MW/m^{-2}K^{-1} by probing away from the optical resonance in the visible region, which is about three times larger than that of ethanol-Au NPs, and the thermal cooling which comes from the Au NP lattice and its environment, was confirmed to be hundreds of ps.

Besides probing the LSPR band in visible spectral region, time-resolved X-ray scattering spectroscopy was performed to examine the lattice thermal dynamics in Au NP (100 nm diameter) in water following 400 nm excitation by Plech et al[85]. It allowed them to resolve the lattice changes in Au NP, and the

advantage is that they gain a more direct access to the atomic structure of the NPs after laser heating compared to purely optical techniques. By following the lattice cooling process with varies pump laser intensities, they found that the lattice heating is followed by cooling on the nanosecond (ns) timescale, in the meantime the lattice expansion rises linearly with excitation power up to a value corresponding to a lattice temperature increase of 529 K. Interestingly, at high temperatures the lattice shows a loss of long-range order due to pre-melting of the NP, and the structural disorder effects already occur below the Au melting point (hundreds of K). They claimed that there is no indication that the heat transfer to the surrounding should be governed solely by the heat conductivity of the water solvent, in contrast, subsequent to the thermal equilibration between electrons and lattice, the thermal energy is released to the surrounding environment across the NP-solvent interface[86,87], and the temperature decay is consistent with a finite heat transfer through the interface.
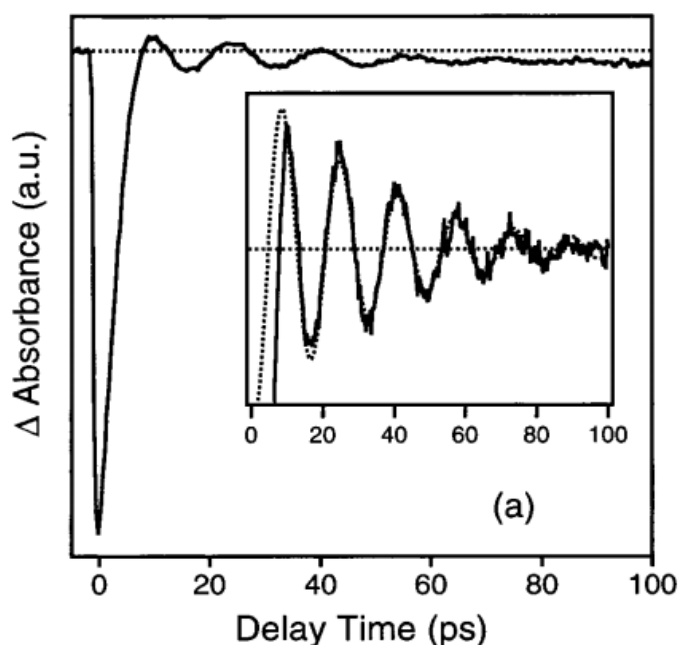
Figure 2.2 TA signal for Au particles with 60 nm diameter recorded under 400 nm pump and 550 nm probe pulses. The inset show the modulations due to the coherently excited breathing mode[88].

The above used visible or X-ray probes mostly deliver thermal dynamics rather than electronic dynamics. In Au NPs, the steady-state absorption (1.5-6.0 eV) has two components: the LSPR absorption (~2.3 eV) which is sensitive to the NP temperature and surface, and absorption (>2.3 eV) comes from the inter-band transitions. For my work, I will present the measurements of Au NPs based on visible (1.6-3.0 eV) and deep-UV (3.4-4.5 eV) TA spectroscopy. The thermal relaxation typically gives two timescales as introduced before, a fast one due to the electron-phonon energy coupling (a few ps), and a very long one (hundreds of ps to ns scale) caused by the NP and its surroundings. In contrast, deep-to-near-UV continuum TA spectroscopy[39,89,90] offers the opportunity to probe the high-energy inter-band transitions

in Au NPs. The advantage is that while promoting electrons from the 5d-band (inter-band excitation)/lower 6sp-band (intra-band excitation) up to the higher 6sp-band, the transitions of d-band/d sub-band → 6sp-band at X and L symmetries in the Brillouin zone are simultaneously monitored[20,91–96]. The details of the experiment are given in Chapter 4.

2.1.1 Two-temperature model

Laser excitation generates a hot electron gas in Au NPs, the initial temperature T_0 of the system is typically ~300 K, the electronic heat capacity constant is ~63 J/m³K³ for bulk Au[73], and the $\Delta T_{exc} = T_{exc} - T_0$ is usually in the range of hundreds of K. A typical schematic of the excitation and relaxation dynamics of Au NPs is given in Figure 2.3. The interaction between the electron and lattice following thermalization of the former can be described by a two temperature model (TTM) with electron temperature T_e and lattice temperature T_l:[97]

$$C_e(T_e)\frac{\partial T_e}{\partial t} = -G(T_e - T_l)$$

Eq. 2.1

$$c\frac{\partial T_l}{\partial t} = -G(T_e - T_l)$$

Eq. 2.2

With $C_e(T_e) = aT_e$ and c are the electronic and lattice specific heat per unit volume, G is the electron-phonon coupling constant, connected to the electron-phonon scattering rate. A typical TTM suppose that the optical laser pulse primarily increases the electronic temperature T_e while leaving the lattice temperature T_l at ambient T; subsequently the energy absorbed by hot electrons is transfered to the lattice until the $T_e = T_l$ limit is reached (Figure 2.4). This model is based on the fact that the electron-electron scattering rate is much larger than that of the electron-phonon coupling. Eventually, heat dissipates to the environment and the cooling of the hot NPs takes hundreds of ps time scale[69,70,76]. Here, the generated electrons and holes are considered 'hot' if their energies are larger than the thermal excitations at ambient temperatures.
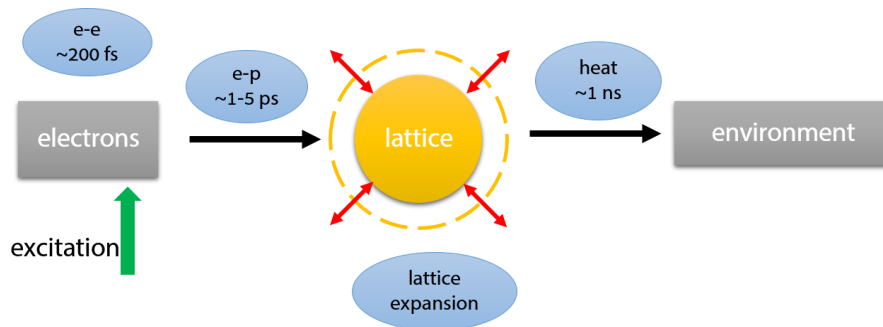
Figure 2.3 A commonly attributed schematic of the excitation and relaxation dynamics of Au NPs.
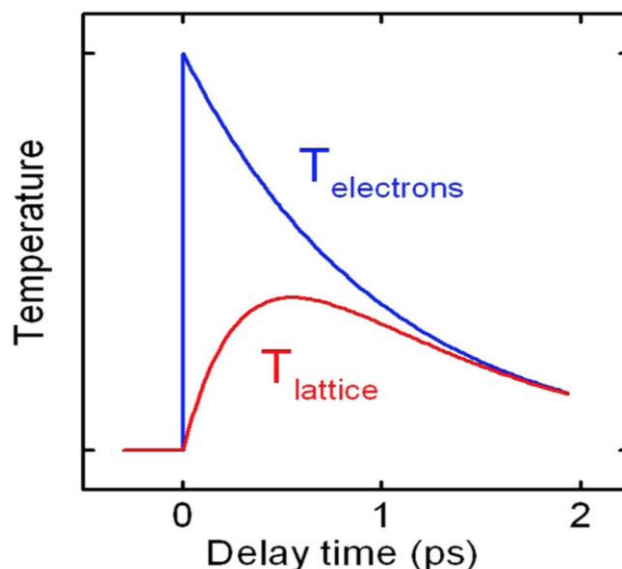
Figure 2.4 The two temperature model showing the electron temperature and lattice temperature immediately following laser excitation of a metal[98].

2.2 Temperature effects on Au nanoparticles

The heating of Au NPs under either continuous or pulsed irradiation of the LSPR has been investigated[99–106]. In these studies, the LSPR band itself is used to monitor the temperature of the NPs, either dissolved in a colloidal solution or embedded in a matrix (glass, sol-gel, mesoporous film or other)[107,108,57,109–111,77,112,58,113–115]. Ultrafast spectroscopy has been (and still is) the most frequently used tool to investigate the details of the electron and thermal evolutions in metallic materials, either in bulk or NP form[35,54,57,59,64,106,116–122]. Monitoring the LSPR response was achieved by TA in the case of NPs or transient reflectivity (TR) in the case of the bulk Au, using a broad band continuum probe. The measured transient signal is the difference of the absorption (reflectivity) after excitation with the signal before. Usually, a depletion of the LSPR band around its centre (i.e. a negative signal) and the appearance of positive features in the wings characterise the response, pointing to a broadening of the LSPR band[54,59,106]. Most of the signal recovers on a 2-3 ps time scale, leaving a weak component decaying on tens to hundreds of ps. More recently, O'Keeffe et al[122] recently proposed a disentangling of the temporal dynamics of non-thermal and thermal electrons generated by photoexcitation of NPs using non-linear optics modelling.

While the LSPR band is dominated by the Drude part of the dielectric function, at energies higher than the LSPR, the absorption spectrum of Au NPs is due to the so-called interband region (Figure 1.4), which originates from band-to-band transitions. This response consisted of positive and negative TA bands that were characterised by a temporal evolution comparable to that of the LSPR. The TA features were interpreted using the band structure (BS) diagramme of bulk Au (will be discussed in Chapter 4), considering that quantum size effects in Au occur for particle sizes below ~4 nm[123,124]. It was concluded

that the response reflects a slow cooling of the charge carriers, commensurate with the thermal cooling of the lattice, i.e. on the order of 150-250 ps. However, Kruglyak et al's study of the transient reflectivity of Au films probed in the region of the LSPR[125], in which the response of the system was rationalised by calculations that account for the full dependence of the reflectivity on the electron occupation number, which raises the question as to whether the photo-induced TA changes in the region of inter-band transitions may also be due to the temperature-dependence of their dielectric function.
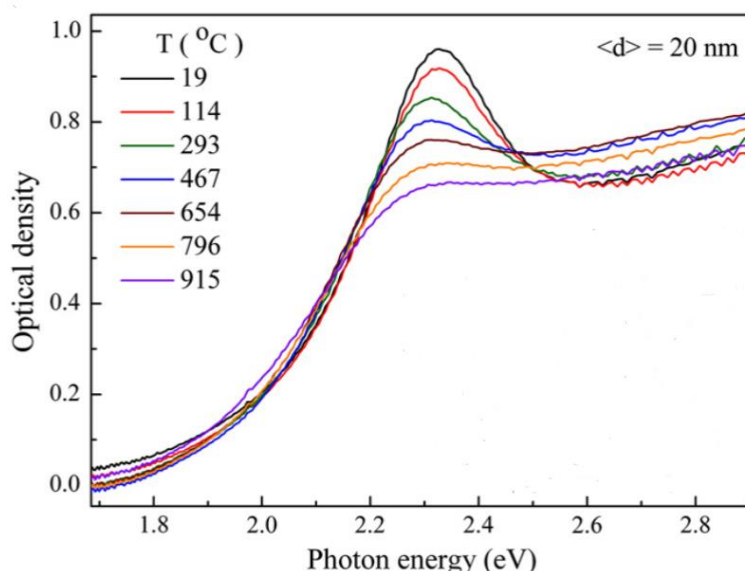
Figure 2.5 Measured absorption spectra of Au NPs with ~20 nm diameter in silica with gradual increase of temperature from 19 to 915 °C[32].

The complex interplay between electronic and thermal effects in the LSPR response of photoexcited Au NPs, can best be tackled by performing temperature-dependent steady-state absorption spectra of the NPs, comparing them to the photoexcited spectra. In studies on Au NPs embedded in silica glass, high temperatures (up to 640 K) could be reached and the effect on 12-20 nm NPs was a clear decrease of absorption intensity of the LSPR, accompanied by weak red shifts of a few 10s meV and broadenings spanning ~100 meV[123,126]. The red wing of the LSPR band was found to broaden slightly and continuously up to the maximum T, but changes were more significant on its blue wing (>2.5 eV). In this region, an increase in absorption intensity was observed up to 380 K followed by a slight decrease upon further T rise up to 640 K[126], but the absorption was still larger than at room temperature (RT). Yeschenko *et al*[32] rationalised these observations using a theoretical model that accounts for the electron–phonon scattering in the NP, its thermal expansion and the temperature-dependence of the dielectric permittivity of the host material. As the temperature increases, so does the NP volume and therefore the density of free electrons decreases, which in turn leads to a lower LSPR frequency, i.e. its red shift (Figure 2.5). Another T-dependent absorption experiment was recently done by Ferrera et al[106] who compared the result with an ultrafast study of the optical response of 2-dimensional arrays of Au

NPs (20-25 nm) films in the region of the LSPR. Figure 2.6 shows the experimental absorption spectra[106] of ~20 nm Au NPs (deposited on LiF film) measured at different temperatures and the differential absorption (difference of the steady-state spectrum at a given temperature minus that at RT) with respect to 293 K (RT), with temperature increases from 293 K to 660 K. The LSPR peak at ~560 nm broadens and weakens are due to the larger optical losses induced by the increased photon population by thermal excitation. The full-width at half-maximum of the LSPR peak evolves from 0.46 to 0.49 eV from RT to 660 K. In the differential spectra, the plasmon bleaching is apparent as the prominent negative feature in the centre of the spectral range, whereas positive wings arise from the LSPR broadening with increasing temperature. In addition, the plasmon bleach position initially red-shifts with increasing T, then blue-shifts from 415 K onward. It was explained that the red-shift of the LSPR is induced by the gradual broadening of the interband transitions of Au with increasing T, and the blue-shift is due to the temperature-induced shift of the plasma frequency to higher wavelengths. Besides, by comparing the differential temperature-dependent spectra with the TA spectra at different pump fluences, they could extract a thermometric calibration scale of ultrafast processes in the NPs. This was further supported by an independent model of the temperature-dependent differential spectra. The comparison and the modelling assume that the energy deposited in the NP by light excitation is all converted into heat.
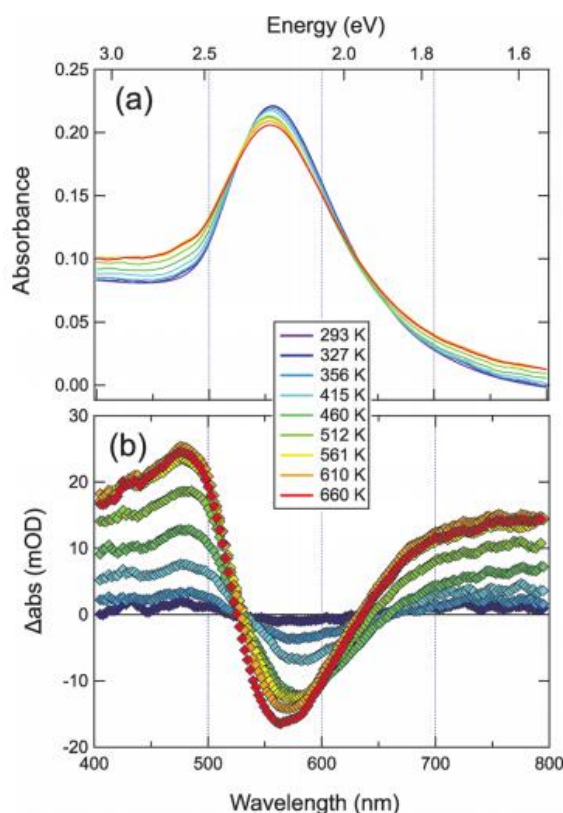
Figure 2.6 (a) Experimental static absorbance spectra of Au NPs as a function of temperature. (b) Differential absorbance spectra with respect to room temperature, obtained from panel (a)[127].

However, the temperatures reached in the above studies are far too high for NPs in colloidal solutions yet in view of their various applications in the biomedical sector (imaging, cancer therapy, etc.), it is

crucial to characterise their response in such media, and mores specifically in water. Paradoxically, such studies are very scarce. Link and El-Sayed[128] reported steady-state spectra of 22 nm Au NPs in aqueous solutions up to 345 K, showing an overall decrease of absorption around the LSPR, with no broadening, contrary to the studies at higher temperatures in silica glass[123,126]. Yeschenko *et al*[105] investigated the heating of Au NPs in a colloidal solution by irradiating them with a continuous wave laser at variable detuning (403 to 514 nm) from the central LSPR wavelength of 540 nm. As the laser wavelength was gradually tuned towards this wavelength, the LSPR band initially did not shift but then, it underwent a marked blue shift, contrary to the red shifts reported for Au NPs in silica glass[126]. This blue shift was attributed to the formation of vapour bubbles around the NP, which significantly changes the environment dielectric permittivity[103].

Recently, Magnozzi *et al*[129] reported a detailed temperature-dependent spectroscopic ellipsometry study of 2-dimensional arrays of ~20 nm Au NPs closely-packed in parallel rows and supported on a nanopatterned LiF substrate under high-vacuum. The temperature was varied from RT to 350 °C and the spectral range extended from 245 to 1450 nm (see Figure 2.7). They found that the T-dependence of the experimental real and imaginary parts of ε_{Au} exhibit a significant sensitivity with T, even at the shortest wavelengths. This indicates the above mentioned the question as to whether the photoinduced TA changes in the interband region[118], may also contain effects due to the dielectric changes in NPs. Thus, we performed a T-dependent steady-state absorption measurement and compared the results calculations based on Magnozzi *et al*[129] T-dependent dielectric data, this will be shown in Chapter 5.

The major difference between the temperature-induced and photo-induced effects is that in the latter case, electrons are transferred above the Fermi level and heat is generated by way of electron-electron and electron-phonon scattering, while in the temperature-driven case, only the lattice is heated and any changes that occur should reflect the thermally-induced modifications of the dielectric function of the NP. Apart from the above study by Ferrera et al[106], few groups have investigated the temperature-dependence of NPs in details[106,123,126,130]. The overall effect of heating is a decrease of absorption intensity of the LSPR, accompanied by weak red shifts of a few 10s meV and broadenings spanning ~100 meV. These observations were rationalised using a theoretical model that accounts for the electron–phonon scattering in the NP, its thermal expansion and the temperature-dependence of the dielectric permittivity of the host material.
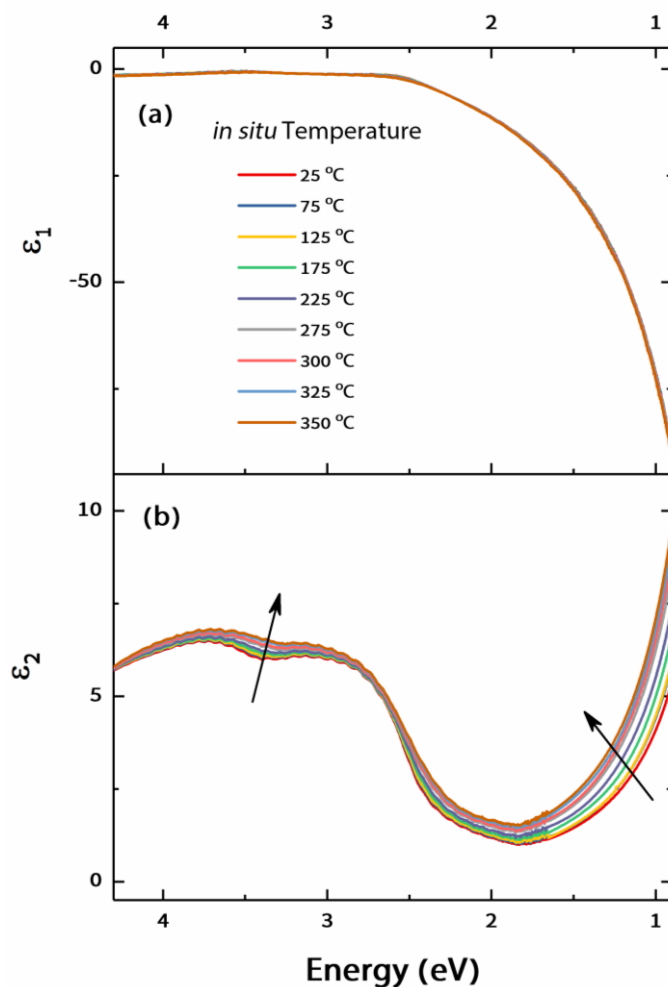
Figure 2.7 Experimental frequency dependent real (a) and imaginary (b) parts of ε_{Au} as a function of temperature; the sample is ~20 nm Au NPs deposited on a film. Reproduced from ref.[131]

2.3 Photo-induced charge transfer in Au/TiO2

Furube and co-workers[51,132,133] used an IR probe (at 3500 nm) on Au/TiO$_2$ film, and by referencing a well-known N3/TiO$_2$ electron injection case, concluded that the electron injection from 10 nm diameter Au NPs into the CB of TiO$_2$ occurs within their time resolution (~240 fs). Subsequent detailed studies[132,133] revealed that electron transfer was complete within 50 fs, where its yield is in the range of 20–50% under 550 nm excitation. As introduced before, the electron thermalization through electron–electron scattering occurs on 100's fs timescales. Therefore, in these experiments the excited hot electrons in the Au NPs were transferred to the CB of TiO$_2$ before or during the electron–electron scattering process. In this scenario, only electrons with energy higher than the Au-TiO$_2$ Schottky barrier which is about ~0.9 eV[50], can be injected into TiO$_2$. Besides, they also claimed the back electron transfer to Au takes up to ~1 ns (Figure 2.8), but this needs more investigations. Some more studies have investigated the ultrafast dynamics of electron injection into TiO$_2$ using visible excitation of the dye and

visible-to-terahertz (THz) probes of the injected electrons[134–138]. These probes are sensitive to the free carriers in the CB of the material, which are characterized by a Drude-like absorption. Further studies have used element-specific probes such as X-ray absorption spectroscopy at the Ru L- and Ti K-edges, which are sensitive to the oxidation of the sensitizer and charge trapping in the metal oxide substrate[139].
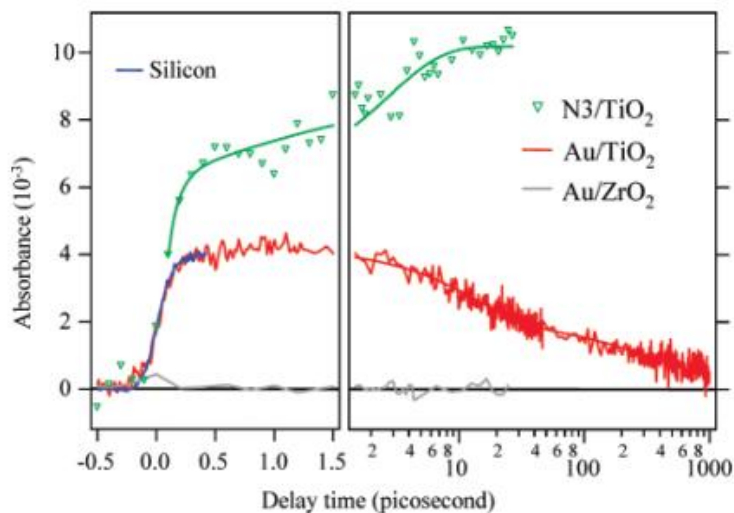
Figure 2.8 Transient absorption time traces at 3500 nm of nanocrystalline films of N_3/TiO_2, Au/TiO_2 and Au/ZrO_2. The blue solid line shows the response of the apparatus, obtained using a reference silicon plate[51].

More recently, Baldini et al[89] demonstrated that a broadband deep-to-near-UV continuum represents a substrate-specific probe of injection by monitoring the exciton response at the optical gap of the semiconductor material[89]. It detects the ultrafast electron transfer (ET) dynamics in dye-sensitized TiO_2 NPs upon exciting the Metal-to-ligand charge transfer (MLCT) state of N719 dye. Here in this dissertation I implement this approach in the case of electron injection in core-shell Au/TiO_2 NPs[140,141] and take advantage of that while we probing the response of the first exciton of TiO_2 at ~3.8 eV, the interband transitions of Au NPs are simultaneously monitored in the 3.4-3.8 eV region. The basic schematic diagram of the deep-UV probing exciton-bleaching related method in dye-sensitized TiO_2 is presented in Figure 2.9, the details of the method and set-up will be described in Chapter 3 and the results are shown in Chapter 6.
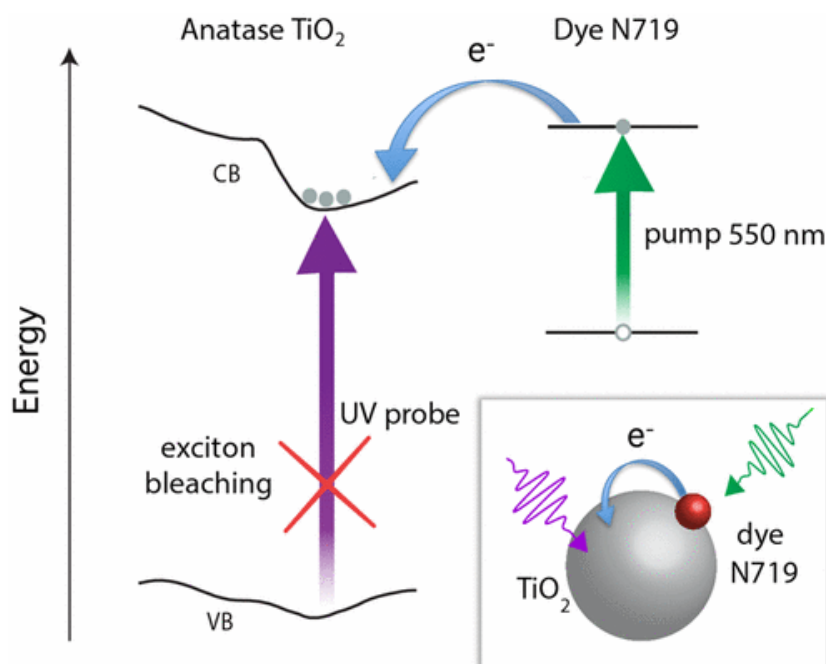
Figure 2.9 Schematic diagram of the deep-UV based detection of the ultrafast charge transfer dynamics in dye-sensitized TiO$_2$ NPs. The pump energy at 550 nm (green arrow) excites the MLCT state of the N719 dye, which then injects an electron directly into the CB of anatase TiO$_2$. The broadband deep-UV pulse (violet arrows) probes the exciton features at 320 nm for TiO$_2$. The direct transitions contributing to this collective state lie in the middle of the Γ-Z region of the Brillouin zone of anatase TiO$_2$[89].

2.4 Non-linear effects in Au/TiO$_2$

TMO thin films have also been attracting growing interest as candidates for non-linear optical materials, due to their high optical non-linearity, ultrafast response times, and low absorption indexes[142,143]. However, measurements of the non-linear optical responses of TiO$_2$ nanocomposites demonstrated that a negligible two-photon absorption (TPA) and a negative n_2 value can occur[144]. It was however noted that the non-linear optical properties of TiO$_2$ films is strongly depending on the processing route[145], as well as the inclusion of metallic NPs[146,147]. In particular, it was reported that Au/TiO$_2$ composites can exhibit a saturating and self-defocusing non-linearity at optical intensities of a few GW/cm^2 [148]. The absorption spectrum of the LSPR of Au NPs is strongly red shifted in core-shell Au/TiO$_2$ NPs compared to that of Au/SiO$_2$ core-shell ones. This has been found to strongly affect the second harmonic generation (SHG) intensity, the non-linear absorption coefficient and the non-linear refractive index. These effects have been associated to the strong field enhancement due to the LSPR of the Au NP.

TPA and self-focusing have been reported in TiO$_2$ films prepared by spray pyrolysis, while TPA was considered to be negligible for the Au NPs embedded in a TiO$_2$ film[149]. Stable core-shell Au/TiO$_2$ and Ag/TiO$_2$ NPs show saturable absorption when excited at 532 nm with moderately energetic nanosecond pulses, but they exhibit strong optical limiting when at higher intensities. This behaviour is explained in

terms of the induced optical non-linearity and non-linear light scattering. Besides, the inherent stability of the core-shell structure shows a high threshold of laser damage for these materials, making them promising candidates for optical limiting in high energy [150]. It has also been noted that Au NPs-doped multilayer such as Au/SiO$_2$ and Au/TiO$_2$ films can be used as optical filters, due to their larger third-order non-linear susceptibilities and high damage threshold[151].

The latter studies prompted us to investigate spectroscopically non-linear absorption of Au/TiO$_2$ core-shell NPs in colloidal solutions. The occurrence of such transitions, and in particular TPA, was previously unobserved for bare TiO$_2$ NPs even up to fluences of 300 mJ/cm^2 [89,139]. In Chapter 6, we will also look into the response of Au/TiO$_2$ NPs upon excitation resonant with the LSPR of the Au NP core in the visible, while the probing is done using a deep-UV broadband continuum, which spans the region of the first excitonic transition of anatase TiO$_2$.

Chapter 3 Methods

3.1 Experimental techniques

3.1.1 Transient absorption spectroscopy

Transient absorption (TA) spectroscopy, which is also known as pump-probe spectroscopy, is a widely used technique of time-resolved spectroscopy, based on the absorption measurement. The basic principle of an ideal pump-probe spectroscopy is simple: a short laser pulse is split into two parts, which are then focused on the same spot on the sample. One of the two pulses serves as a pump, performing an optical excitation, the other one arrives some time (delay time) after the first one and is used to measure the transient changes of the absorption of the sample induced by the pump pulse, as depicted in Figure 3.1. The pump beam should be much more intense than the probe, because it produces the changes in the sample, whereas the probe merely interrogates them. In an ideal case, the probe has no influence on the sample being investigated.

The temporal dimension is introduced by a controlled motorized translation delay stage which has a retroreflector on it. By electronically moving the delay stage in the path of the probe beam, it varies the time of the probe pulse with respect to the pump, thus we are able to measure the entire time-dependence of the differential absorption signal. Since the vacuum light travels 0.3 μm in a fs, the stage length and path resolution determines the available time window (usually ~1 ns) and time interval (sub-fs) of the probe.
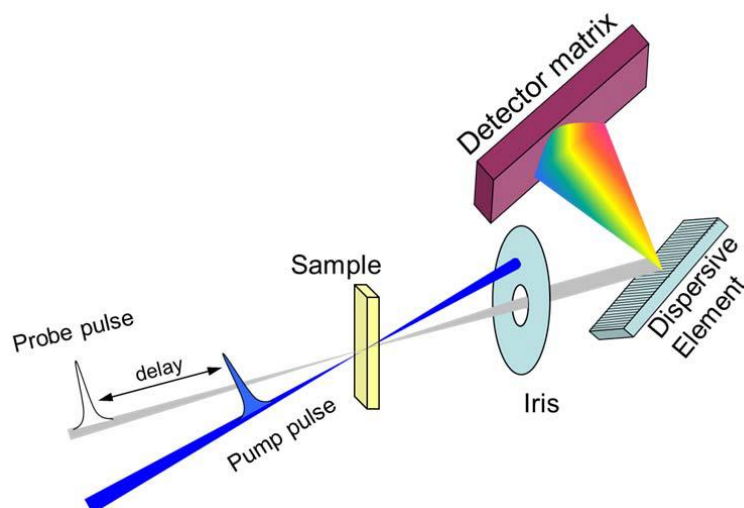
Figure 3.1 A typical schematic diagram of pump-probe experiment: The sample receives two pulses with a time delay: the pump and the probe. After going through the sample, the pump will usually be blocked, and the probe beam intensity is measured in transmission. The variable time delay between the pump and probe pulses gives the controllable time dependence of the changes of absorption signal.

The transient absorbance of the sample is recorded as the difference between the absorbance with the presence and absence of the pump pulse, according to the Beer-Lambert law, the probe intensity after the excited sample is

$$I_{exc} = I_0 \cdot 10^{-A_{exc}}$$

Eq. 3.1

Here, I_0 is the incident pulse intensity and A_{exc} is the excited sample absorption. Likewise, the probe intensity after the unexcited sample is

$$I_{noexc} = I_0 \cdot 10^{-A_{noexc}}$$

Eq. 3.2

By dividing the above two equations, we obtain the transient absorption signal

$$\Delta A = A_{exc} - A_{noexc} = lg \frac{I_{noexc}}{I_{exc}}$$

Eq. 3.3

It means that there is no need to measure the incident light beam intensity I_0. A typical pump-probe signal contains three kinds of contributions shown in Figure 3.2, namely:

(1) Ground state bleaching (GSB);

(2) Stimulated emission (SE);

(3) Excited state absorption (ESA).

When the pump pulse excites the sample, some electrons are removed from the ground state and promoted to the excite state, which means a decreased absorption of the ground state, therefore, at the energy of the ground state absorption, the transient signal becomes negative and this signal remains until all the excited electrons relax back to the original ground state. Another type of TA signal is SE, which arises as an increase of the probe light upon sample excitation, when the probe pulse detects that some of the electrons in the excited state, the probe photons stimulate the emission of the sample, which is a phenomenon underlying the principle of lasers. The ESA can only occur in the excited states and is usually referred to the fact that the electrons in the excited state could absorb another photon and go to a higher state, therefore, after the photo-excitation, additional induced absorption appears and the corresponding ΔA signal is always shown positive.

In my PhD, the main TA set-ups I used are deep-to-near-UV (20 kHz) and visible (1 kHz) TA set-ups, which I will introduce below separately.
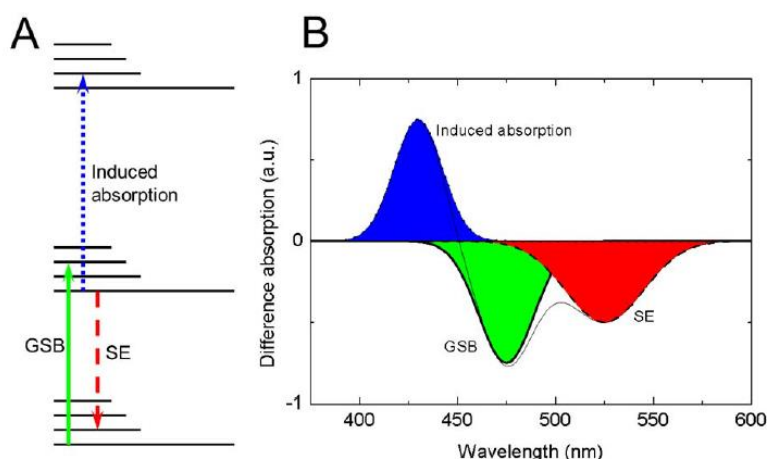
Figure 3.2 A) Typical energy levels of a hypothetical molecule and three types of transitions influencing the difference absorption spectrum. B) The corresponding difference absorption spectrum together with the separated contributions of the three different transitions.

3.1.2 Deep-UV transient absorption spectroscopy

Figure 3.3 shows a schematic view of the 20 kHz deep-UV transient set-up, including the laser system, non-collinear Optical Parametric Amplifier (NOPA), and achromatic doubling (AD). The laser system consists of a Ti: sapphire oscillator (Halcyon), which seeds a cryogenically cooled regenerative amplifier (Wyvern500), pumped by three pump lasers (DS20HE532, Photonic Industries). The laser system provides ~0.7 mJ pulses at 800 nm, of 50 fs duration, about 70% of the power is used to pump the NOPA to generate sub-90 fs visible pulses (520 - 740 nm range), the typical output energy per pulse is 13 μJ. The output of the NOPA is further split into two parts, one (60%) goes through a chopper, which operates at 10 kHz and is phase-locked to the laser system to obtain the pump pulse. The pump maximum energy is about 120 nJ per pulse and the pump power is recorded on a shot-to-shot basis by a calibrated photodiode for each pump wavelength which allows for the normalization of the data based on the average pump power. The remaining 40% of the NOPA output is used to generate the broadband deep-UV probe pulses with around 100 nm bandwidth through an AD scheme (Figure 3.5), after passing through a 30 cm electronically controlled delay stage (Aerotech, BMS60). The generated broadband UV probe pulse are shown in Figure 3.4. A half waveplate is used to set the relative polarization between the pump and probe beams at the magic angle (54.74º) to get rid of photo-selection effects. Pump and probe pulses, are then focused onto the sample, where they are spatially and temporally overlapped.
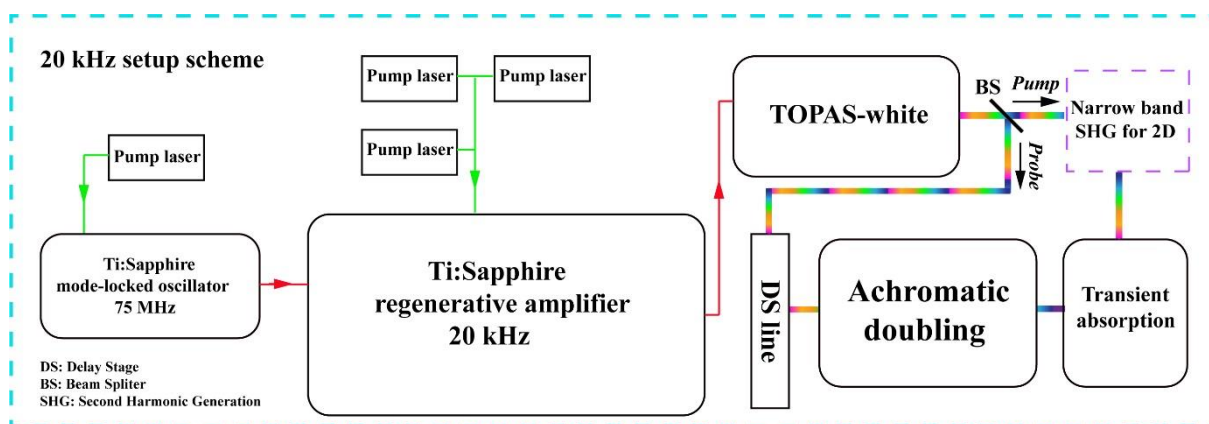
Figure 3.3 layout of the 20 kHz deep-UV transient absorption set-up, including the laser system, NOPA, and AD components.

The AD comprises two fused silica prisms that spatially disperse and re-collimate the broadband visible beam coming out from the NOPA. The resulting spatially chirped beam is then focused with a 90° off-axis parabolic mirror on a 0.2 mm thick BBO crystal. The frequency doubling of such broadband visible beam is much more difficult as there is only one phase-matching angle at each frequency component. Therefore the spatial chirp of the broadband visible beam and the different incident angles achieved by the parabolic mirror onto the BBO can match the phase-matching conditions at all probe wavelengths at the same time. The frequency doubled beam is subsequently re-collimated with another 90° off-axis parabolic mirror, recombined and re-compressed with two additional CaF_2 prisms, to deliver the broadband UV probe beam.
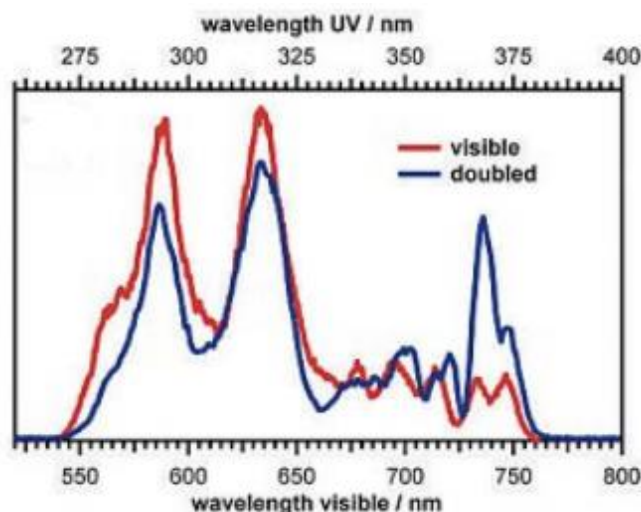
Figure 3.4 The broadband UV probe pulse generated through AD, the red line shows the output spectrum of the NOPA, from the 20 kHz deep-UV transient set-up[122].
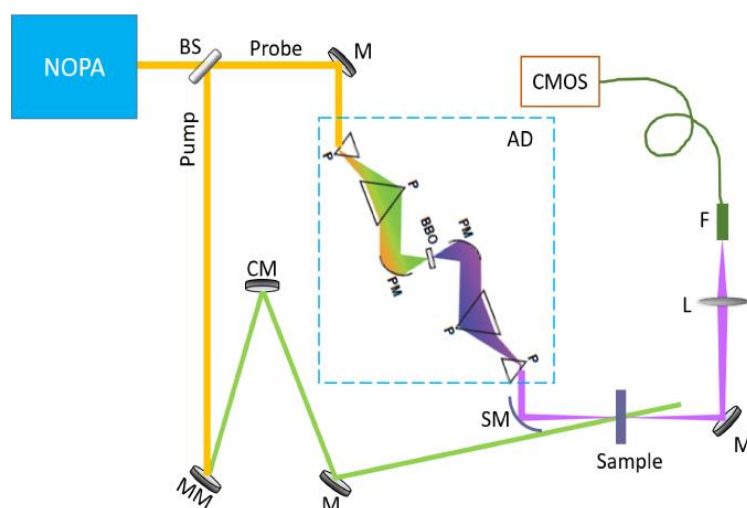
Figure 3.5 A diagram of the transient deep-UV spectroscopy setup, detailing the broadband pump-probe experiment after NOPA. The blue dashed box shows the schematic of the AD, adapted from Ref.[152], BS: Beam splitter, M: Mirror, MM: Multi-layer Mirror, CM: Chirped mirror, SM: Spherical mirror, PM: Off-axis parabolic mirror, P: Prism, L: Lens, F: Multi-mode fiber.

The typical pump and probe spot sizes are 120 μm and 50 μm full-width half-maximum (FWHM), respectively, resulting in a homogeneous illumination on the sample's probe region. The samples used in this set-up either are thin film or solution in a quartz flow-cell. The probe was measured after the samples's transmission and its detection synchronized with the laser repetition rate. The differences of the absorption with and without the presence of pump beam has been measured at varying time delays between the pump and the probe pulses. After the sample, the transmitted broadband deep-UV probe beam is focused into a multi-mode optical fibre, which is coupled to the entrance slit of a 0.25 m imaging spectrograph (Chromex 250is). The beam is dispersed by a 150 gr/mm holographic grating and imaged onto a multichannel detector consisting of a 512 pixel CMOS linear sensor (Hamamatsu S11105, 12.5 × 250 μm pixel size) with up to 50 MHz pixel readout, so the maximum readout rate per spectrum (almost 100 kHz) allows one to perform shot-to-shot detection. The described experimental setup offers an instrument response function (IRF) of ~250 fs by measuring a flow-cell with pure solvent. The method of the determination of IRF will be introduced later.

3.1.3 Visible transient absorption spectroscopy

The 1 kHz set-up is used to perform visible transient absorption experiment. For the laser system, a continuous wave Nd: YVO_4 (Nd^{3+}-doped yttrium vanadate crystalline matrix) laser (Millennia Vs, spectra Physics) is used to pump an 80 MHz Ti: Sapphire mode-locked oscillator (Trunami, Spectra Physics) with 4.5 W pump power at 532 nm. The oscillator provides an 800 nm seed laser with a FWHM

of about 15 nm and ~330 mW power. The seed is then used for the 1 kHz Ti: Sapphire regenerative amplifier (Spitfire, Spectra Physics), which delivers 800 nm pulses with a typical power of ~0.45 mJ with ~120 fs pulse duration, 15-20 nm bandwidth, and 0.2% rms (energy flcuturation). The amplifier is pumped by a Nd: YLF (Neodimium doped Yttrium-Lithium fluride) pulsed laser (Quantronix), the pump laser gives 170 ns pulses at 527 nm at 1 kHz with 9 W power. Then after a telescope, the 800 nm laser beam is split into two parts, which are used to generate pump and probe beams, respectively.

The pump part: the pump beam is injected into a home-made NOPA, which is depicted in Figure 3.6, the pump beam is further split into two parts by a ratio of 8:2, one is used to pump a Ti:Sapphire crystal to produce visible light in the spectral range of 500-750 nm, the second weaker part is focused into a 0.25 mm thick BBO crystal, and then these two beams are overlapped and re-focused onto a second BBO to generate tuneable visible pump light. There is a delay stage in the seed path line and is used for selecting the visible pump wavelength. Afterwards, the visible pump beam goes through a pair of prism to get compressed to have a less than 30 fs pulse duration with ~10 nm bandwidth, the overall selectable visible pump beam spans from 500 to 630 nm. Alternatively, if there is no need for visible pump, a direct 400 nm pump beam is achievable after the first BBO as described in Figure 3.6. The pump beam is chopped by a phase-locked mechanical chopper operating at half of the amplifier repetition rate.

The probe part: the broadband visible probe pulse is obtained by focusing a small portion (~1 mW) of the 800 nm beam onto a continuously shaking CaF_2 crystal (0.5 cm thickness), the up and down moving of the plate is to prevent photo-damage. The generated white light has a spectral range of 380-750 nm.

The two paths are then overlapped on the sample with an angle of approximately 10°, after the sample, the probe beam is then dispersed by an 830 gr/mm transmission grating and re-focused on a 512 pixel photodiode array. The typical pump and probe beam size (at the focused position) diameters are ~150 μm and ~80 μm, respectively.
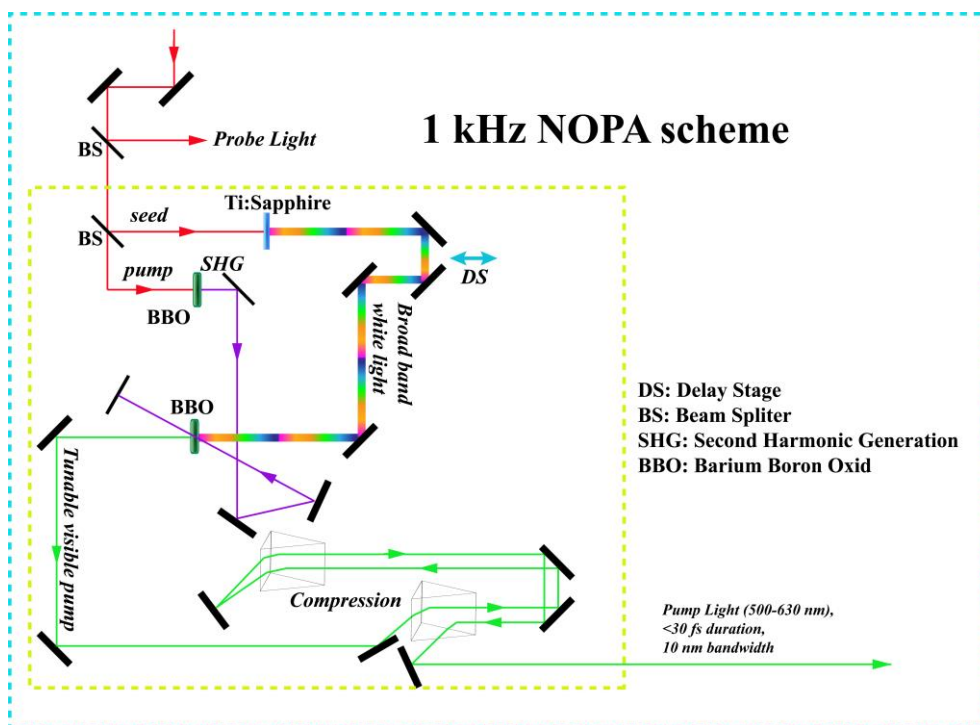
Figure 3.6 Scheme of the NOPA of the 1 kHz visible transient setup.

3.2 Data treatment

3.2.1 Jacobian conversion method

In absorption measurements, often, the signal data are measured and presented as a function of the electromagnetic spectrum and the absorption data are recorded in unit of wavelength, but presentation of the absorption data as a function of energy usually provides better physical insight. The inverse relationship between the two quantities has sometimes led to misinformation and incorrect features, a proper presentation of absorption spectral data is thus important for enlightening scientific research. Normally, converting a spectrum from the measured nm to eV directly yields an incorrectly processed spectrum as depicted in Figure 3.13, evenly spaced data intervals in wavelength regime are unevenly spaced in energy, the constant unity signal in wavelength, gives a curve because the signal per unit energy is higher at lower energy or higher wavelength when the wavelengths are properly converted to energy.

To convert the nm to eV scale, we followed the Jacobian conversion method[153]. The wavelength is converted to energy using $E = hc/\lambda$, and the signal values themselves are scaled by (hc/E^2), where E represents the photon energy, h is the Planck constant, c is the light speed, and λ represents the wavelength.
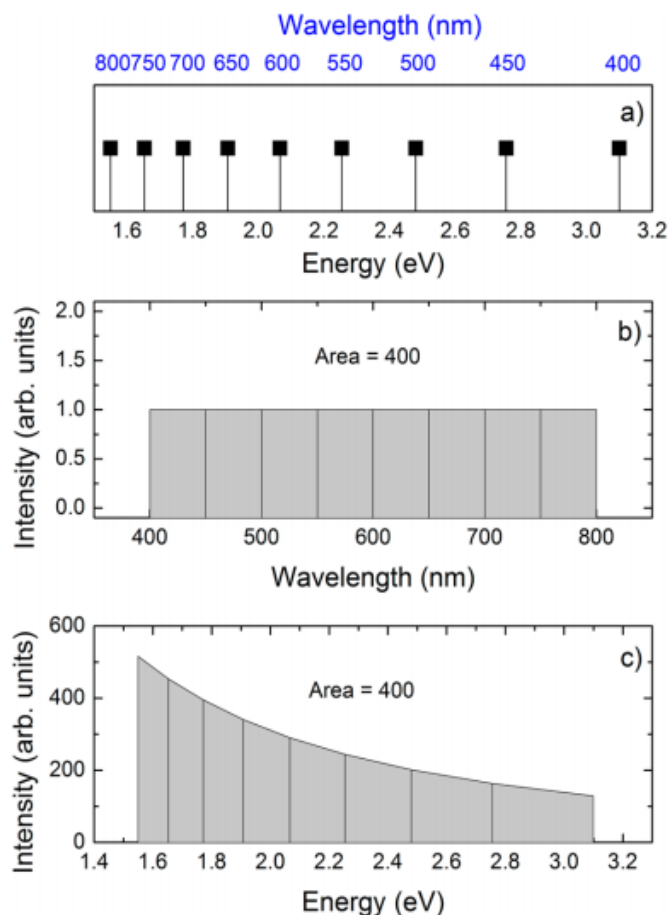
Figure 3.7 (a) Due to the inverse relationship between energy and wavelength, the evenly spaced data value intervals in wavelength are unevenly spaced in energy. (b) A constant signal in the unit of wavelength between 400 and 800 nm produces an area of 400. (c) A constant signal in the unit of wavelength, gives a curve because the signal per unit is higher at lower energy or higher wavelength when the wavelengths are properly converted to energy. Therefore, it preserves the area of 400, whereas if the signal are not converted during conversion and only the wavelength unite are converted to energy scales, the area under this curve would be incorrect[153].

3.2.2 Determination of instrument response function

As mentioned in the 3.2.3, the quartz flow cells used in my experiments have optical paths of 0.1, 0.2 and 0.5 mm, however, the normal flow cells have two external walls with ~1 mm thickness, due to the off-resonant contribution of the walls[154], the cross-phase modulation (CPM) at time zero is very significant, even though in the experiments we used a drilled-flow cells which has thin apertures in each of the two windows, the CPM is still strong, with consequent loss of the time resolution at time zero position, especially in my case that is doing a broadband band visible pump/broadband UV probe TA measurement with prominent Group Velocity Dispersion (GVD), as shown in Figure 3. 14.

The cross-correlation between pump and probe pulses can be represented by the IRF which is determined by measuring the FWHM of the CPM at time zero of the pure water solvent (in a 0.2 mm

optical path length drilled flow cell in this case). I adopted a procedure by fitting the CPM signal with a function composed of a Gaussian and its first and second derivative as below:[155]

$$G(t) = \frac{1}{\sigma\sqrt{2\pi}} e^{-\frac{t^2}{2\sigma^2}}$$

Eq. 3.4

$$G(t)' = \frac{(c-t)}{\sigma^3\sqrt{2\pi}} \exp(-\frac{(t-c)^2}{2\sigma^2})$$

Eq. 3.5

$$G(t)'' = \frac{(t^2 - 2ct - \sigma^2 + t^2)}{\sigma^5\sqrt{2\pi}} \exp(-\frac{(t-c)^2}{2\sigma^2})$$

Eq. 3.6

of which the FWHM $= 2\sigma\sqrt{2\ln(2)}$, t is the time variable, and c is the offset of time zero. The IRF was found to be ~250 fs (Figure 3.15).
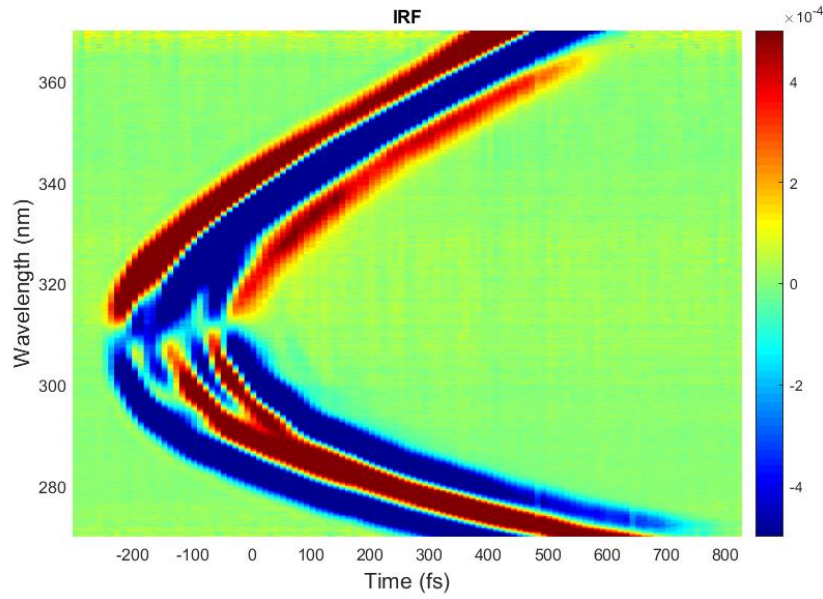
Figure 3.8 the cross-phase modulation signal upon visible-pump/UV-probe at time zero region by measuring a drilled quartz flow cell with pure water inside.
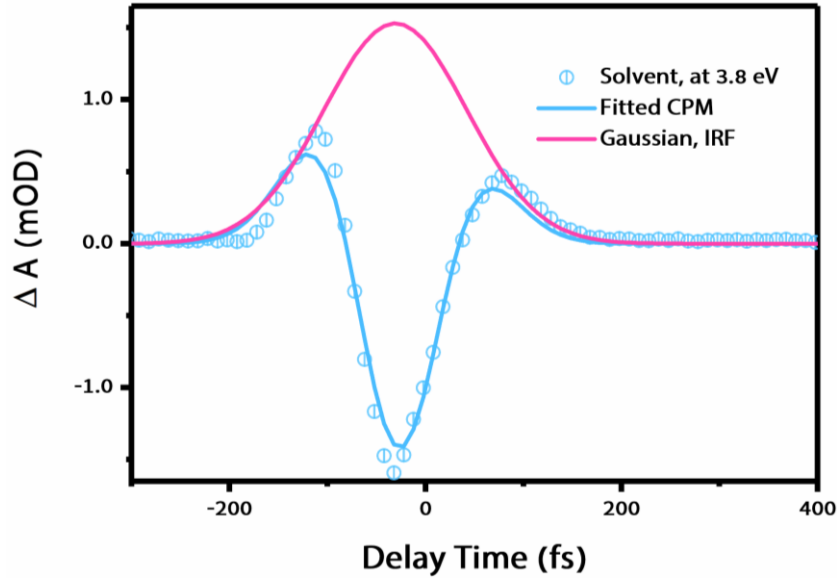
Figure 3.9 The pure solvent (water) CPM fit. The cyan circles represent experimental data, the cyan solid line is the fitted CPM curve, and the red solid line is the Gaussian peak, which has the same FWHM.

3.2.3 Kinetic trace fitting

The TA kinetic traces are fitted by using the equation below:

$$I(t) = \left\{ \left[\sum_{i=1}^{n} A_i \cdot e^{-(t-c)/\tau_i} \right] + \left[A_{osc} e^{-(t-c)/\tau_D} \cdot cos\left(\frac{2\pi}{\tau_{osc}} \cdot (t-c) - k \right) \right] \right\} * \text{IRF}(t) \qquad \text{Eq. 3.7}$$

where t is the time variable, n is the number of exponential decay functions used, c is the time zero offset, A_i is the decay function amplitude, A_{osc} is the oscillation component amplitude, k is the phase of the cosine function, τ_i represents the decay time constant, τ_{osc} represents the oscillation period and τ_D represents the damping constant.

And the calculated equation of the convolution of a Gaussian and an exponential function is shown below:

$$I(t) = Aexp(-\frac{t}{\tau} + \frac{\sigma^2}{2\tau^2})(1 + \text{erf}(\frac{t - \frac{\sigma^2}{\tau}}{\sqrt{2}\sigma})) \qquad \text{Eq. 3.8}$$

In the fitting, we take into account the contributions: i) the promptly rising within the IRF; ii) a long-lived decaying kinetic (with a short-lived decay at 3.8 eV); iii) damped cosine functions for the coherent oscillations.

The fit function contains two terms: one is the mono- or bi-exponential decay function, depending on the trace; the other is the damped cosine function. The above two terms are convoluted with the IRF, taken as a Gaussian with ~250 fs FWHM (determined in 3.3.2).

The uncertainty on the time-zero position, due to the asymmetry and probe energy dependence of the cross-phase modulation signal and to the GVD correction, makes the absolute value of the phase of the oscillations difficult to retrieve. Therefore, we use a time zero offset c, and the offset could be different at different probe energies.

3.2.4 Fluence dependence measurements

The fluence dependence experiments were performed by measuring the TA at specific time delays between pump and probe, in a range of pump fluences.

Prior to the measurement, we firstly determine the time zero position at the delay stage, by looking at the point where the signal starts to appear while electronically moving the stage. Secondly, we convert the desired delay time into distance on the stage, and calculate the position of the stage with respect to time zero. Then we set two time points slightly before and after the desired time, (e.g. it measures TA response at ~9.9 ps and ~10.1 ps if 10 ps is chosen) and take the average TA values at these two time points.

The average incident pump fluence F (measured in $\mu J/cm^2$ or mJ/cm^2) is defined as F = P/(r · A), where P is the average of the pump laser power, r is the repetition rate of the amplifier, and A is the pump beam spot size. The measurement of the laser beam spot size is performed using a camera-based beam profiling system, which consists of a camera and analysis software, the beam spot size diameter is determined by the FWHM of the beam profile. We firstly set a range of the pump power (the upper power limit is determined by the laser system, the lower limit is selected based on the smallest signal amplitude) and use a round continuously neutral density filter to control the power. The impinging pump power P is measured by using an UV-extended ultra-sensitive photodiode, we record the power P before and after one signal TA measurement and take the average value of these two.

3.2.5 Estimation of the laser-induced temperature increase in Au NP

In the pump-probe experiment, the laser-induced temperature increase in Au NP can be simply calculated according to the typical heat absorption equation:

$$Q = m \cdot C_p \cdot \Delta T \qquad \qquad \text{Eq. 3.9}$$

Q means the heat absorbed by a single Au NP, m is the mass of the heat absorbing subject (one Au NP is this case), C_p is the specific capacity of Au and ΔT is the change in temperature.

Since the spot size of the pump beam is much larger than the NP cross-section, we have to consider the actual absorption cross-section ratio (as shown in Figure 4.2), I use: $\frac{A_1}{A_2}$, A_1 is the cross-section of the Au NP, A_2 is the pump spot size.

It can be written as:

$$\frac{P}{R} \cdot \frac{A_1}{A_2} \cdot \alpha = \rho \cdot V \cdot C_p \cdot \Delta T \qquad \text{Eq. 3.10}$$

P is the pump power in W, R is the repetition rate of the pump laser, α is the sample's absolute absorbance at the plasmon band, ρ is the density of bulk Au, V is the NP volume.

Thus:

$$\Delta T = \frac{P \cdot A_1 \cdot \alpha}{R \cdot A_2 \cdot \rho \cdot V \cdot C_p} \qquad \text{Eq. 3.11}$$

In which,

$$P = 2.5 \text{ mW};$$

$$A_1 = \pi \cdot r_1^2 \ (r_1 \ is \ the \ radius \ of \ the \ NP, 15 \ nm);$$

$$A_2 = \pi \cdot r_2^2 \ (r_2 \ is \ the \ radius \ of \ the \ beam \ spot, 75 \ \mu m);$$

$$R = 10^4 \ Hz \ \left(\frac{1}{s}\right);$$

$$V = \frac{4}{3} \cdot \pi \cdot r_1^3 \ ;$$

$$\rho = 19.3 \ \frac{g}{cm^3} ;$$

$$\alpha = \sim 0.3;$$

$$C_p = 0.126 \ \frac{J}{g \cdot K} ;$$

$$\Delta T = \frac{2.5 \ mW \cdot \pi \cdot r_1^2 \cdot \alpha}{10^4 \ \frac{1}{s} \cdot \pi \cdot r_2^2 \cdot 19.3 \ \frac{g}{cm^3} \cdot \frac{4}{3} \cdot \pi \cdot r_1^3 \cdot 0.126 \ \frac{J}{g \cdot K}}$$

$$= 87.5 \text{ K}$$

Hence, we have a rough idea that the temperature rise in Au NP in our TA experiment is approximately 87.5 K under the pump power used, the error in the calculated temperature should be completely due to the uncertainty of the pump beam spot size and the measured average pump power.

3.3 Samples

3.3.1 Preparation methods

The samples used in this thesis are mainly Au NPs, Au/SiO$_2$ core-shell NPs and Au/TiO$_2$ core-shell NPs. The pure Au NPs are synthesized by myself in the lab, while Au/SiO$_2$ and Au/TiO$_2$ core-shell NPs are provide by the Chinese University of Hong Kong (CUHK). Below shows the preparation method for each sample.

Preparation of bare Au NPs: The Au NP samples were synthesized through a seed-mediated growth method[140]. Specifically, a cetyltrimethylammonium bromide (CTAB) solution (0.1 M, 9.7 mL) was first mixed with a HAuCl$_4$ solution (0.01 M, 0.25 mL), followed by a rapid injection of a freshly prepared, ice-cold NaBH$_4$ solution (0.01 M, 0.60 mL) under strong stirring. The resultant solution was kept under gentle stirring for another 3 h at room temperature. The as-prepared seed solution (0.24 mL) was then injected into a growth solution made of CTAB solution (0.1 M, 19.5 mL), deionized water (380 mL), HAuCl$_4$ (0.01 M, 8 mL), and ascorbic acid (0.1 M, 30 mL) afterwards. The reaction mixture was gently mixed well and left overnight at room temperature. The resultant Au NPs samples were washed and concentrated three times by centrifugation and re-dispersion into water for further use.

Preparation of the Au/SiO$_2$ NPs: CTAB molecules adsorbed on Au NPs were first replaced by thiol-terminated methoxy poly(ethylene glycol) (mPEG−SH). Au NPs solution (100 mL) was centrifuged and re-dispersed in water (20 mL). Then, mPEG−SH (molecular weight: 5000, polymer chain concentration 1 mM) solution (2 mL) was subsequently added. The resultant solution was kept undisturbed at 25 ℃ for 12 h and then centrifuged twice to remove the excess mPEG−SH polymers. The obtained mPEG-coated Au NPs were re-dispersed in a solution mixture containing 4.5 mL of water, 15 mL of absolute ethanol, and 0.3 mL of NH$_3$·H$_2$O (30 wt %). After that, 0.08 mL of the silica precursor solution (5 vol % tetraethylorthosilicate (TEOS) in absolute ethanol) was injected into the Au NPs solution under ice-cold and ultrasonication conditions for 1.5 h. For the temperature-dependent absorption measurements, the Au/SiO$_2$ NPs were sonicated for 3 h, to eliminate agglomeration.

Preparation of the Au/TiO$_2$ NPs: The preparation of titania coated Au NPs (Au/TiO$_2$ NPs) was a modified synthetic procedure[141]. TiCl$_3$ was used as the TiO$_2$-precursor. The CTAB-capped Au NPs were first wrapped with poly(sodium 4-styrenesulfonate) (PSS). Typically, the solution (20 mL) of an as-grown CTAB-capped Au NP sample was first centrifuged and then re-dispersed into water (10 mL) to remove the excess surfactant. The resultant Au NP solution was then added dropwise under vigorous stirring to an aqueous PSS solution (2 g·L^{-1}, 10 mL, containing 6 mM NaCl). PSS adsorption was done for at least 6 h at room temperature. The PSS-encapsulated Au NP were re-dispersed into water (0.2 mL) after the excess PSS was removed by centrifugation. TiCl$_3$ solution (0.2 mL, 17.1 wt%, containing 25 wt% HCl) and water (6 mL) were firstly added into a glass bottle. After that, the NaHCO$_3$ solution (0.93 M, 1.1 mL) and the PSS-encapsulated Au NP solution were dropped under stirring. The mixed solution

was stirred for another 30 min, and then was washed by centrifugation several times and re-dispersed in water (10 mL) before further use. To prepare anatase-phase titania coated Au NPs, the thermal treatment of the washed and completely dried Au/TiO$_2$ nanostructures was putted into a box furnace in air at 450 $^{\circ}$C for 2 h for a heat treatment with a temperature increasing rate of 5 K·min^{-1}.

3.3.2 Characterization

The nano-morphologies of the core-shell samples were observed by transmission electron microscope (TEM) on an FEI Tecnai Spirit microscope operating at 120 kV. Figure 3.7 shows representative TEM images of the pure Au, Au/SiO$_2$ and Au/TiO$_2$ NPs, which were synthesized by growing SiO$_2$ or TiO$_2$ shell on pre-grown Au NPs as described above. They all show well-defined core-shell nanostructures with a clear boundary between the Au core and the shells. The diameter of the NPs is ~65 nm diameter with a ~25 nm diameter Au core and ~20 nm thickness SiO$_2$/TiO$_2$ shell. XRD patterns were obtained on a Rigaku SmartLab diffractometer equipped with Cu K radiation (Figure 3.8), and the measured diffractions peaks of Au/TiO$_2$ NPs was compared with standard PDF card of JCPDS 1-1172 (Au) and JCPDS 21-1272 (anatase TiO$_2$). The steady-state absorption spectra were recorded at room temperature by using a commercial UV-vis spectrometer (Shimadzu, UV-3600), as shown in Figure 3.9, a blank spectrum of the pure water solvent was recorded (Figure 3.11) for the baseline correction before measuring the samples' absorption spectrum. In the temperature-dependent absorption measurements, the bare TiO$_2$, Au/SiO$_2$ and Au/TiO$_2$ NPs were sonicated for 3 h, to eliminate agglomeration before performing experiments in the UV-vis. In order to vary the temperature of the sample, we used a temperature controller, connected with a heating unit inside the spectrometer chamber. A water flow was used to adjust and stabilize the temperature. A diagram of the top and side views of the heating unit is shown in Figure 3.10. The cuvette used here is a commercial Starna 10 mm UV-quartz rectangular cell with a small glass-coated magnetic stir bar inside. The absorption spectra were recorded from room temperature (~20 °C) to 80 °C in steps of 10 °C, while the NPs in solution were magnetically stirred.
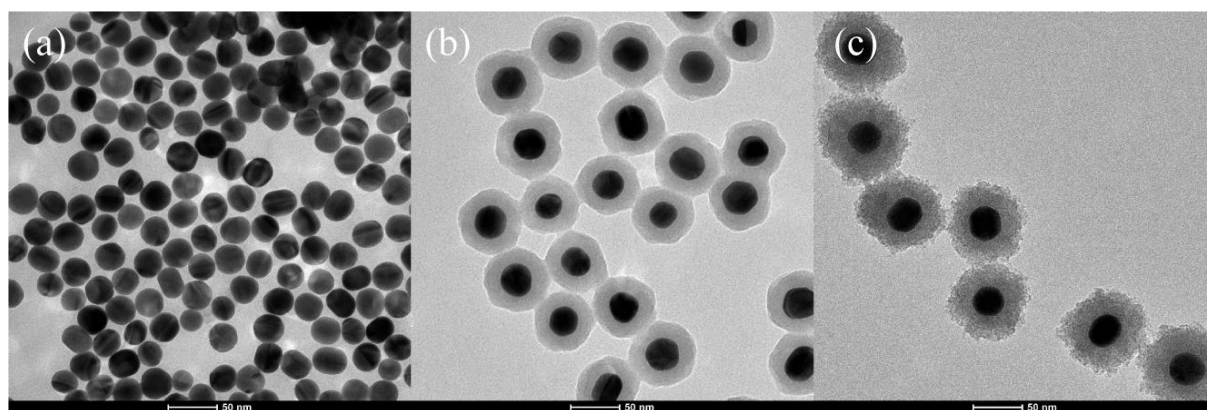
Figure 3.10 TEM images of the (a) pure Au NPs, (b) Au/SiO$_2$ NPs and (c) Au/TiO$_2$ NPs.
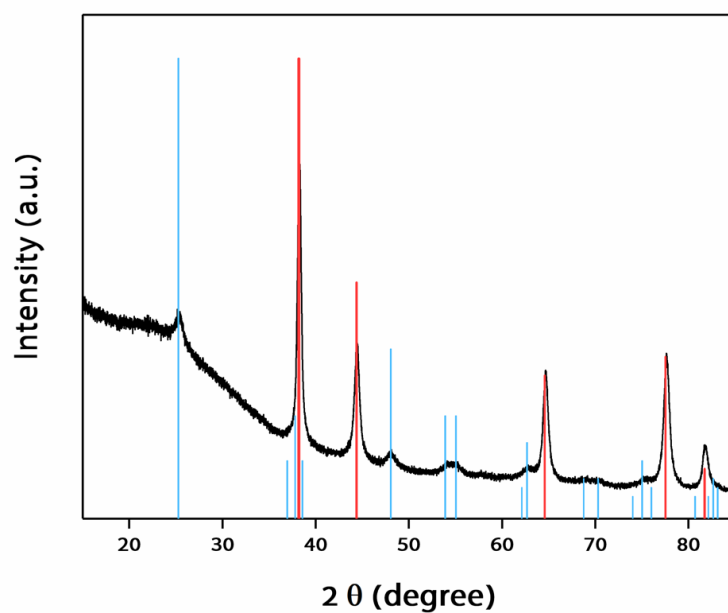
Figure 3.11 XRD pattern of the as-prepared Au/TiO$_2$ NPs, the measured diffraction peaks are compared according to the faced-centered-cubic (fcc) structure of Au (JCPDS 1-1172, red lines) and the anatase TiO$_2$ (JCPDS 21-1272, blue lines), data provided by CUHK.
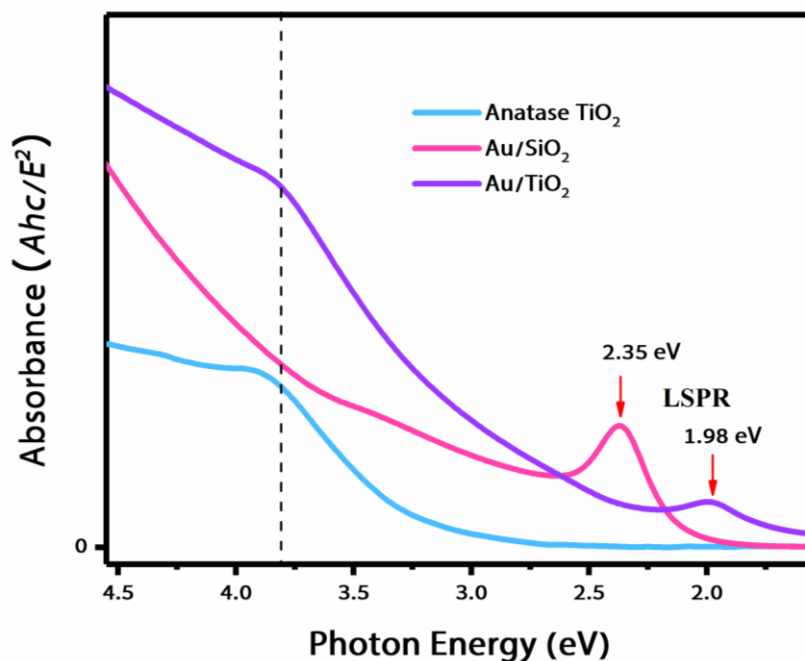
Figure 3.12 The steady-state absorption spectra of the measured anatase TiO$_2$, Au/SiO$_2$ and Au/TiO$_2$ NPs samples. The red arrows show the LSPR maximums of Au/SiO$_2$ and Au/TiO$_2$ NPs, respectively.
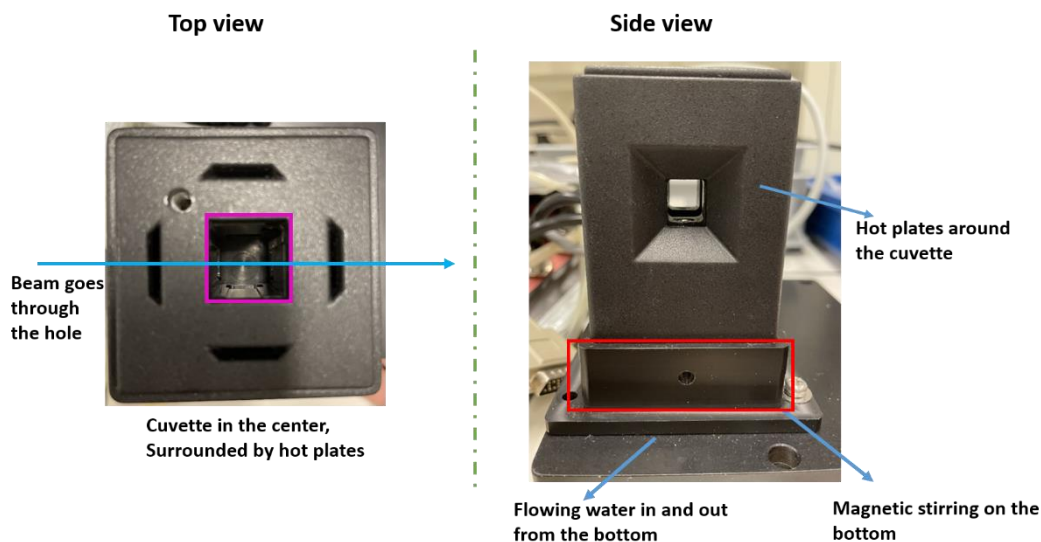
Figure 3.13 Top (left) and side (right) views of the heating unit used in the T-dependent absorption measurements, the whole unit is placed inside the UV-Vis spectrometer chamber and connected with a water flow and a temperature controller.
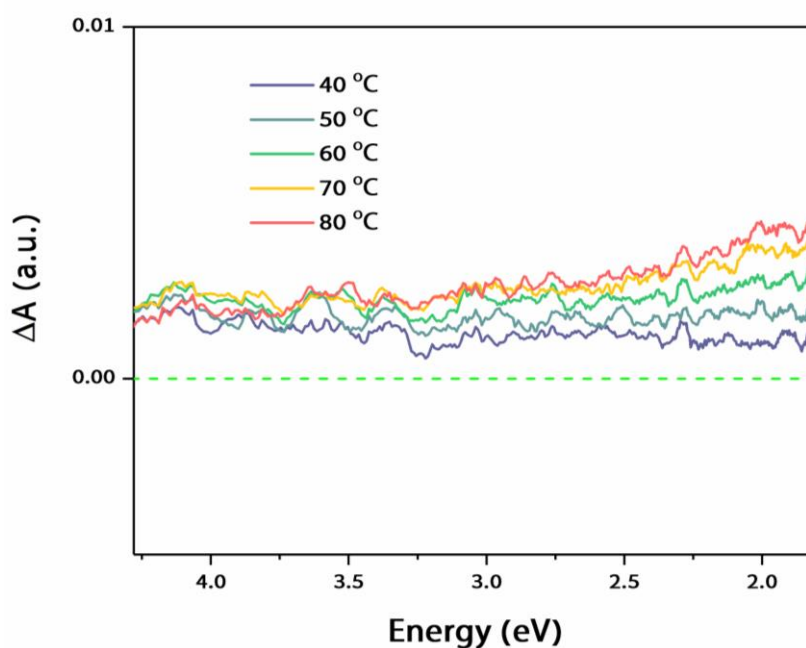
Figure 3.14 Absorption difference spectra of pure water, obtained by taking the difference of a spectrum at high temperature minus that at RT.

3.3.3 Sample environment

The sample is in an electrically rotating quartz flow cell by a rotation stage, the continuously rotating is to minimize the degradation and ensure that the sample is refreshed after each excitation, preventing artifacts and laser-induced damage upon long-term exposure. The flow cells are purchased from Starna

for optical path length of 0.1, 0.2 and 0.5 mm, besides, we used a drilled-flow cell which has thin apertures in each window to reduce the effects from the quartz wall (the wall is ~1 mm thick in the normal flow cell) as much as possible. The difference between the normal flow cell and drilled-flow cell is shown in Figure 3.12. For the measurements on large amount of bare anatase TiO_2 NPs, we used a peristaltic pump connecting with Teflon tubes, which is capable to flow the sample up to 1m/s, guaranteeing fresh sample for each laser shot. For the T-dependent steady-state absorption measurements, the cuvette used is a Starna 10 mm UV-quartz rectangular cell with a small glass-coated magnetic stir bar inside. The anatase TiO_2 sample was prepared in the meantime with acetic acid, which is known as a hole scavenger. The Au/SiO_2 and Au/TiO_2 NP samples are well dispersed in water solution and are sonicated for at least 3 hours before performing measurements.
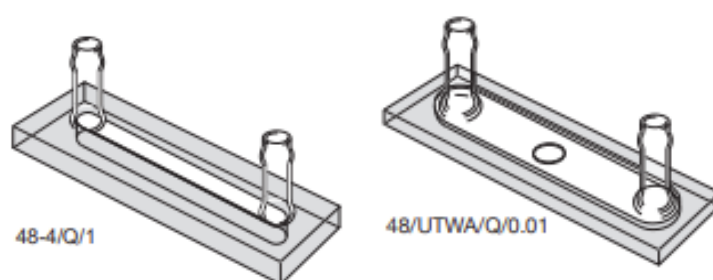
Figure 3.15 The used flow cells in the TA experiments, the left is the normal flow cell, the right is the drilled-one.

Chapter 4 Charge carrier relaxation in Au nanoparticles probed in interband transitions

The following chapter is adapted from the article:

4.1 Abstract

We report on ultrafast transient absorption (TA) studies of surface plasmon-excited ~25 nm diameter Au nanoparticles in solution, monitoring the surface plasmon resonance response in the visible (1.7-3.0 eV) and the inter- and intra-band transitions in the near-to-deep-UV (3.4-4.5 eV). The former reflects lattice heating by electron-phonon energy transfer, while the latter monitors charge carriers, i.e. the presence of excess holes and electrons, respectively, in the bands below and above the Fermi level. While the steady-state near-to-deep-UV absorption spectrum of Au is featureless, the TA spectra reveal three bands. Based on the band structure diagram of the bulk solid, we attribute these to inter- and intra-band transitions from the X and L symmetry points. The decay of the hot electrons and holes monitored via the inter-band transitions takes 150-180 ps. On the other hand, probing the intra-band transitions at the L symmetry points below the Fermi level reveals a hole relaxation on the tens of ps. These results show that after the initial ultrafast electron-electron and electron-phonon scattering processes, low-energy hot electrons above the Fermi level and holes below it remains in equilibrium with the hot lattice for several tens to hundreds of ps.

4.2 Introduction

Over the past two decades, nanoparticles (NPs) made of noble metals (Au and Ag) have attracted enormous interest[47,156,157] due to their potential applications in a wide range of fields, such as biomedical imaging, solar energy conversion, photocatalysis, etc. Noble metal NPs exhibit fascinating properties, which justify the intense interest for such applications: a) Their absorption spectrum is dominated by the so-called localized surface plasmon resonance (LSPR), which in many cases, is found in the visible to ultraviolet (UV) spectral range;[66] b) The optical cross-section of the LSPR is large; c) Its energy can be tuned by engineering the NP size and shape; d) Noble metal NPs exhibit an excellent photochemical stability and are non-toxic.

Surface plasmons can decay either radiatively[158] via the emission of a photon or non-radiatively through the generation of hot charge carrier (electrons and holes) pairs (so-called Landau damping). These photo-excited hot carriers can potentially be used to directly drive energetically demanding chemical reactions,[156,159,160] or be transferred to a semiconductor for photovoltaic[161,162] and photoelectrochemical

applications.[17,163] These potential applications call for a detailed description of the charge carrier dynamics and their fate over several decades of time scales. Because the initial events such as Landau damping occur on the 10s of femtoseconds (fs) time scale, ultrafast spectroscopy has played an important role in probing the charge carrier dynamics. Our interest here focusses on the case of Au NPs that have played an irreplaceable role in the advancement of the field of nanoplasmonics. More specifically we focus on probing the fate of photo-excited charge carriers, all the way to their complete relaxation.

Detailed ultrafast photoemission and optical pump-probe studies have already been carried out on bulk Au surfaces[60,61,68,164] and on colloidal NPs.[54,55,64,88,165,166]. The general picture that emerged is that after laser excitation, electron-electron scattering occurs within a few 10s of fs between the initially excited electrons. This leads to a Fermi-Dirac distribution characterized by a large effective electron temperature.[116] Energy exchange with phonons occurs on a slower time scale, typically several picoseconds (ps), by electron-phonon coupling,[167,168] leading to heating of the lattice until the electron and lattice temperatures equalize. At this point, the NP is in an internal thermal equilibrium at a uniform temperature, but not with its environment that is still at the initial ambient temperature. Eventually, heat dissipation to the environment occurs and cooling of the hot NPs takes place on time scales of hundreds of ps.[69,70,76] The generated electrons and holes are considered 'hot' if their energies are larger than the thermal excitations at ambient temperatures. As mentioned above, these hot carriers are essential in order to induce physical or chemical processes, but their ability to do so is dictated by their energy and their time scale of the cooling.[116]

The light absorption and scattering are strongly enhanced at the LSPR due to the electron oscillation,[169] and the increase in NP lattice temperature upon excitation of the NPs plasmon resonance is typically a few degrees Celsius to hundreds of degrees Celsius in the case of Au NPs (diameter, ca. 20-120 nm). Their cooling is significantly affected by their size, shape and environment.[29,75–77,170] This implies that at the LSPR, thermal effects are prominent. These effects translate into shifts/broadenings of the LSPR band because the lattice temperature affects the surface of the NPs.[82,84] By probing at different wavelengths at and around the LSPR, Del Fatti et al[29,76] found that the optical properties of the sample are also modified by the heating of the environment. In fact, the measured time-resolved signals were found to reflect changes in the genuine NP temperature only when probing away from the LSPR. Consequently, while probing the latter's response provides a valuable thermometer of the NP and its local environment, caution must be exercised when relating the LSPR response to actual hot charge carriers.

Alternative methods such as time-resolved X-ray scattering (XRS)[85] and Au L_3-edge X-ray absorption spectroscopy (XAS)[171] have also been implemented to probe the response of LSPR-excited Au NPs. These approaches provide a direct local (XAS) and global (XRS) view of the lattice structure changes upon heating via LSPR excitation. XRS experiments were performed with 100 ps temporal resolution on ~100 nm diameter Au NPs in water, following excitation at 400 nm. For low excitation powers, the

initial lattice heating is followed by cooling on the nanosecond (ns) time scale, which was attributed to a transfer of heat to the solvent. The XAS studies were also carried out with 100 ps resolution on much smaller (1.8 nm diameter) colloidal Au NPs in ethanol. The transient XAS spectra were interpreted in terms of an 8% expansion of the Au–Au bond length and a large increase in disorder associated with the melting of the NPs. Recovery of the ground state was found to occur with a time constant of ~1.8 ns, arising from thermalization with the environment. A summary of the kinetic parameters derived from optical and X-ray studies on Au films or NPs is given in Table S1. One should note however that the discrepancies showing up in this table, in particular, between the optical and X-ray studies are, among others, due to the different fluences used in these studies and additional effects, such as melting[85] and cavitation[77,172] also affecting the results. While photoemission studies are sensitive to pure electronic effects and have been implemented only on thin films, the various optical and X-ray probes mentioned above are sensitive to thermal and structural effects of the NPs, and in the case of the visible probes, also to heating of the solvent environment. In short, these studies deliver detailed information about the long-time cooling processes assuming they are entirely thermal. Thus, the methods used so far for NPs monitor thermal effects but do not monitor the actual evolution of the hot charge carriers.

In order to circumvent this problem, here we adopt a different strategy based on the use of a broadband probe continuum in the deep-UV (3.4-4.5 eV)[89,152] that opens observation windows spanning the inter-band transitions. This is accompanied by parallel experiments probing the NP thermal response in the visible range (1.7-3.0 eV) around the LSPR band. Thus by monitoring the TA response of the LSPR-excited Au NPs, in the region of the LSPR and of the inter-band transitions, we are capable of monitoring both the thermal and the charge carrier relaxations over several hundreds of ps. We find that the decay of the inter-band transitions is commensurate with that of the LSPR. Specifically, the inter-band transitions identified as monitoring the electrons suggest that these return to their initial bands (below the E_F) on a relatively long-time scale of 150-180 ps, slightly shorter than the time scale for the lattice cooling (~250 ps to ns's, see Table S1), while the inter-band transition sensitive to the holes, exhibits a similar time scale, suggesting that hole relaxation occurs on the tens of ps time scale. Thus, the charge carriers remain in equilibrium with the lattice and relax on a time scale commensurate with thermal relaxation.

4.3 Experimental section

4.3.1 Sample preparation

Au nanoparticles (NPs) of ~25 nm diameter were synthesized using a seed-mediated growth method, as reported in ref.[140]. Specifically, a cetyltrimethylammonium bromide (CTAB) solution (0.1 M, 9.75 mL) was first mixed with a HAuCl4 solution (0.01 M, 0.25 mL), followed by the rapid injection of a freshly prepared, ice-cold NaBH4 solution (0.01 M, 0.60 mL) under vigorous stirring. The resultant solution was kept under gentle stirring for 3 h at room temperature. The as-prepared seed solution (0.24 mL) was

injected into a growth solution made of CTAB (0.1 M, 19.5 mL), water (380 mL), HAuCl4 (0.01 M, 8 mL), and ascorbic acid (0.1 M, 30 mL) afterwards. The reaction mixture was gently mixed well and then left undisturbed overnight at room temperature. The resulting Au NPs were washed and concentrated three times into water by centrifugation and re-dispersion.

4.3.2 Steady-state spectra

The steady-state absorption spectra were recorded at room temperature using a commercial UV-Vis spectrometer (Shimadzu, UV-3600). Before measuring the absorption spectrum of the sample, a reference spectrum of the pure solvent (water) was recorded for the baseline correction. The Au NPs were measured at room temperature with sampling interval of 1.0 nm. To convert the nm to eV scale, we followed the Jacobian conversion method.[153] The wavelength is converted to energy using $E = {hc}/{\lambda}$, and the signal values themselves must be scaled by $({hc}/{E^2})$, where E represents the photon energy, h is the Planck constant, c is the light speed and λ represents the wavelength.

4.3.3 Transient absorption set-up

The experiments were performed using two different set-ups: one for tunable visible-pump/broadband visible-probe and the other for visible-pump/ broadband deep-UV-probe.

a) For the broadband visible-probe set-up, a 1 kHz regenerative amplifier provides 30 fs pulses at 800 nm with ~720 μJ/pulse. A non-collinear optical parametric amplifier (NOPA) is used to generate visible pump pulses (550 nm, 2.25 eV) with ~15 nm bandwidth and 2-4 μJ/pulse, while the probe beam is focused onto a CaF2 plane for white light generation (450-750 nm, 1.65-2.75 eV range). The typical pump and probe focus beam diameters are ~150 μm and ~80 μm, respectively.

b) For the broadband deep-UV probe set-up,[152,173] a 20 kHz Ti:Sapphire regenerative amplifier (KMLabs, Wyvern500), providing 50 fs/0.6 mJ pulses at 800 nm pumps a NOPA to generate sub-90 fs visible pulses of 13 μJ/pulse in the 510-740 nm (1.68-2.43 eV) range. About 60% of the output is used as the pump pulses. Particularly we use a multi-layer mirror to obtain only green pump beam (2.0-2.4 eV, centered at ~2.2 eV). The pump pulses are further compressed by chirp mirrors to deliver <20 fs duration. The remaining 40% NOPA output is used to generate the broadband UV probe pulses with ~100 nm bandwidth through an achromatic doubling scheme.[174] A half-wave plate is used to set the relative polarization between the pump and probe at the magic angle (54.74°) to avoid photo-selection effects. The typical spot sizes of the pump and probe are ~120 μm and ~50 μm full widths at half maximum (FWHM),

respectively. In all measurements, the pump fluence is ~330 $\mu J/cm^2$ (with ~10% uncertainty due to the laser power measurement and laser beam spot size). The sample is in a 0.2 mm thick quartz drilled-flow cell and rotated by an electronic motor to prevent photo-damage.

4.4 Results and discussion

The identification of inter-band transitions requires the band structure (BS) diagram which has been calculated by several groups using *ab-initio* many-body perturbation theory on bulk Au at different levels of approximation within the GW approach.[20,22,23] Figure 1 shows the calculated BS diagram using the quasiparticle self-consistent GW (QSGW) scheme,[22] which we have selected because it provides the best agreement with angle-resolved photoelectron spectroscopy (ARPES) data on Au crystal[24] and is consistent with the calculation of the Au dielectric function.[25] The topmost 5d-band below the E_F are shown in red, while the blue one is due to the 6sp-band, which spans both the region below and above the E_F. The ARPES data only probes the region between the L and Γ points,[24] and no experimental data are available around the X points. We therefore use this BS diagram here to predict the transition energies at the X points. In order to simplify the discussion of our results and because of the different nomenclatures used in the literature for the energy points of the BS diagram, we labelled them from 1 for the first point above the E_F, in incremental order of decreasing energies, as shown in Figure 1. We stress that the use of the BS diagram for the bulk solid is likely to yield energies that deviate from those measured in the confined geometries of NPs, as was already shown to be the case for semi-infinite metal slabs[23] and thin films of precipitated NPs.[93] Furthermore, as will be seen below, the energies derived from the calculated BS diagram and the experimental ARPES data for bulk Au already show some degree of deviations. Therefore, when using the BS diagram of the bulk solid to guide the interpretation, we should bear in mind that energies are likely different. Finally, the dipole-allowed inter-band transitions dominate the optical response in bulk Au and as a consequence, electrons are not produced with a high energy content while holes are.[23] On the contrary, in nano-confined geometries such as NPs, the transitions no longer need to be vertical, opening the possibility of geometry-assisted intra-band transitions without involving phonons. This results in hotter electrons under LSPR excitation than in the bulk case.[23]

The absorption spectrum of the Au NPs (~25 nm diameter) used here is shown in Figure S1 of the Supporting Information (SI). The LSPR lies at ~2.3 eV. On its high energy side, a featureless continuum absorption grows towards shorter wavelengths, which is due to inter-band absorption and scattering. The inter-band absorption arises due to electronic transitions of the system below and above the Fermi level (E_F). It should be stressed that the onset of these transitions already lies on the blue side of the LSPR band,[165,175] so that when exciting the latter, inter-band transitions can also be excited. The lack of spectral features at energies above the SPR band hinders the identification of the inter-band transitions. However, studies have shown that the extinction coefficient of bulk gold, which reflects its energy band

structure, exhibits features at ~2.5 eV, ~3 eV and at ~4 eV.[26,93,176] The first two have been attributed to transitions from the uppermost 5d-valence electron bands (red in figure 1) to states in the 6sp bands (blue in figure 1) just above the Fermi level (E_F). According to figure 1, these transitions would occur from around the L_3 and X_2 points to the region where the 6sp crosses E_F and higher. The band at 4 eV was attributed to transitions from lower-lying d bands to the 6sp band near the X point (i.e. transitions from $X_{3,4}$ to X_1), as well as the L_2-L_1 transition. We will revisit these assignments when we present our TA spectra.
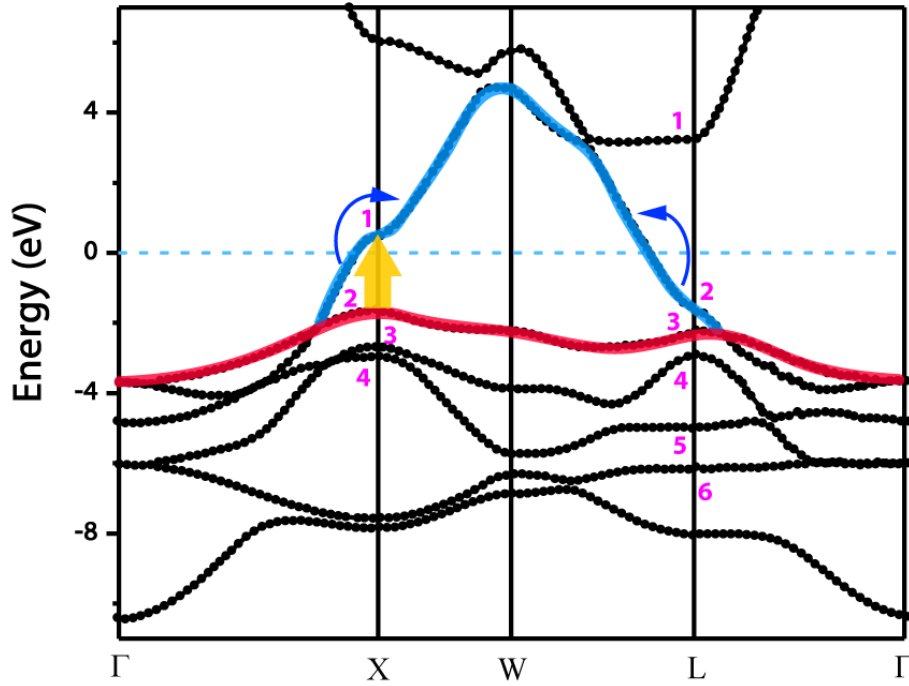
Figure 1: Calculated band structure diagram of bulk Au.[22] The Fermi level is set to 0 (dashed cyan line). The various critical energy points at the L and X symmetries are numbered starting from the first point above the Fermi level in incremental order going to lower energies. The red line disentangles 5d-character topmost occupied band, while the blue line indicates 6sp-band. The wide vertical yellow and curved blue arrows show inter-band and plasmon-assisted intra-band excitations, respectively.

A critical point of the band structure is defined as the energy where $d(E(k))/dk=0$ for two bands separated by the energy E at the crystal momentum k. When $d(E(k))/dk{\neq}0$, the joint density of states is reduced but inter-band transitions are still possible and non-negligible, especially if one of the bands is relatively flat, as is the case with the 5d-band near the X- and L- symmetry points. The $d(E(k))/dk=0$ range is relatively extended around the $X_{2\text{-}1}$ transition, which is well within our pump pulse range. The next such transition would be $L_{2\text{-}1}$ but it lies too high in energy. Mostly $d(E(k))/dk{\neq}0$ transitions from the upper 5d-band to the 6sp-band above E_F are found between the L and W points. For the near-to-deep-UV probe studies, we used a broadband pump pulse spanning from 2 to 2.4 eV, which fully encompasses the LSPR

band of the sample. The use of a broadband pump pulse was needed to enhance the excitation yield. This implies that in addition to excitation of the LSPR in which electrons are transferred from the lower 6sp band to above the E_F, as shown by the curved arrows in Figure 1, inter-band transitions near the X symmetry points (wide vertical yellow arrow) will also be excited, where the 5d bands are relatively flat. The bandwidth of the pump pulse is however not sufficient to induce transitions from the L and W points. In summary, our pump pulse excites the LSPR promoting electrons from lower 6sp band to above the E_F at both the X and L symmetries, as well as inter-band transitions at and around the X_{2-1} transition. As a consequence, holes are created at the X_2 and L_2 points,[91,177,178] while the region around X_1 and the 6sp band between L and W above E_F will have an excess of electrons upon excitation.
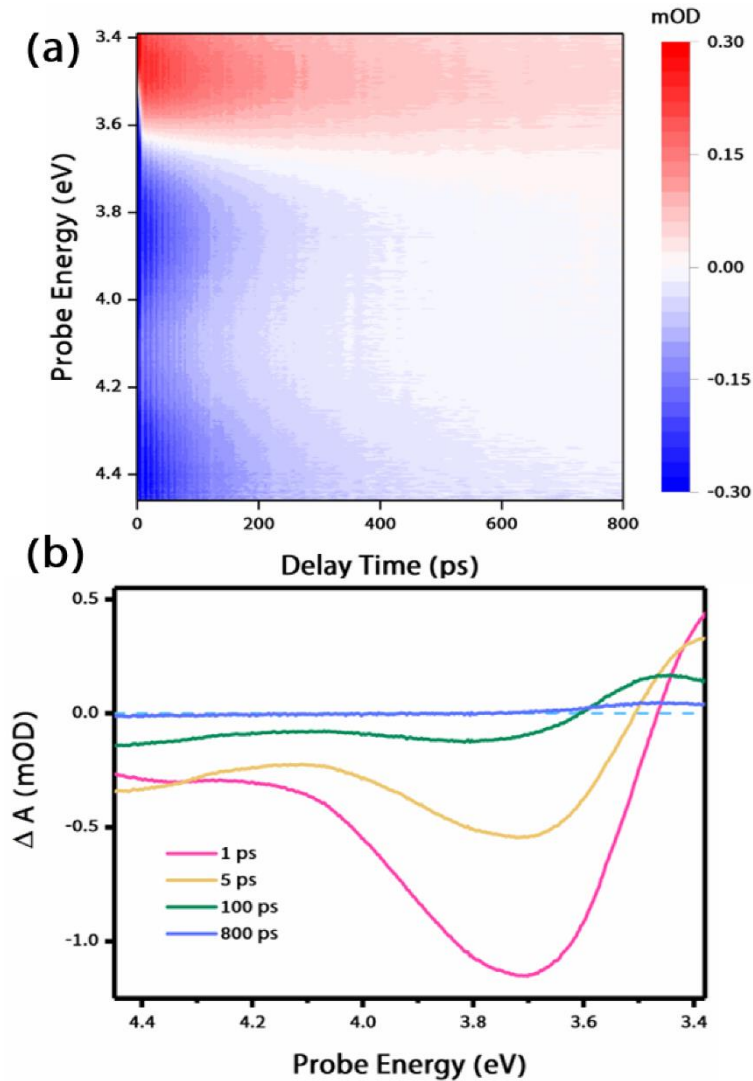
Figure 2: Time-energy transient absorption (TA) map (a) and TA spectra (b) at different time delays of the Au nanoparticles excited by a broadband 2.0-2.4 eV pulse and probed in the 3.4-4.5 eV region.

We now turn to the estimate of the possible inter- and intra-band transitions in the region of our UV probe continuum using the ARPES data and the BS diagram of bulk Au (Figure 1).[22] The inter-band transitions are directly sensitive to the relaxation of charge carriers, and the estimated transition energies are given in Table S2. In the case of the L transitions, deviations of 0.15-0.45 eV occur between the experimental and calculated values for bulk Au, which should be borne in mind when using the calculated X transitions, and more so when extending them to the case of NPs. According to Table S2, our near-to-deep-UV (3.4 to 4.5 eV) probe continuum can monitor the following inter-band transitions after depletion of the L_2, X_2 points and population of the X_1 point: a) The $L_2{\rightarrow}L_1$ transition at ~4.3 eV according to the ARPES data and the BS diagram (this assignment is consistent with literature[26,93,94,176]), and the $X_4{\rightarrow}X_1$ transition at ~3.5 eV, according to the BS diagram, both having a negative sign in the TA; b) the $L_6{\rightarrow}L_3$ transition (we are also considering the L_3 point for reasons that will be discussed later) at ~3.8 eV and the $L_5{\rightarrow}L_2$ transition at ~3.95 eV, which both have a positive TA signal. Thus, within our probe window, two clearly separate negative bands and two energetically close-lying positive ones should show up based on the high symmetry points.

Prior to presenting the UV transients, we benchmarked our results with respect to those of the literature, by revisiting the ultrafast response of LSPR-excited Au NPs, probing in the visible region. Our results are presented in § S3 of the SI and Figures S2 to S4. Figures S2 and S3 show that upon excitation, the absorption at the centre of the LSPR band decreases, while it increases in the wings. This behaviour reproduces the results of Logunov et al[54] and is typical of the thermal expansion of the NP lattice.[65] The transients remained unchanged during the first 20 ps, as can be seen from the normalized TA spectra in Figure S3. The temporal behaviour at the centre and in the wings (Figure S4a) is also identical as can be seen from Figure S4b, which shows the overlapped traces. The inset in Figure S4b shows the time trace at 2.35 eV in the 5 to 400 ps window. It can be fit by a single exponential with a decay time of ~260 ps. As established previously, the kinetics of Au NPs strongly depend on size, excitation fluence, solvent, etc., and Table S1 hints to these. In particular, we identify the ~260 ps decay as thermal cooling of the NPs, in reasonable agreement with previous studies.[54,55,64,116,171,179]

Probing in the deep-UV yields the TA time-energy plot in Figures 2a and S5. Figure 2b shows TA spectra obtained by taking cuts of Figure 2a at time delays of 1, 5, 100 and 800 ps. Figure S5 shows the time-energy TA plots for different time windows. In Figures 2a and b, one can distinguish three main transient features: two negative (bleach) bands centred at ~4.4 eV and ~3.8 eV and a positive (induced absorption) one at ~3.4-3.6 eV (cut off by the red-edge limit of our detection). Although the high energy side of the LSPR in the steady-state absorption spectrum is featureless (Figure S1), in these figures the TA exhibits clear spectral features. This arises from the cancellation of the scattering background by subtracting the unexcited sample spectrum from the excited one.[39,90] All the bands decay on 100s of ps, but at somewhat different rates. Based on Table S2 and bearing in mind the likely deviations in energy between bulk and nanostructured Au, we attribute the bleach (negative) bands at ~3.8 eV and ~4.4 eV

in Figure 2 to the $X_4 \rightarrow X_1$ (with a possible contribution from $X_3 \rightarrow X_1$) and the $L_2 \rightarrow L_1$ inter-band transitions, respectively. The induced absorption (positive) band around 3.4-3.6 eV is attributed to the near-lying $L_5 \rightarrow L_2 / L_6 \rightarrow L_3$ transitions (see Table 1). For the latter, the energies deviate significantly from the ARPES-derived values, which we attribute to the fact that the latter concern bulk Au. Thus, the present assignment identifies the two negative TA bands as $X_4 \rightarrow X_1$ and $L_2 \rightarrow L_1$ transitions due to an excess of electrons at X_1 and an excess of holes at L_2, while the positive TA band is due to an intra-band transition that detects the excess of holes at L_2 (and L_3). It should be stressed that this assignment is quite robust, since the signs of the various TA signals exclude any alternative possibilities. In particular, it is difficult to conceive an alternative explanation to the occurrence of a photo-induced absorption (positive) band in the TA.

Table 1: Energies (in eV) and signs of the bands observed by transient absorption spectroscopy, along with their estimated energies and assignments based on Table S2 (the L energies are derived from ARPES data while the X energies are from the calculated BS diagram, both for bulk Au). Corresponding exponential decay time constants (τ_1, τ_2), amplitudes (A_1, A_2), oscillation period ($\tau_{osc.}$) and damping constants (τ_D). All times are in picoseconds.

Probe band energy (sign)	Estimated energies/Assignment	τ_1	τ_2	A_1	A_2	τ_{osc}	τ_D
2.35	LSPR	2.3±0.1	258.2±35.3	90%	10%	-	-
4.4, negative	4.3 eV/$L_2 \rightarrow L_1$	-	178.2±12.2	-	-	9.6±0.1	30.0±7.7
3.8, negative	3.5 eV/$X_4 \rightarrow X_1$	3.1±0.2	153.3±8.5	79%	21%	10.2±0.2	17.5±5.3
3.4-3.6, induced absorption	3.8 eV/$L_6 \rightarrow L_3$ 3.95/ $L_5 \rightarrow L_2$ (main)	-	247±11.9	-	-	9.4±0.4	10.9±4.1

Figure 3 shows the kinetic traces recorded at the energies of 3.4 eV, 3.8 eV, 4.4 eV and the trace recorded at the LSPR (2.35 eV), along with the fits. The extracted decay time constants τ_1, τ_2, amplitudes A_1, A_2, oscillation period τ_{osc} and damping constant τ_D are given in Table 1. The 2.35 and 3.8 eV traces exhibit a bimodal decay with an initial few-ps component, followed by a slower component of 100s of ps, while the 3.4 and 4.4 eV traces exhibit only one slow component. From Figures 3 and Table 1, we note the following:

a) The short components of the 2.35 eV and 3.8 eV traces drop within a few ps to 15-25% of their initial value, while the 3.4 and 4.4 eV traces do not. The drop is faster and more significant in the case of the 2.35 eV trace.

b) The oscillatory pattern is identical in period (~10 ps) and phase for the 3.4, 3.8 and 4.4 eV traces. It rides on the exponentially decaying signal and lasts up to ~80 ps, while undergoing a damping with a constant of ~10-30 ps. Such coherent oscillations have already been reported upon probing in the region of the LSPR band, and were attributed to coherent acoustic phonons, due to a breathing mode of Au NPs.[71,88,179] However, here they are observed for the first time via inter- and intra-band transitions. Figures S5a and b show that the central energy of the bands does not change but their oscillator strength does (amplitude modulation), typical of a coupling of the electronic transitions to the acoustic phonons.[180]

c) The long component in all traces decays on a comparable time scale (~200 ps) but some differences appear. The decay time scale of 4.4 eV signal is intermediate between the slower 3.4 eV signal and the faster 3.8 eV signal, the latter reaches zero by ~600 ps (Figure 2a). While the 2.35 eV signal decays the slowest.

We fit the kinetic traces (detailed methods in § S2 of the SI) using a function consisting of a biexponential component and a damped cosine component for the oscillatory part in the case of the 3.8 eV trace, and a mono-exponential with a damped cosine component in the case of the 3.4 and 4.4 eV traces. Finally, the 2.35 eV trace was fit with a biexponential decay function. All fit functions were convoluted with the instrument response function (IRF, see § S1 and Figure S6 of the SI). Figures S7 to S9 show the decomposition of the time traces into kinetic and oscillatory components for the 3.8, 3.4 and 4.4 eV traces, respectively. It is worth noting that no coherent oscillations are observed in our visible probe TA experiments. A more detailed discussion of the coherent oscillations is beyond the scope of this paper and will be presented in a forthcoming publication.

Based on the assignments of Table S2, the 3.8 eV bleach band initially interrogates the presence of electrons at the X_1 point via the transition from the X_4 point. The fast, initial drop (~4 ps) is attributed to the fact that the electrons quickly relax away from X_1 due to electron-electron and electron-phonon scattering. This initial process is also probed in the visible (2.35 eV) although the time scale seems shorter in this case. We attribute this difference to the fact that the latter monitors pure electron-electron and electron-phonon scattering processes, while the former includes electron relaxation of the 6sp band to above the E_F at the X_1 point. The long component reflects the subsequent relaxation of hot electrons back to the initial bands below the E_F. Its time constant implies that the electrons require ~150 ps to perform this relaxation. The fact that 3.8 eV bleach only monitors electrons at the X_1 point implies that the electrons remain for ~150 ps in its vicinity, a situation enabled by the fact that the X_1 point is just above the E_F and considering that the NP lattice has not yet fully thermalized,[29,76] the electrons remain hot, in equilibrium with the lattice. The 4.4 eV band monitors the depletion of electrons (i.e. the holes) formed at the L_2 point upon LSPR excitation. For this reason and contrary to the 3.8 eV band, the 4.4 eV trace lacks a short component, as it is not sensitive to the fast non-equilibrium scattering processes taking place after LSPR excitation. The fit of this trace yields a value of ~180 ps, which is close to that

of the 3.8 eV band and leads us to conclude that electron relaxation back to the valence band (VB) is nearly identical at the X and L points. In principle, the same time scale should show up at the positive induced absorption 3.4-3.6 eV band, if it would only monitor the holes at L_2, via the $L_5 \rightarrow L_2$ transition. However, the fit of this trace yields a value of ~250 ps, which is significantly larger than for the two bleach bands. As already mentioned, the assignment of bands is based on the BS diagram of the bulk, whose extrapolation to NPs is uncertain. In this respect, it is not fully excluded that holes are also created in the 5d band between the L and W upon direct inter-band excitation, which then migrate to the L_3 and L_2 points that could be monitored by the $L_6 \rightarrow L_3$ and $L_5 \rightarrow L_2$ transitions, respectively. This would imply that the longer time scale (~250 ps vs ~180 ps) is due to an additional hole relaxation near the $L_{2/3}$ points on the tens of ps time scale for the holes.
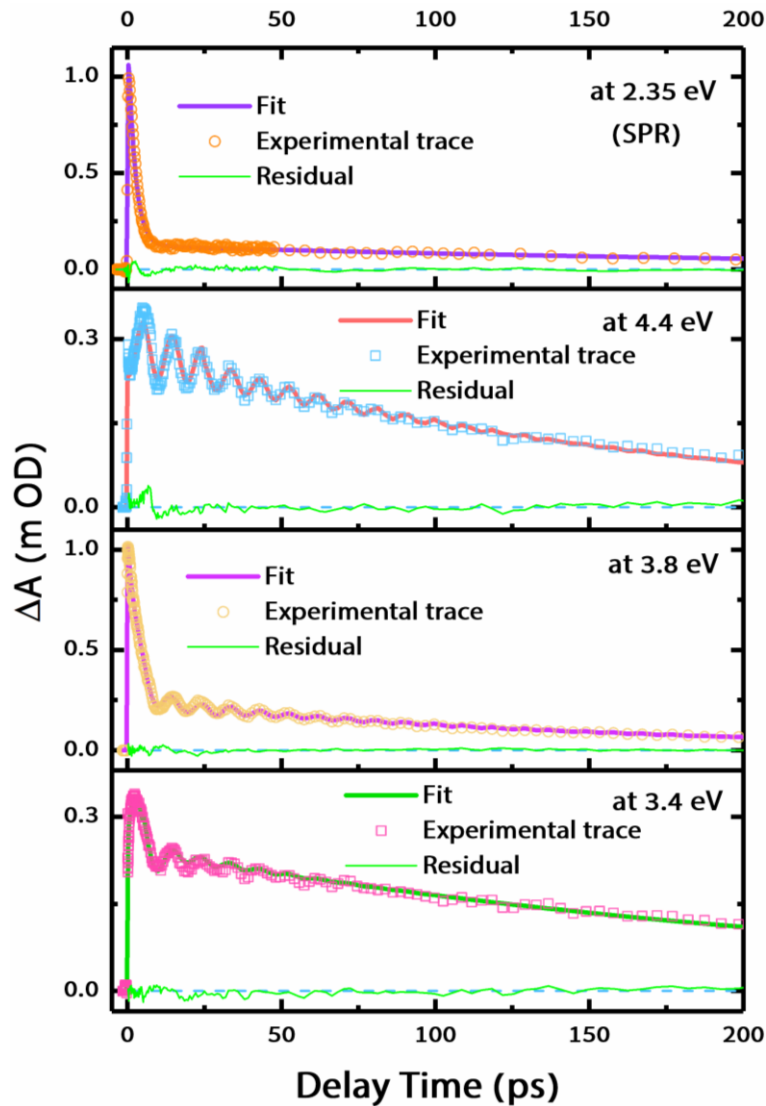
Figure 3: The fitting of the kinetic traces probed at 2.35, 4.4, 3.8 and 3.4 eV. The dots are experimental data, and the solid lines represent the fitted time traces. The cross-phase modulation region at time zero is removed before the fitting. The fitting function contains one or two exponential functions and damped cosine terms. The functions are also convoluted with a Gaussian response that accounts for the IRF.

What appears from the above is that hot electrons generated by LSPR excitation remain above the E_F and require typically 150-180 ps to relax back to the initial bands. We also suggest that hot holes undergo a slow relaxation in tens of ps. However, visible probe studies suggested that thermal energy stored in the form of lattice heat remains for a longer time of ~250 ps in the NP, and therefore there is a time window during which the electrons above the E_F and the lattice are indeed in thermal equilibrium. Thus, lattice thermal relaxation and cooling of charge carriers leading to their return to below the E_F on commensurate time scales, suggesting that they are strongly intertwined. Given that the LSPR-induced heating of Au NPs depends on several parameters such as their shape, size, solvent environment and the laser fluence etc., correspondingly, the lifetime of 'hot' electrons can be controlled by tuning these parameters.[88]

The above analysis ties the charge carrier relaxation to the thermal relaxation suggesting that hot carriers exist by virtue of the hot lattice. Our interpretation is largely based on the BS diagramme of bulk gold, which as we mentioned is surely different for NPs. Of course, an alternative interpretation would be that the inter-band transitions also report on thermal effects, just as the LSPR response does. While we cannot fully exclude this scenario, we believe that our above interpretation is more probable due to the fact that: a) we have used three inter-band transitions to monitor the charge carrier relaxation at different points of the BS diagramme. It would be remarkable that thermal effects would be operative in a similar fashion on all three; b) a thermal effect on the electronic structure would, we believe, be most visible close to the Fermi level, i.e. the points of the BS diagramme closest to E_F would be most affected by thermal effects. However, of these the X_4-X_1 transition is the only one that monitors charge carriers just above E_F, yet its decay is identical to the L_2-L_1 transition that occurs between points far from E_F. Finally, the intra-band L_5-L_2 transition, between points below and far off from the Fermi level, has a different decay time; c) we also note that the temporal profile of the LSPR and of the inter-band transitions is different, with the 3.4 and 4.4 eV signals showing no short component, while the 2.35 and 3.8 eV ones show it. Interestingly, the 3.8 eV probe is the only one that monitors electrons in the region where the LSPR excitation creates them. For all these reasons, we believe that the inter-band transitions do monitor electronic effects even if these are commensurate with the lattice thermal cooling.

The fact that thermalized hot (i.e. above the E_F) electrons can survive for such a long time is interesting in relation to the applications mentioned in the introduction. In photovoltaics, Au NPs have been proposed as sensitizers of transition metal oxide semiconductors (SC) such as anatase TiO_2.[46,181,182] In this configuration, hot electrons with an energy larger than the Schottky barrier can be transferred to the conduction band of the SC. This process is however inefficient because the fast relaxation through electron-electron and electron-phonon scattering tends to decrease the energy of the electrons to below the Schottky barrier. For the TiO_2−Au interface, the latter is believed to be in the 0.9−1.2 eV range.[183–185] The long-lived hot electrons cannot overcome such a barrier but they can tunnel through it.[186,187] Besides, those slowly relaxing electrons and holes can also be exploited for hot electron-mediated

chemical reactions by their direct capture by molecules adsorbed on the surface of plasmonic nanostructure.[160,168,188] This can take place either by hot electrons directly injecting into unoccupied orbitals of target molecules or, if the hot electrons with higher kinetic energy and higher momentum than other electrons at the Fermi surface may transfer sufficient energy to break chemical bonds of the molecules or assist in bond breaking for chemical reactions. In this respect, the long relaxation/cooling time of the photo-generated electrons reported here may present a significant advantage. These are avenues that call for further studies as the present results need to be confirmed for NPs of different sizes and shapes and for different metal-SC nanostructure configurations. Finally, the relatively long cooling of the hot holes (tens of ps) suggested by the present results is a very exciting avenue to explore in photo-redox reactions. On a more fundamental aspect, the present results call for a detailed theoretical investigation of the electronic (band) structure of NPs, and a detailed description of the effect of acoustic phonons on the inter-band (electronic) transitions.

4.5 Conclusions

In conclusion, using ultrafast TA spectroscopy on Au NPs with a deep-UV probe, we have identified several transient bands corresponding to inter- and intra-band transitions, which we have used to monitor the decay of electrons and holes upon LSPR excitation. We find that relaxation of electrons back to the VB takes place in about 150 ps, while holes relax over tens of ps. Considering that the NPs lattice thermal relaxation takes ~250 ps, the hot lattice maintains the electrons above the E_F for a significantly long time, whose occurrence is promising for several applications and calls for further study.

4.6 Supplementary information

4.6.1 Determination of the instrument response function

The instrument response function (IRF) was determined by measuring the FWHM of the cross-phase modulation (CPM) at time zero of the pure water solvent (in a 0.2 mm optical path length drilled flow cell). We adopted a procedure by fitting the CPM signal with a function composed of a Gaussian and its first and second derivative as below:[155]

$$G(t) = \frac{1}{\sigma\sqrt{2\pi}} e^{-\frac{t^2}{2\sigma^2}}$$

$$G(t)' = \frac{(c-t)}{\sigma^3\sqrt{2\pi}} \exp\left(-\frac{(t-c)^2}{2\sigma^2}\right)$$

$$G(t)'' = \frac{(t^2 - 2ct - \sigma^2 + t^2)}{\sigma^5\sqrt{2\pi}} \exp\left(-\frac{(t-c)^2}{2\sigma^2}\right)$$

of which the FWHM $= 2\sigma\sqrt{2\ln(2)}$, t is the time variable, and c is the offset of time zero. The IRF was found to be ~250 fs (Figure S6).

4.6.2 Fit of the kinetic traces

The fit was performed by using the following Eq. 3.4:

$$I(t) = \left\{ \left[\sum_{i=1}^{n} A_i \cdot e^{-(t-c)/\tau_i} \right] + \left[A_{osc} e^{-(t-c)/\tau_D} \cdot \cos\left(\frac{2\pi}{\tau_{osc}} \cdot (t-c) - k \right) \right] \right\} * \mathrm{IRF}(t)$$

where t is the time variable, n is the number of exponential decay functions used, c is the time zero offset, A_i is the decay function amplitude, A_{osc} is the oscillation component amplitude, k is the phase of the cosine function, τ_i represents the decay time constant, τ_{osc} represents the oscillation period and τ_D represents the damping constant.

In the fitting, we take into account the contributions: i) the promptly rising within the IRF; ii) a long-lived decaying kinetic (with a short-lived decay at 3.8 eV); iii) damped cosine functions for the coherent oscillations.

The fit function contains two terms: one is the mono- or bi-exponential decay function, depending on the trace; the other is the damped cosine function. The above two terms are convoluted with the IRF, taken as a Gaussian with ~250 fs FWHM (determined in S1).

The fit was implemented in OPTIMUS[155] and Matlab. Firstly, we fitted the long-term time trace over the 50 ps to 1 ns time window with a mono-exponential decaying function, disregarding the oscillations and the rising part of the signal, to get τ_2. Secondly, for the 0-100 ps short-term traces, the points of artefacts (at time zero) which come from water solvent and quartz flow cell were removed, by referencing the cross-phase modulation signal of pure water solvent. The short-term traces were fitted with a mono-exponential decaying function (to obtain τ_1), with an addition of damped cosine function (to obtain τ_{osc} and τ_D) to account for modulations. In the end, a final optimization was performed by using the preliminarily obtained $\tau_1, \tau_2, \tau_{osc}$ and τ_D as references. The fitted traces are plotted in Figure 3, and the extracted parameters are given in Table 1.

The uncertainty on the time-zero position, due to the asymmetry and probe energy dependence of the cross-phase modulation signal and to the group velocity dispersion (GVD) correction, makes the absolute value of the phase of the oscillations difficult to retrieve. Therefore, we use a time zero offset c, and the offset could be different at different probe energies.

4.6.3 Visible probe studies

Figure S2a displays the colour-coded map of the visible TA as a function of probe photon energy and time delay between pump and probe. The transients at specific time delays are shown in Figure S2b. The signal around 2.25 eV has been removed because of the strong pump scattering. We observe a negative TA response in the centre (2.35 eV) and two positive wings on the blue and red sides, whose amplitude decreases dramatically during early time delays (~4 ps). There are two clear isosbestic points at ~2.5 and ~2.2 eV of the TA spectra suggesting that there is only one thermal contribution[54,65,189] to this transient response and that all of the features should have an identical temporal behaviour. This is indeed the case as can be seen from Figures S3 and S4, where we present the normalized spectral traces at different time delays (Figure S3) and the time traces of the Au NPs probed at 2.35 (spectra minimum), 2.60 (blue wing) and 2.10 eV (red wing). Figure S3 shows the normalised transients, showing that their profiles are unchanged in the 20 ps time window and that they evolve at the same rate. Figure S4a shows the experimental traces as measured, while Figure S4b shows them normalized, confirming that they have the same temporal evolution in the 20 ps window. The plasmon TA response rises within the cross-correlation of the experiment and decays within ~4 ps. Thereafter, the signal undergoes a slow relaxation. The inset of Figure S4b shows the temporal window from 5 to 400 ps for the 2.35 eV trace. A biexponential fit of the time traces in Figure S4 yields a fast component of 2.3±0.1 ps and a slow one 258±35 ps. Overall, the present results are consistent with previous studies[54,55,65,66,88,165,167] using visible probes after LSPR excitation (see Table S1) and they can be described as: (1) a pronounced initial, few-ps decay due to electron-electron and electron-phonon scattering; (2) a slower, 100s of ps decay due to cooling of the hot lattice to the environment.

Table S1: Time constants of the kinetics of optical excited Au films and nanoparticles from the literature using different measurements methods.

Sample	$E_{exc.}$ (eV)	E_{probe} (eV)	$F_{exc.}$	τ_{e-p} (ps)	$\tau_{cooling}$ (ps)	Method
Thin film, 20 nm[61]	2.0	2.34-2.82	2.5-200 μJ/cm^2	~1	-	Transient reflectivity & transmissivity
NPs, 30 nm[54,55]	2.1	1.72-2.75	0.1-0.2 mJ/pulse	2.5	>50	TA
NPs, 18.5 nm[76]	2.3	1.5	~40 μJ/cm^2	-	~80	TA
NPs, 11±2 nm[65]	3.1	1.78-2.48	<0.1 mJ/cm^2	0.8±0.1	~100	TA
NPs, 7.6±2.4 nm[165]	2.3	1.03-2.75	1.4 mJ/cm^2	2.8	120	TA
NPs, 26nm[69]	3.1	2.34	~300 μJ/cm^2	-	130±20	TA
NPs, 50 nm[69]					270±30	
NPs, 15 nm[70]	3.1	2.34	0.25 μJ/pulse	-	90±3	TA
NPs, 17 nm[179]	3.1	1.78	0.5 nJ/pulse	1.2	-	TA
		2.36	0.5 nJ/pulse	0.9		
		1.78	6.8 nJ/pulse	2.2		

		1.78	21 nJ/pulse	4.6		
NPs, 100 nm[85]	3.1	X-ray (15 keV)	~14 mJ/cm^2	-	~1 ns	X-ray scattering
NPs, 1.8 nm[171]	2.3	X-ray (11.92 keV)	110 mJ/cm^2	-	~1.8 ns	X-ray absorption spectroscopy

Table S2: Theoretical and experimental values for the transition energies of Au at the X and L points.

Transition	Assignment	Calc. from BS diagram[22]	ARPES data[24]	TA sign	Exp. TA bands
X_3-X_1		3.18			
X_4-X_1	d-sub band $\rightarrow$ 6sp	3.50		<0	3.8
X_4-E_F		2.99			
L_5-L_2	d-sub band $\rightarrow$ 6sp	3.50	3.95	>0	3.4-3.6
L_5-L_3		2.70	2.55		
L_5-L_4		2.16	1.75		
L_6- L_2		4.58	5		
L_3- E_F		2.23			
L_6-L_3	d sub-band $\rightarrow$ 5d band (only when the inter-band excitation is present)	3.88	3.8	>0	3.4-3.6
L_6 -L_4		3.24	3		
L_2-L_1	lower 6sp$\rightarrow$ upper 6sp	4.77	4.3	<0	4.4
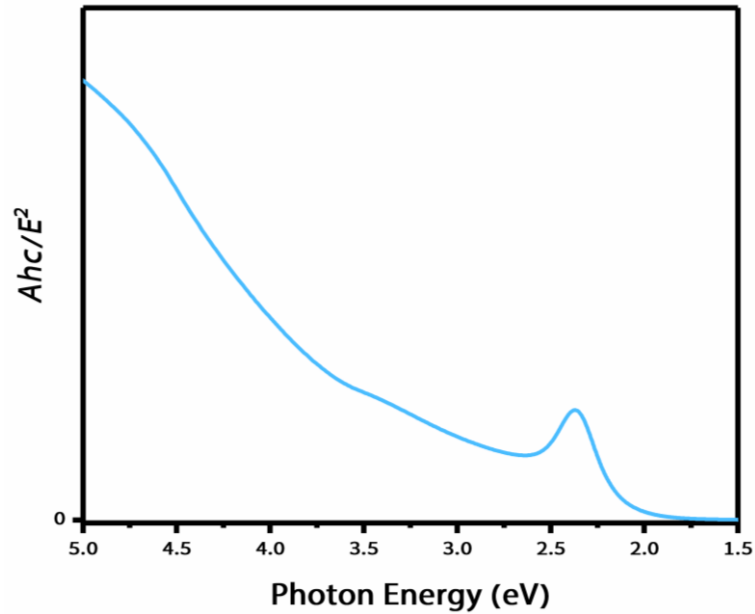
Figure S1: Steady-state absorption of the Au NPs. The measured NPs have a diameter of ~25 nm, and the sample was dispersed in water.
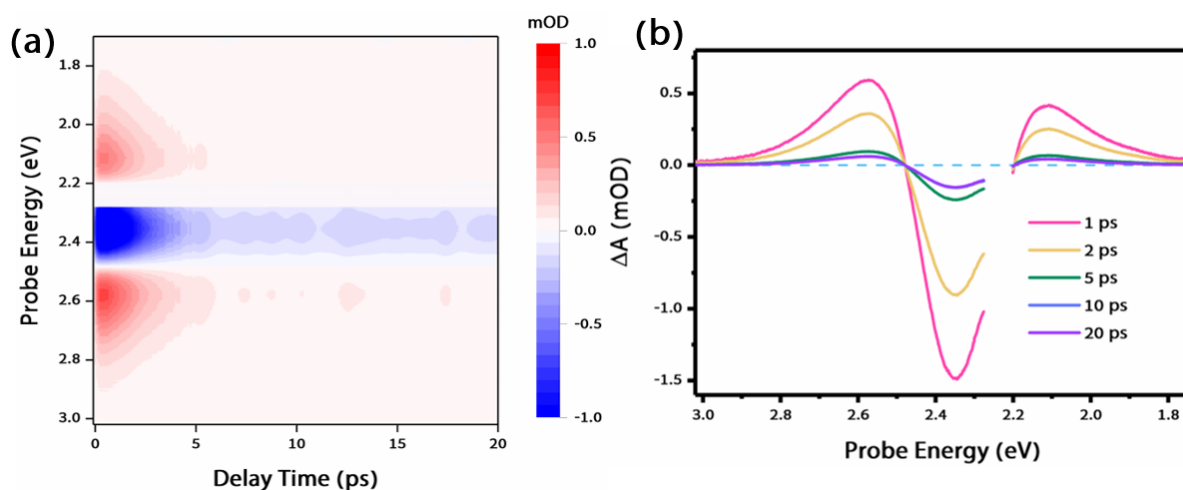
Figure S2: Time-energy TA map and the corresponding spectral traces probed in the visible. (a) Color-coded map of TA as a function of the probe energy and time delay between pump and probe. (b) TA spectra at selected delays of 1 ps, 2ps, 5 ps, 10 ps and 20 ps. Upon 2.25 eV plasmon excitation.
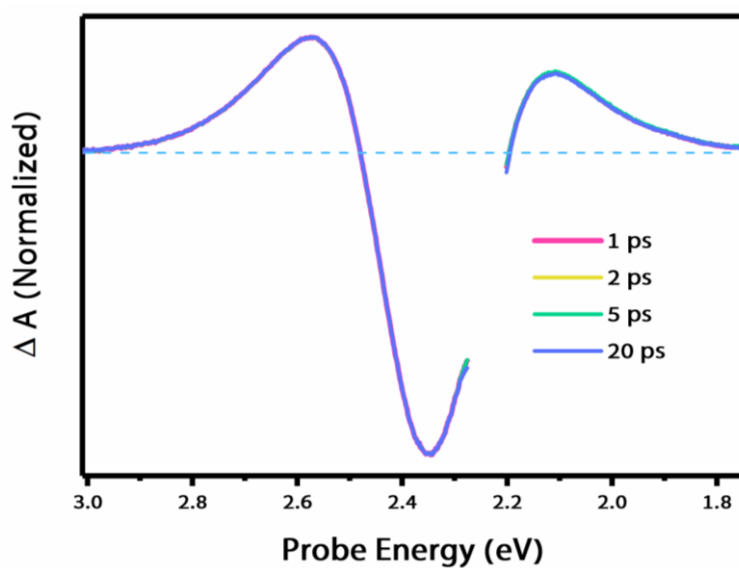
Figure S3: Normalized TA spectra of the Au NPs. At selected delays of 1 ps, 2 ps, 5 ps and 20 ps. Upon 2.25 eV plasmon excitation.
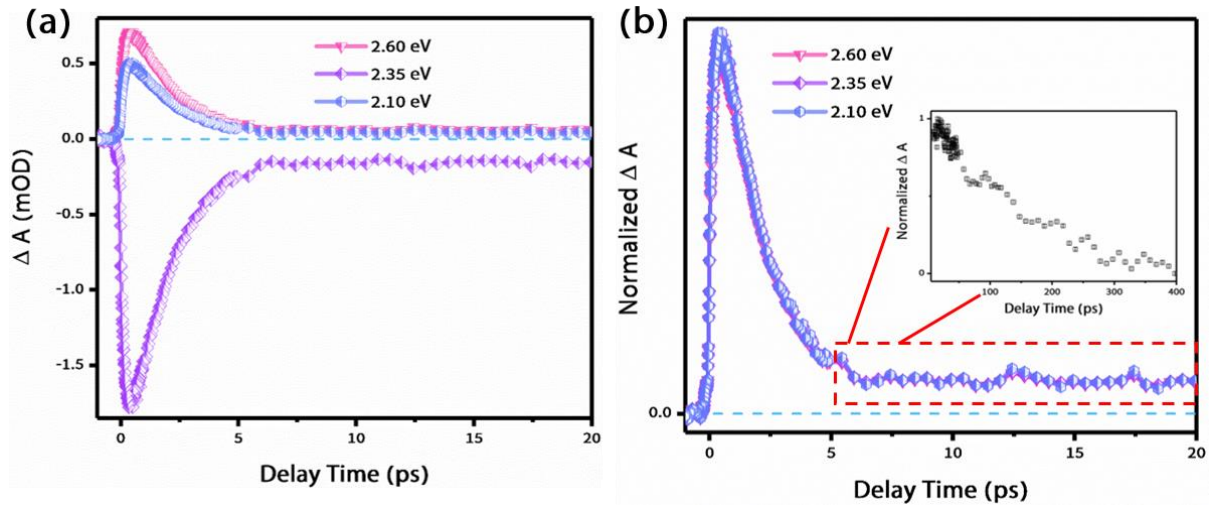
Figure S4: Time traces of the Au NPs upon vis-pump/vis-probe. (a) Time traces probed at 2.60, 2.35 and 2.10 eV. (b) Normalized time traces probed at 2.60, 2.35 and 2.10 eV. The inset in (b) zooms into the long-term temporal region of 5 to 400 ps of the trace at 2.35 eV.
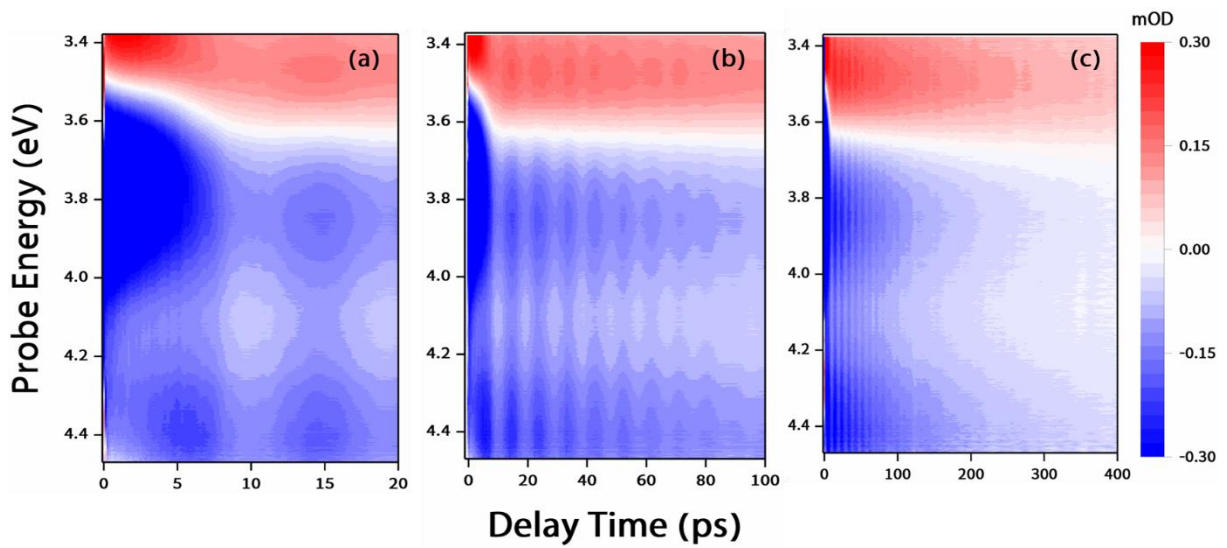
Figure S5: Time-energy TA maps upon vis-pump/near-to-deep-UV-probe. Within time delay of (a) 20, (b) 100 and (c) 400 ps.
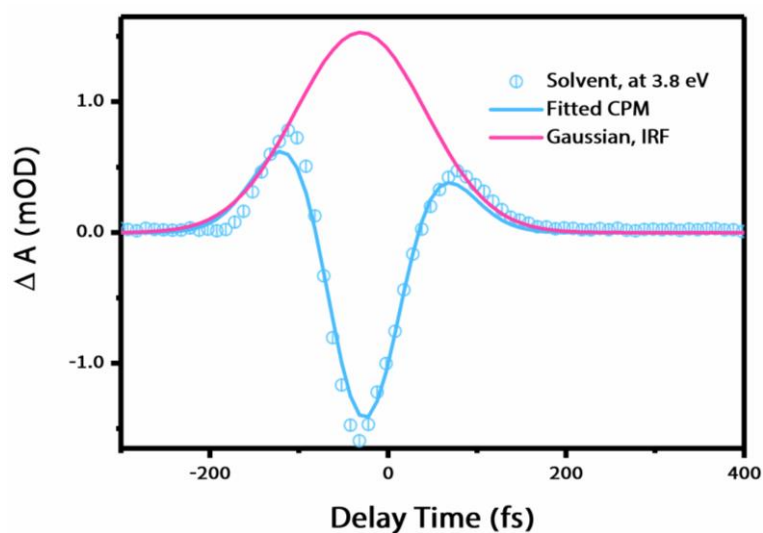
Figure S6: The pure solvent (water) cross phase modulation fit. The cyan circles represent experimental data, the cyan solid line is the fitted CPM curve, and the red solid line is the Gaussian peak, which has the same FWHM.
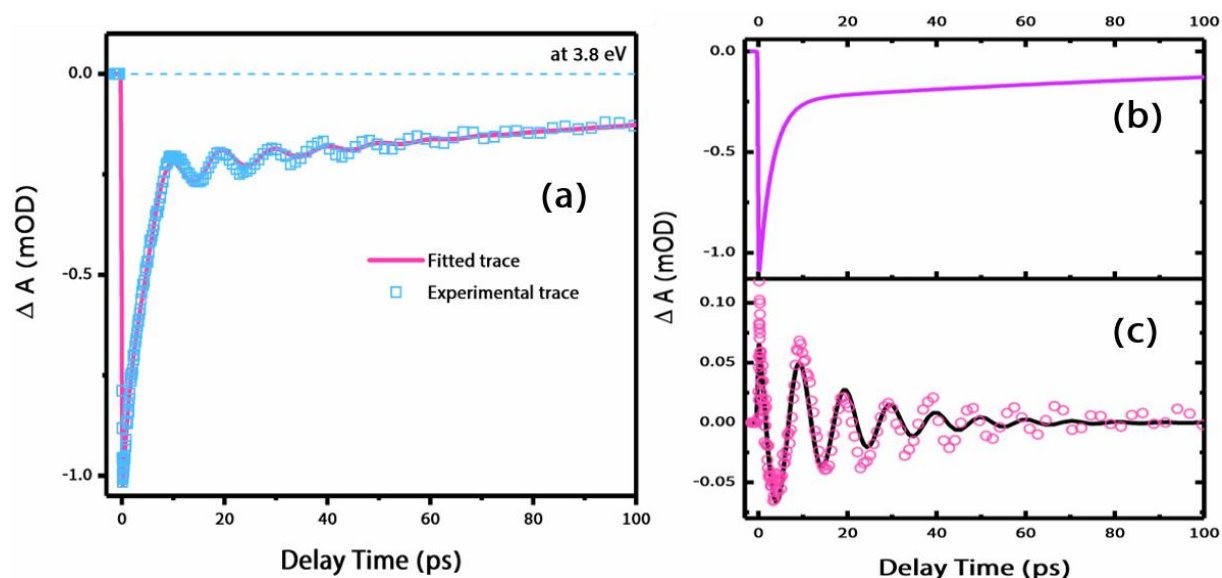
Figure S7: The fitting of the temporal trace probed at 3.8 eV. (a) The cyan squares are experimental data, the red solid line is the fitted time trace. (b, c) Decomposition of the time trace into kinetic and oscillation, as shown in b and c.
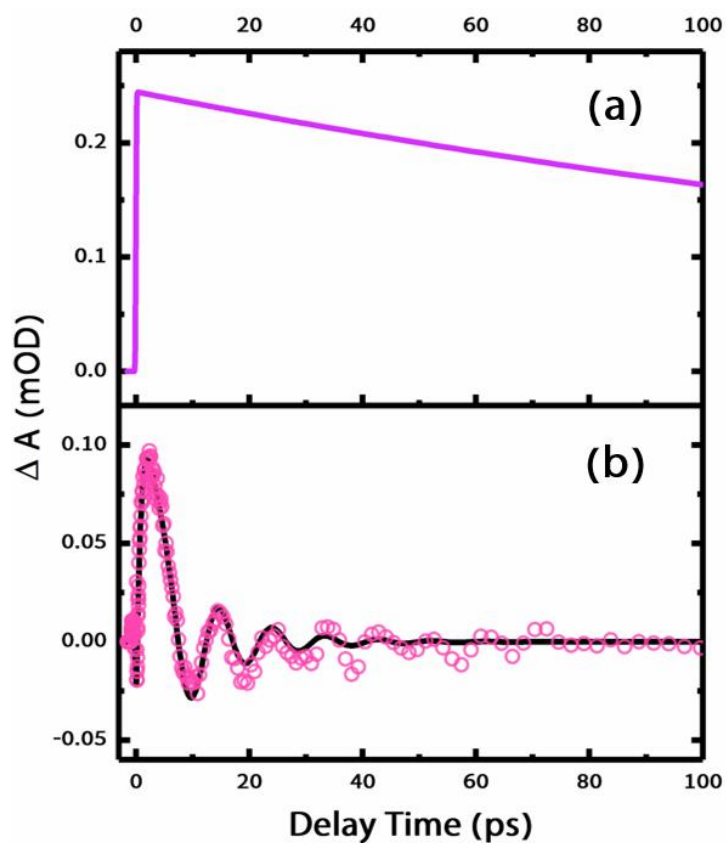
Figure S8 Decomposition of the time trace into kinetic and oscillation at 3.4 eV, as shown in a and b.
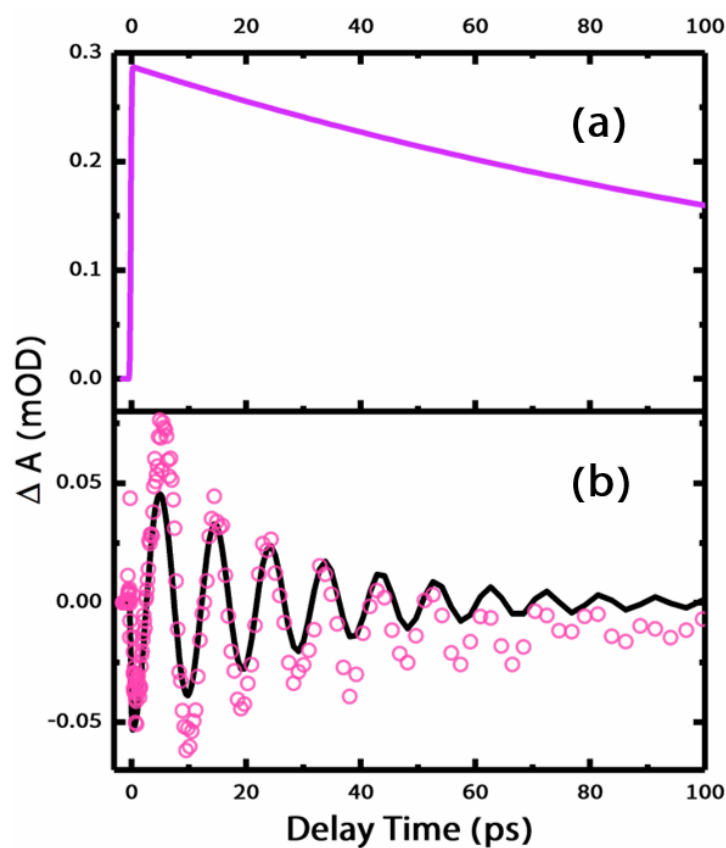
Figure S9 Decomposition of the time trace into kinetic and oscillation at 4.4 eV, as shown in a and b.

Chapter 5 Temperature effects on the absorption spectra of colloidal Au nanoparticles

5.1 Experimental temperature dependent absorption spectra

A T-dependent steady-state absorption study under dark conditions are performed (the methods are presented in Chapter 3), due to difficulties, in particular, aggregation at high temperature, in investigating colloidal bare Au NPs, we have used Au/SiO_2 core-shell NPs. The absorption spectra of bare Au and Au/SiO_2 are compared in Figure 5.1, they both exhibit the LSPR band at ~2.3 eV although the Au/SiO_2 shows a small (~0.3 eV) redshift due to the larger refractive index of the shell, while the growing featureless continuous background on the high energy side is due to interband absorption and to scattering. The absorption spectra of Au/SiO_2 measured between 30 and 80 °C are presented in Figure 5.2. The T-effect is overall weak, and is most visible in the region of the LSPR (Figure 5.2b) where it shows a downward trend in intensity and a slight broadening. The region around 3.5 eV also shows some variations.
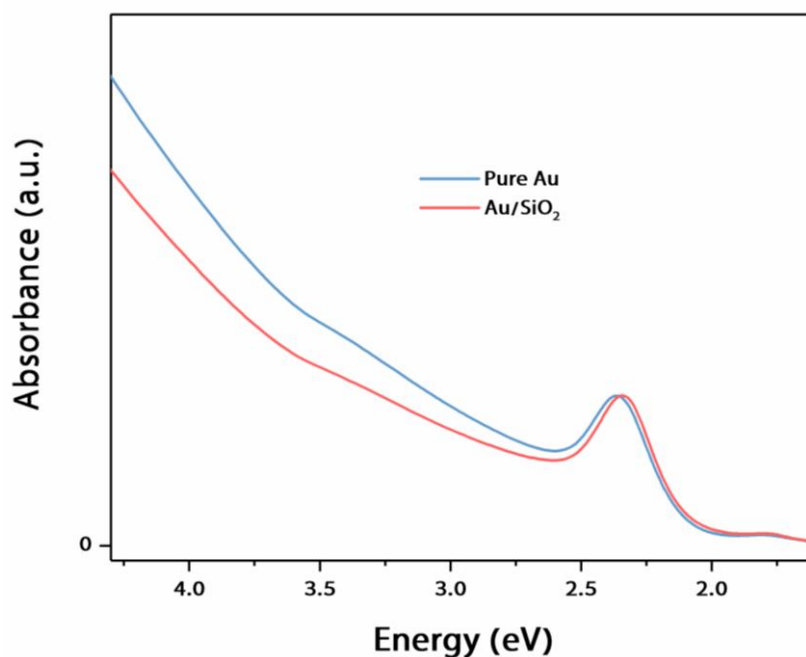
Figure 5.1 Absorption spectra of ~25 nm-diameter bare Au and core-shell Au/SiO_2 NPs, normalized at the maximum of the LSPR peak.
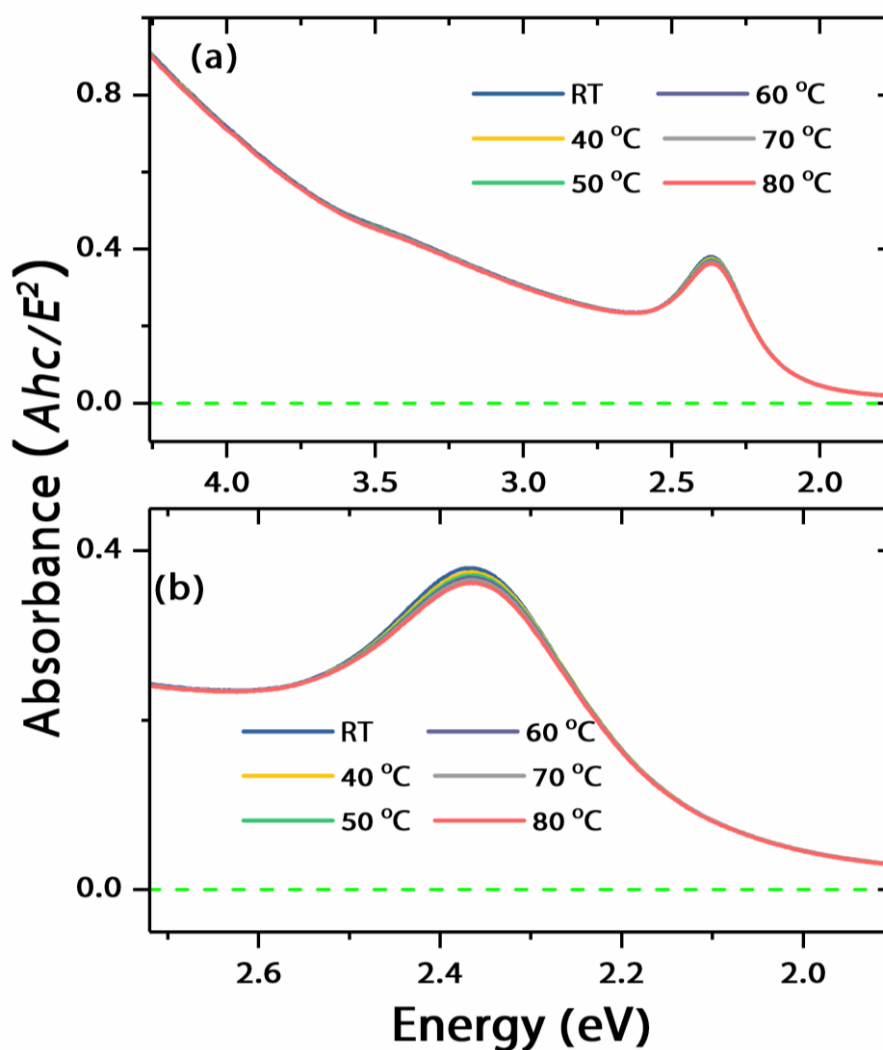
Figure 5.2 (a) Steady state absorption spectra of Au/SiO$_2$ NPs measured at temperatures ranging from RT to 80 °C; (b) zoom into the LSPR region.

The temperature-effect is best visualized by taking the difference of a spectrum at a higher temperature minus that at RT (~25 °C). These differential absorption spectra are displayed in Figure 5.3. They show an increasing drop in intensity at the LSPR with increasing T, as well as a decreased intensity over the entire UV region above 2.6 eV. Figure 5.4 zooms into the region of the LSPR and Figure 5.5 shows a selection of normalized spectra in the same region. One notes that the intensity drops of the LSPR band are multiplied by a factor of ~3 between 40 and 80 °C. The minimum of LSPR signal shifts slightly to lower energies with increasing T and a weak positive wing appears on the red of the LSPR, with the point of zero crossing shifting to lower energies with increasing T. Finally, no positive wing shows up on the high energy side of the LSPR band, and the overall trends are qualitatively similar to those reported by Bouillard et al[130] for nanorods. The region of interband transitions in Figure 5.3 is rather featureless except for a feature appearing at ~3.5 eV.
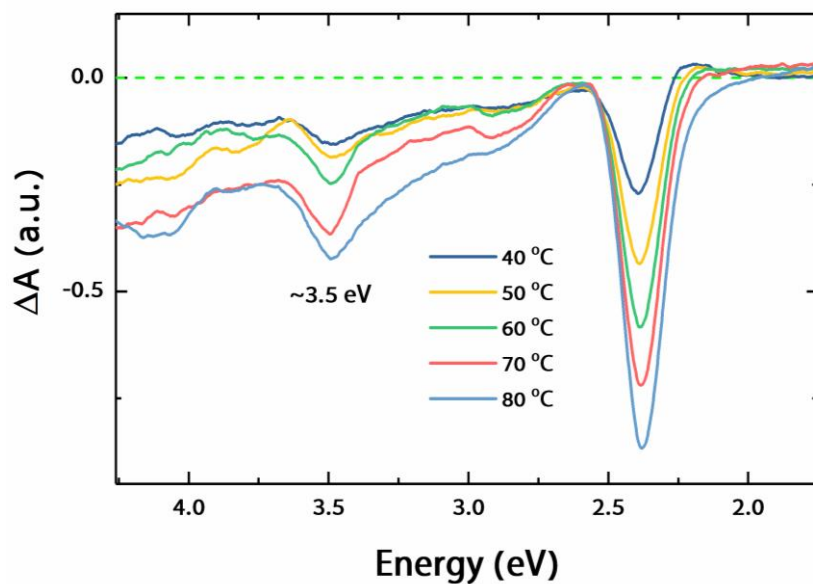
Figure 5.3 Absorption difference spectra of Au/SiO$_2$ NPs, obtained by taking the difference of a spectrum at high temperature minus that at RT (~20 °C).
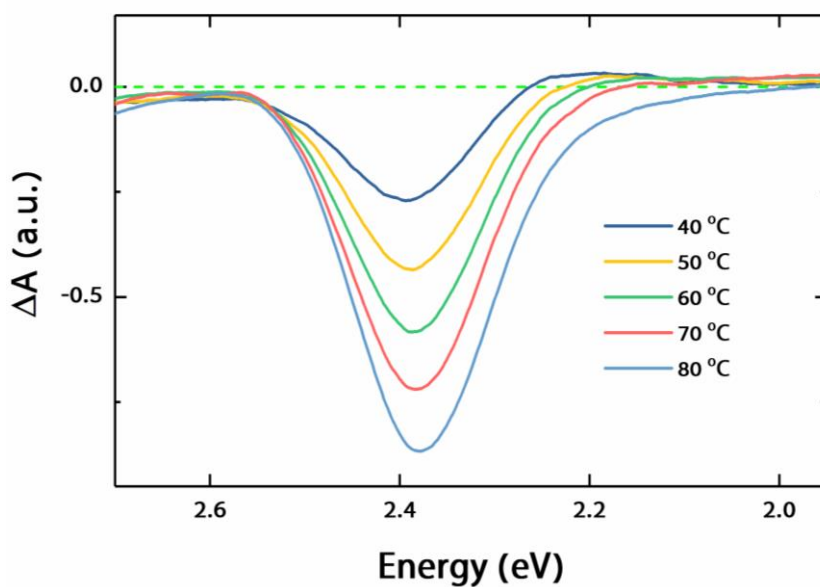
Figure 5.4 Zoom in the LSPR region of the absorption difference spectra of Au/SiO$_2$ NPs, obtained by taking the difference of a spectrum at high temperature minus that at RT.
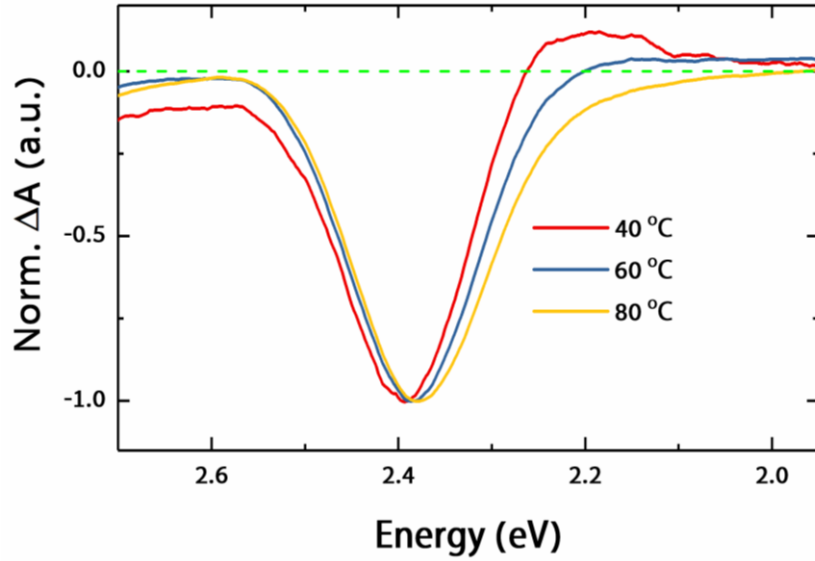
Figure 5.5 Normalized experimental absorption difference spectra of Au/SiO$_2$ NPs, obtained by taking the difference of a spectrum at high temperature minus that at RT.

5.2 Simulated temperature dependent absorption spectra

Since it has been shown that the temperature could affect the imaginary part of the dielectric of Au NPs, both in the interband transition and the LSPR regions. To evaluate to what extent the temperature affects the transients in the UV region, a calculation of the absorption spectra based on the dielectric properties of Au within a range of temperature were carried out, and combine with the experimental T-dependent absorption results, we should be able to have a clear cut knowledge of the light- and thermal- induced effects on the absorption spectroscopy in Au NPs.

Figure 2.7 (in Chapter 2) shows the of ε_1, ε_2 of Au NPs measured from RT up to 350 ºC for ~20 nm NPs[129]. The real part of the permittivity ε_1 shows minimal changes with increasing T, while the imaginary part ε_2 shows an overall increase with T, both in the regions of interband transition and the low energy part (Drude tail). Note that at the lower energy part, the changes are significantly more prominent at the red end than at the blue one. In the region of the interband transitions, the changes are only significant around 3.5 eV. The calculation of the absorption spectra, based on the equation 1.5 (see Chapter 1) makes the following approximations: a) we assume that the T-dependence of ~20 nm NPs[129] reflects that of the 25 nm NPs used here; b) although the ε_d of the surrounding medium is basically both wavelength- and T-dependent[126,190,191], the T-induced changes of ε_d of the surrounding medium are tiny in our temperature range and are thus assumed to play a negligible role on the overall Au absorption spectrum; c) as medium, we only consider water because the volume fraction occupied by the SiO$_2$ shell is negligible.
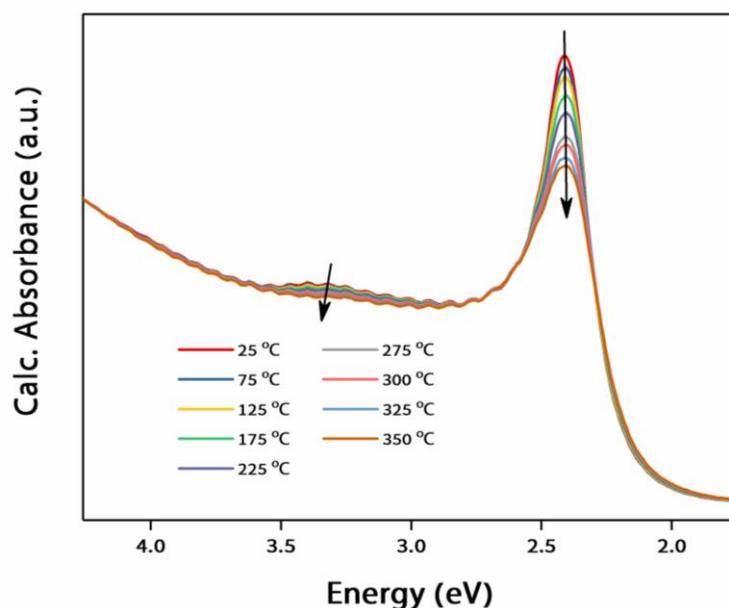
Figure 5.6 Simulated absorption spectra at temperatures varying from 25 to 350 °C, the calculations were based on the measured dielectric data of Au NPs shown in Figure 4.7.

Figure 5.6 shows the simulated steady-state absorption spectra, whose variations are exclusively due to the T-dependent dielectric functions. An overall decrease in intensity with increasing T is observed over the entire spectral range and is more pronounced at the LSPR maximum (at ~2.4 eV), and an additional feature appears at ~3.4 eV. The calculated differential spectra are shown in Figure 5.7 b and a zoom in the region of the LSPR is shown in Figure 5.8 b. Because, the lowest two temperatures reported by Magnozzi *et al* are 25 and 75 °C[129] as in Figure 2.7 (in Chapter 2) , the first differential spectrum is that at 75 °C, which is close to the highest temperature reached in our experiment. For this reason and those invoked above, we cannot carry out a quantitative comparison between experimental and calculated differential absorption spectra, but the main goal here is in reproducing the trends. Figure 5.9 b shows the normalised calculated differential spectra. From Figures 5.7, 5.8 and 5.9, one notes that the LSPR minimum is somewhat blue shifted compared to the experimental data, which is mainly due to the presence of SiO$_2$ shell which has a larger refractive index in the experimental case (also can be seen from Figure 5.1). In addition, a positive feature appears on the red of the LSPR band, as in the experiment, and the point of zero crossing on the red side of the LSPR shifts to the red with increasing T, which is in good agreement with Kruglyak et al[125] and Inouye et al's work[165]. On the blue side, and even though the experimental differential spectra do not show a positive wing, the calculations predict one, but much weaker than on the red side. This is a consequence of the T-induced changes of ε_2 in this range (Figure 2.7). We also note that the point of zero crossing of the blue wing shifts to higher energies with increasing T (Figure 5.9b). The absence of a blue wing in the experimental data is presumably due to the overall intensity decrease in the region above the LSPR band (Figure 5.7a). Finally, the calculated spectra predict a weak T-dependence of the interband absorption region of Au NPs, while the drop in

absorption is not negligible in the experimental differential spectra. This baseline drift is likely caused by T-induced increased scattering.
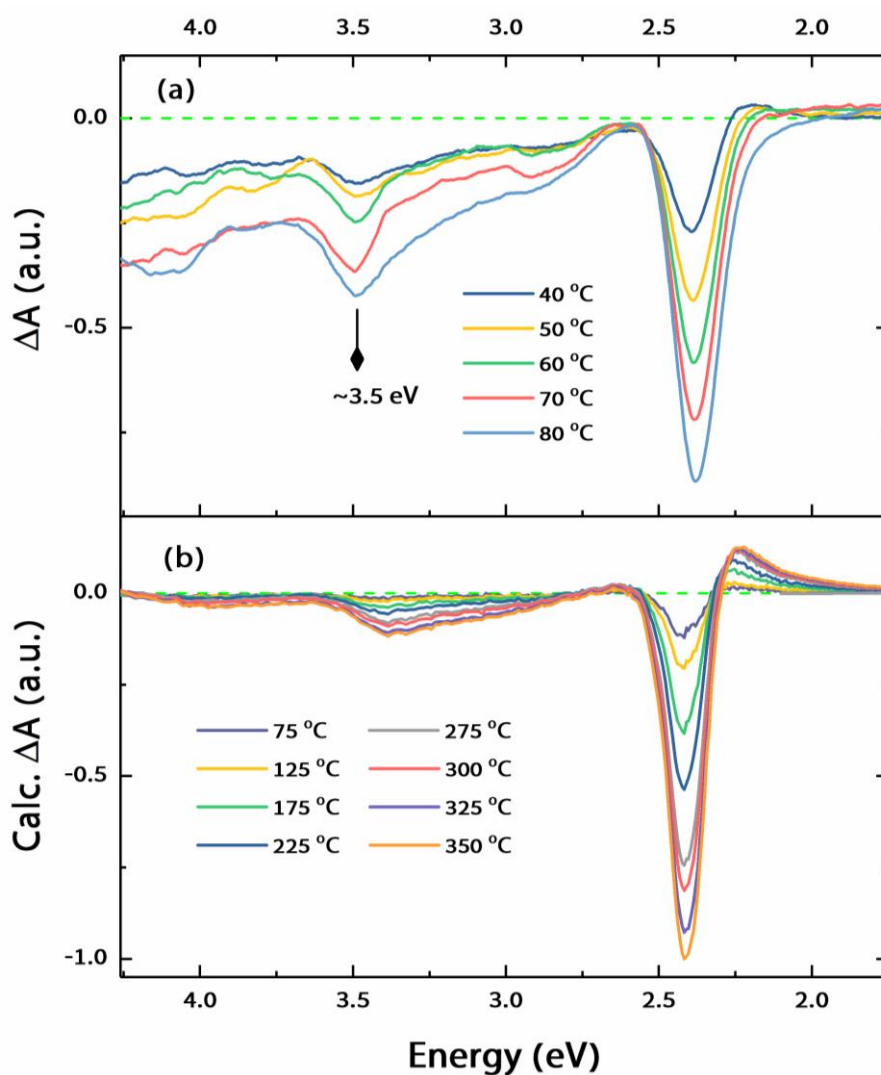
Figure 5.7 (a) Absorption difference spectra of Au/SiO$_2$ NPs, obtained by taking the difference of a spectrum at high temperature minus that at RT (~25 °C); (b) Calculated differential absorbance of Au NPs from the measured real (ε_1) and imaginary (ε_2) parts of ε_{Au} at temperature varying from 75 to 350 °C.
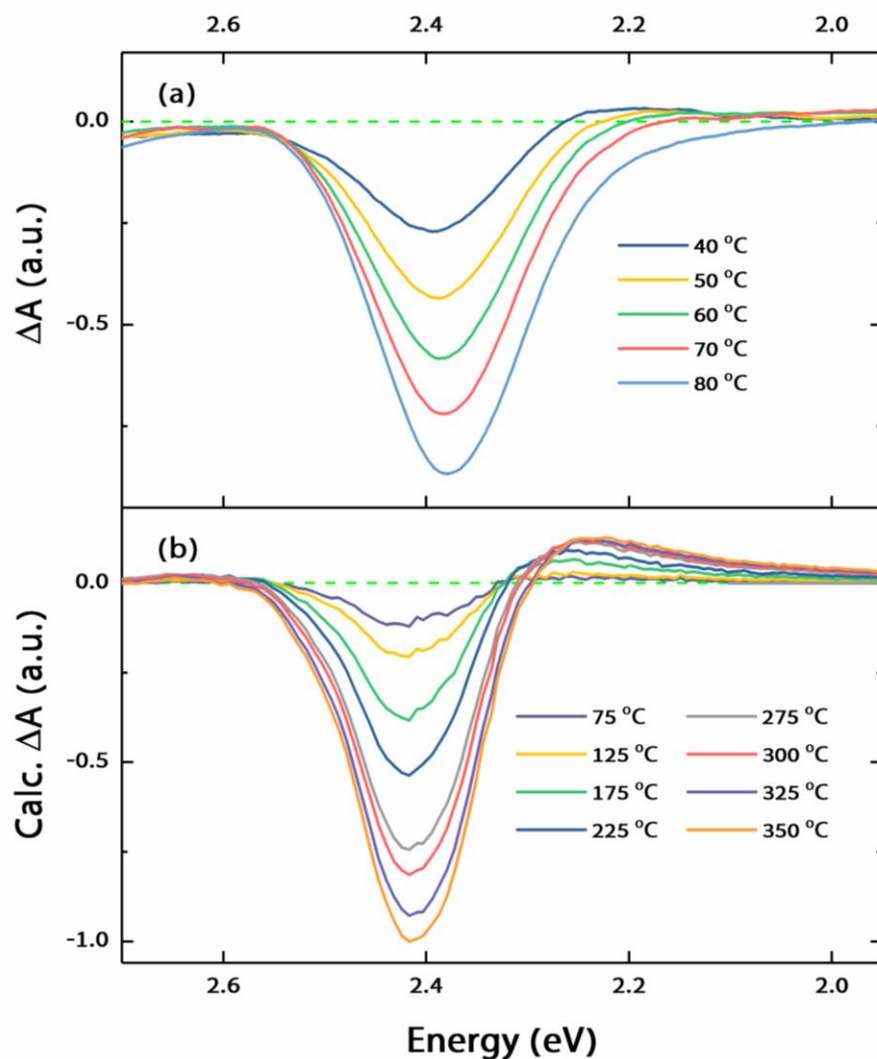
Figure 5.8 (a) Zoom in the LSPR region of the absorption difference spectra of Au/SiO_2 NPs, obtained by taking the difference of a spectrum at high temperature minus that at RT ($\sim$25 $^{\circ}$C); (b) Zoom in the LSPR region of the calculated differential absorbance of Au NPs from the measured real (ε_1) and imaginary (ε_2) parts of ε_{Au} at temperature varying from 75 to 350 $^{\circ}$C.
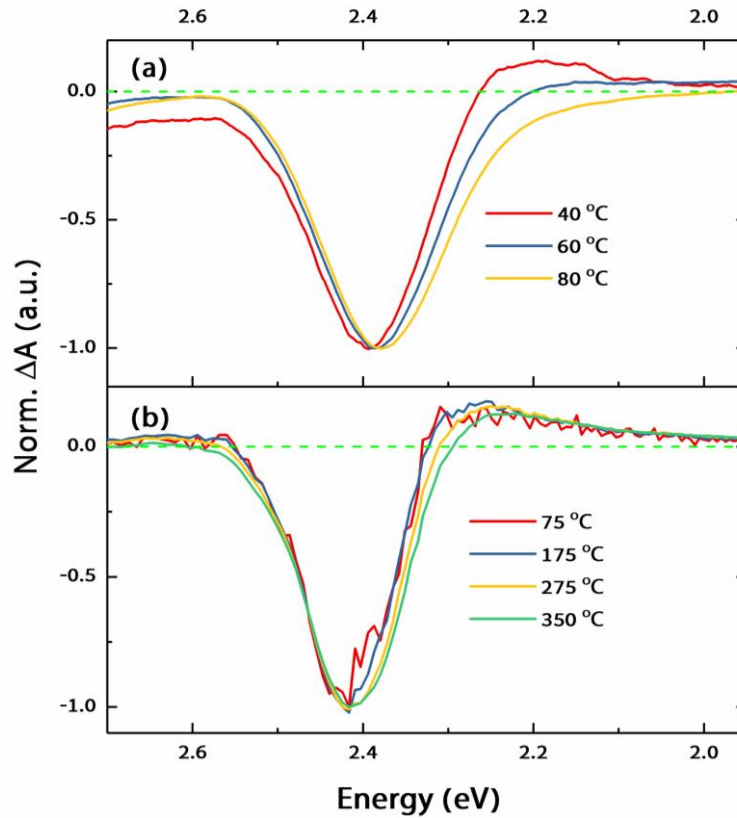
Figure 5.9 (a) Normalized experimental absorption difference spectra Au/SiO$_2$ NPs, obtained by taking the difference of a spectrum at high temperature (40, 60 and 80 °C) minus that at RT (~25 °C); (b) Normalized calculated differential absorbance of Au NPs from the measured real (ε_1) and imaginary (ε_2) parts of ε_{Au} at temperature 75, 175, 275 and 350 °C.

Besides, the origin of the blue and red wings of the LSPR differential spectra is an important point that needs to be clarified in relation to photoinduced effects, which we will discuss below. Interestingly, in Yeshchenko *et al*'s work[126] on Au NPs in embedded in SiO$_2$, the intensity drop of the LSPR is accompanied by an intensity increase of both its red and blue wings, but the latter is more prominent. Unfortunately, these authors did not present differential spectra, which would have been preferable for comparing the trends with our data. Nevertheless, in Figure 5.10 we present our simulations of the LSPR differential spectra in water, SiO$_2$ and TiO$_2$. The enlarged LSPR region is presented in Figure 5.11. First of all, in all cases, the UV part has little spectral signatures, which is different with the photo-induced TA response described in Chapter 4. Secondly, contrary to the case of water, in SiO$_2$ a blue wing clearly shows up, almost comparable in intensity to the red one. In addition, the point of zero crossing moves to higher energies with increasing temperature just as for the red wing it moves to lower energies. These trends are in qualitative agreement with the results of ref.[126]. Furthermore, in TiO$_2$, the differential absorption signal gets remarkably enhanced, and the blue wing is even 5 times higher than the red one.

Which all suggest that the blue wing is strongly determined by the properties of the surrounding medium and not just that of the NP (Figure 5.12).
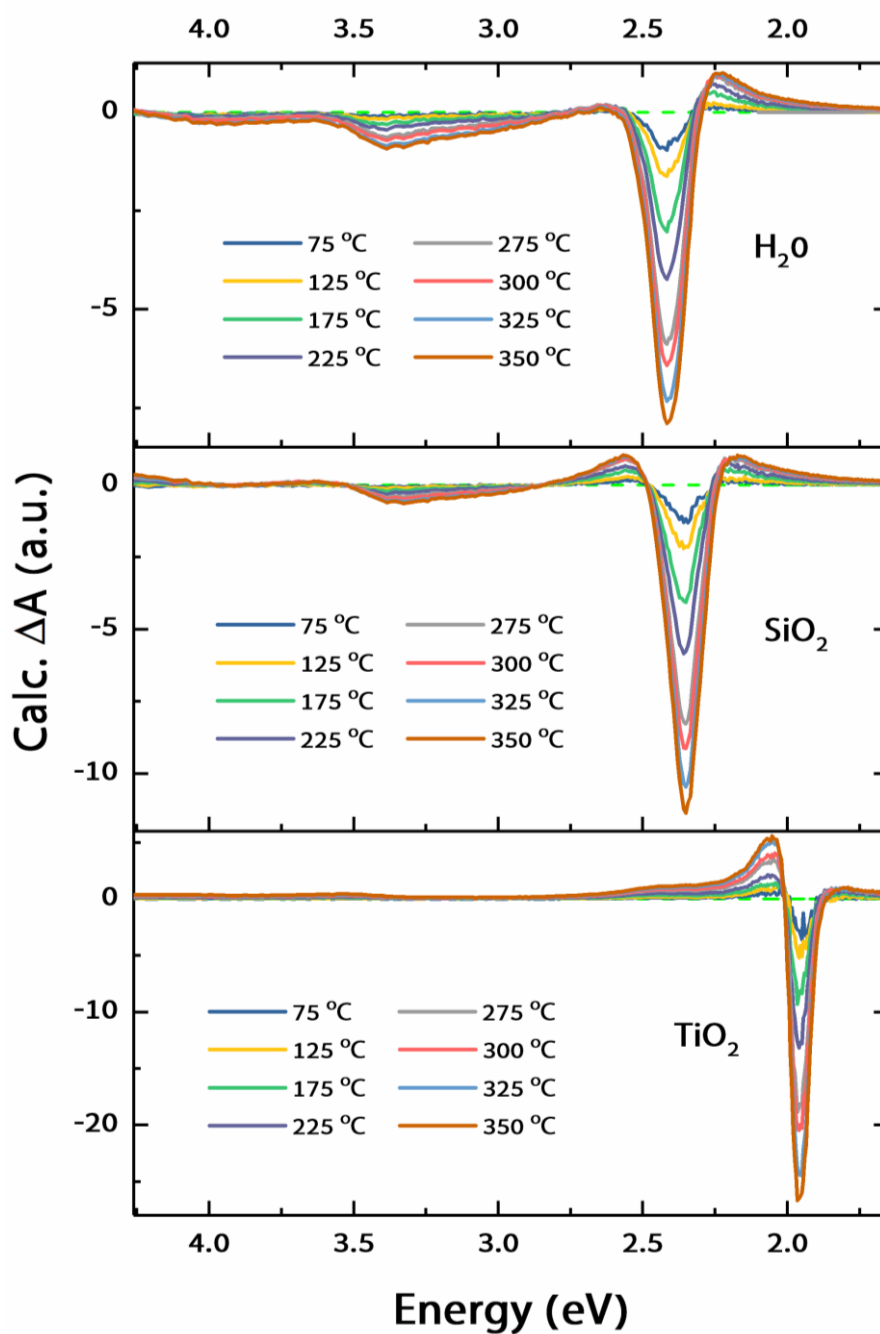
Figure 5.10 Calculated differential absorbance of Au NPs from the measured real (ε_1) and imaginary (ε_2) parts of ε_{Au}, while with different surrounding medium: (a) pure water; (b) SiO_2; (c) TiO_2. The maximum of the red wing of at the highest temperature of these three cases are normalized to 1.
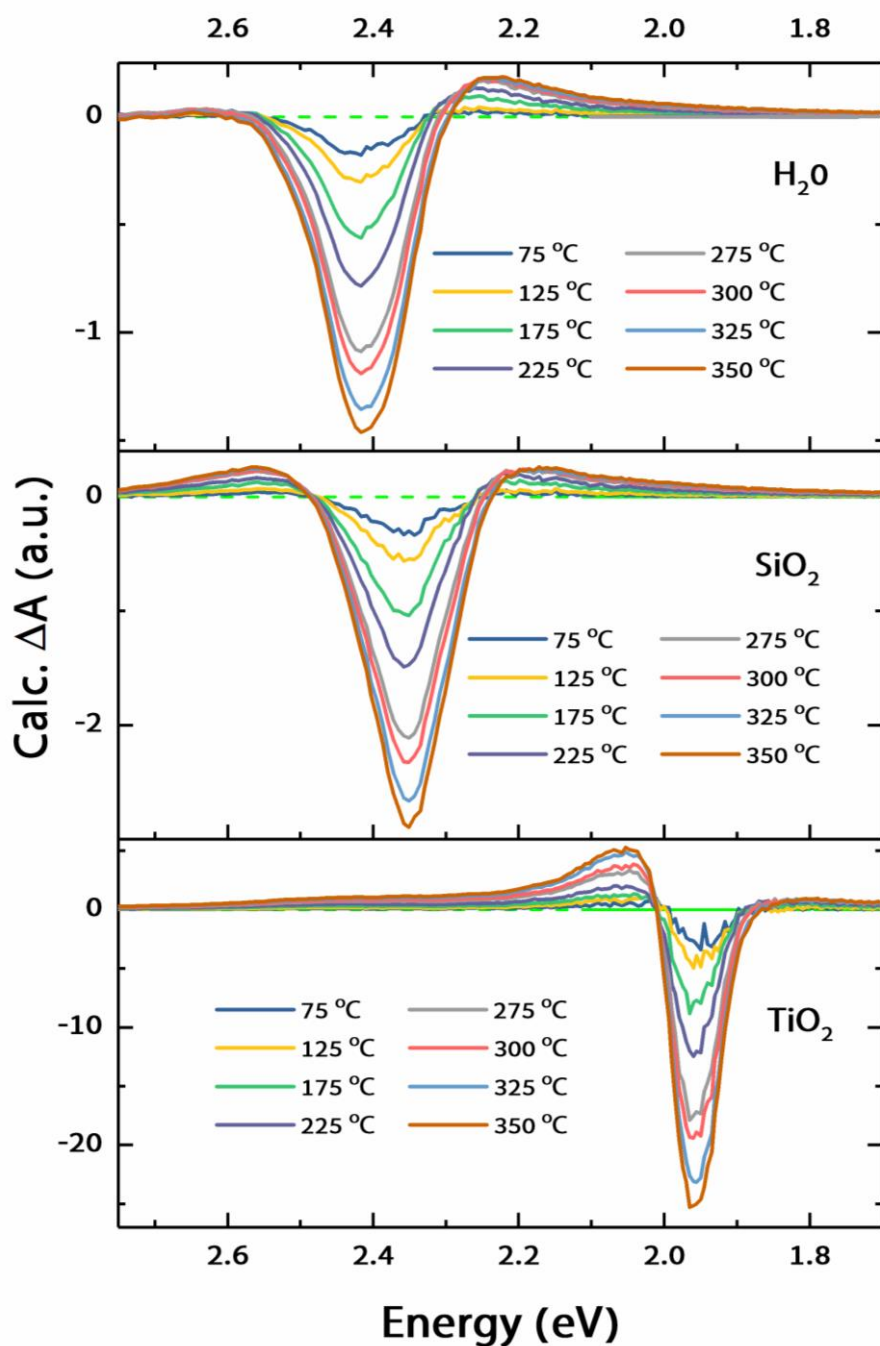
Figure 5.11 Zoom in Calculated differential absorbance of Au NPs from the measured real (ε_1) and imaginary (ε_2) parts of ε_{Au}, while with different surrounding medium: (a) pure water; (b) SiO_2; (c) TiO_2. The maximum of the red wing of at the highest temperature of these three cases are normalized to 1.
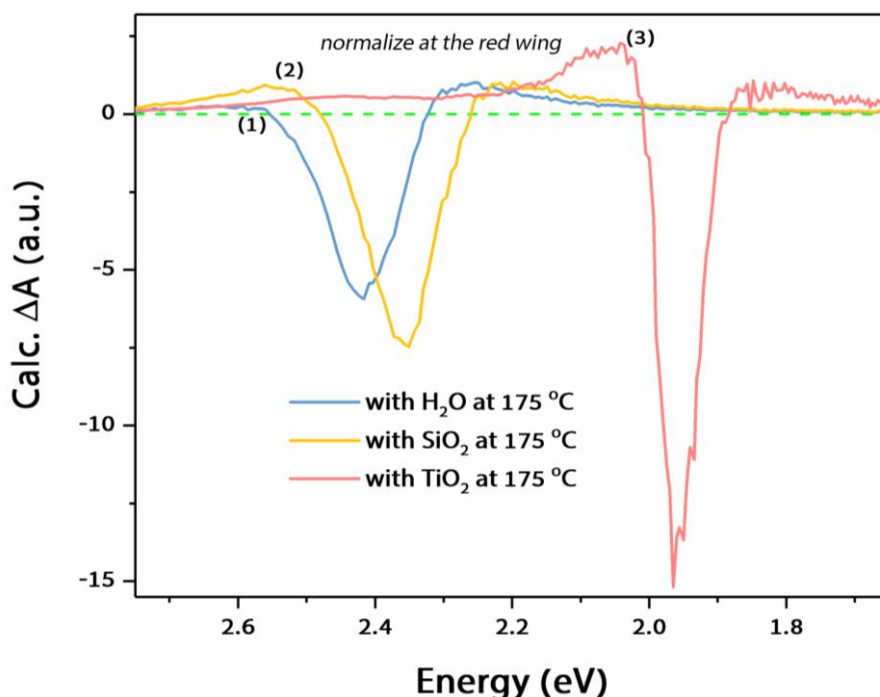
Figure 5.12 Comparison (LSPR region) of the calculated differential absorption of Au NPs with sounding medium of H_2O, SiO_2 and TiO_2 at 175 °C. The three spectra are normalized at the maximum of the positive red wing of the transient LSPR.

5.3 Comparison with the photo-induced transient response

TA spectra in the region of the LSPR band have been reported for Au NPs in silica glass[57] and in water[58,59,118], and for bulk Au films[125]. They all exhibit a bleach of the LSPR with the appearance of positive red and blue wings. However, while the point of zero crossing on the red wing shifts towards high energies with time (i.e. with cooling), in agreement with the calculations in Figures 5.6 and 5.7, the point of zero crossing on the blue side is isosbestic and does not reflect the trends shown in Figure 5.11. Furthermore, while the T-dependent experimental differential spectra lack the blue wing, as confirmed by the simulations (Figure 5.8), the photoinduced TA spectra for Au NPs in water do exhibit a clear one[58,59,128]. This suggests that the positive signal on the blue side of the LSPR band in TA spectra is an indicative of a broadening of the LSPR upon photoexcitation. The same behaviour is observed for Au NPs in SiO_2[57]. The main difference between the present T-induced measurements (under thermodynamic equilibrium) and photoinduced ones lies in the fact that in the latter case, electrons are excited above the E_F.

For the region of the interband transitions. In Chapter 4, we presented the TA spectra between 3.4 and 4.5 eV upon excitation of the LSPR. The comparison of the differential absorption spectrum of Au/SiO_2, TA spectrum at 10 ps, and calculations on the Au NPs absorption in the UV spectral region are shown

in Figure 5.13. Contrary to the differential T-induced spectra which are generally featureless, the photoinduced TA spectrum exhibits prominent negative features at ~3.8 eV and ~4.4 eV and a positive one at ~3.5 eV, which has already been described in Chapter 4. In addition, the T-induced change of absorption amplitude in the LSPR is significantly larger than that of interband region (Figure 5.7) suggesting that thermal effects on interband transitions are minimal, as actually supported by the calculations (Figure 5.7b).
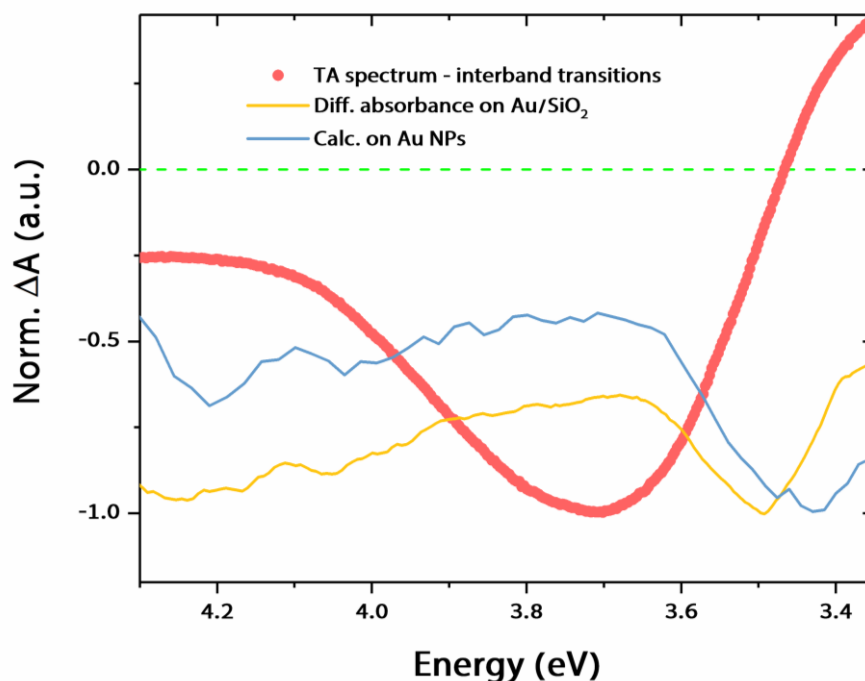
Figure 5.13 Comparison (interband transition region) of the differential absorption spectrum of Au/SiO$_2$, TA spectrum at 10 ps, and calculation on Au NPs, in the UV spectral region.

The (so-called linear) assumption that the transient signal depends linearly on either the transient electron (and lattice temperature)[192,193], the transient excess total electron energy[194], or the transient electron occupation number[195], was demonstrated to fail in the case of the plasmon resonance response of photoexcited thin Au films[125], and the above model was successfully used to rationalize the observations. In our deep-UV TA study (see Chapter 4), we used the linear assumption to interpret the response at the above three interband transitions[118]. The comparison of our TA spectrum with the T-dependent absorption differential spectra shows clearly that this assumption is valid for the region of the interband transitions. Furthermore, the good agreement between experimental and calculated T-induced differential spectra (Figures 5.7 and 5.8) further supports the conclusion that the TA spectra in the photoinduced case can by no means be rationalised in terms of pure heating. Therefore, while the LSPR response does reflect a modification of the dielectric properties due to photo-induced thermal effects, the response in the region of the interband transitions is wholly different and is little affected by thermal

effects, but rather by electronic ones. The reason between these two behaviours stems from the fact that while the LSPR is a collective oscillation of electrons determined by the size/shape of the NP, the interband region contains transitions between actual bands and sub-bands of the band structure diagram and they do monitor the evolution of charge carrier populations, while changes of the dielectric function of Au NPs upon heating are negligible in this region (Figure 5.7).

Furthermore, we also consider the effects of surrounding medium in the UV spectral region, and a calculation in full spectral region from the visible to UV is shown in Figure 5.14. Clearly, the thermal effects are only prominent in the LSPR region, the sounding medium indeed make an influence on the spectral intensity, LSPR frequency, the amplitude of the positive wings etc. as mentioned before, but it barely can affect the interband transitions in Au NPs.
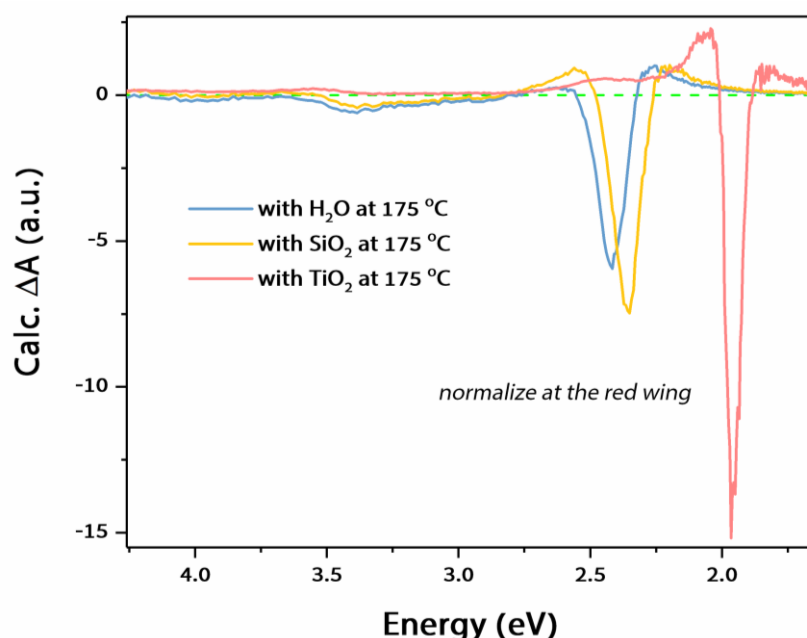
Figure 5.14 Comparison of the calculated differential absorption of Au NPs with surrounding medium of H_2O, SiO_2 and TiO_2 at 175 °C. The three spectra are normalized at the maximum of the positive red wing of the transient LSPR.

5.4 Temperature-dependent absorption on bare TiO_2

We also performed a T-dependent experiment on bare anatase TiO_2 NPs with 50 nm diameter, to investigate if the temperature increase could affect the anatase TiO_2 excitonic transition.

Because colloidal anatase TiO_2 NPs have a strong scattering background, and it has no absorption in the visible region, thus the measured intensity in the visible region is completely due to scattering, since the scattering has a relationship with wavelength: $\sim \lambda^{-4}$ (the shorter the wavelength, the stronger the scattering), we fit the scattering by using a 4th order polyfit function (only fit 450-700 nm region, because

this region is purely due to scattering), the measured spectra with and without scattering are shown in Figure 5.15. As can be seen, the scattering at > 380 nm is well reproduced and removed by subtraction, hence the absorption of bare anatase TiO_2 are displayed in the lower panel of the same figure. In Figure 5.16, we convert the wavelength into energy by using Jacobian methods (see Chapter 3), thus the well-known absorption-edge at ~3.8 eV is exhibited. As temperature increasing from RT (25 °C) to 80 °C, the absorption intensity in the UV has an overall drift while the visible part remains zero. Figure 5.17 shows the absorption difference spectra of bare anatase TiO_2 NPs, after subtracting the scattering background, there is a dramatically spectral drop in the UV region starting from ~3.6 eV and two negative features showing up at approximately at 3.8 and 4.2 eV, which correspond to the first and second excitonic transition in anatase TiO_2[39]. Some positive features show up, especially at low temperature, could be due to the noise of the instrument, or the quality of background fitting.

The reason for the appearance of such bleach at the excitonic transitions could be due to that the temperature changes the exciton binding energy in TiO_2 and modifies the optical absorption/reflectivity of it. Although the exact mechanism is unknown, the T-dependence of the TiO_2 shows that the lattice heating of TiO_2 could generate an absorption change at the exciton resonance, which may lead to a contribution in TA measurements
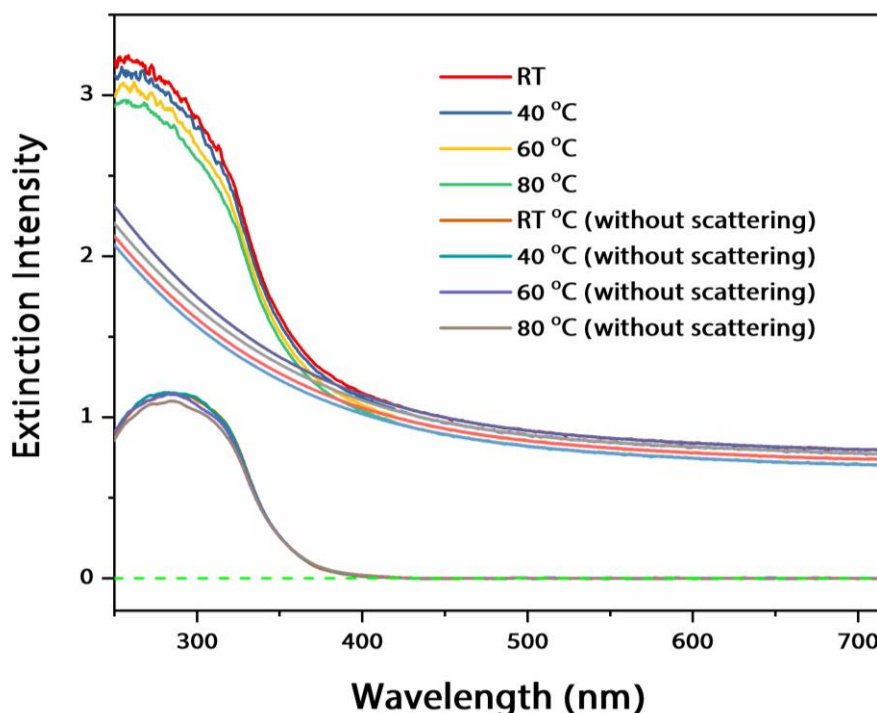
Figure 5.15 The extinction spectra of ~50 nm anatase TiO_2 NPs dispersed in aqueous solution, measured by UV-Vis absorption spectrometer, with different temperatures. The lower panel shows the absorption spectra of bare TiO_2 after removing the scattering background by subtraction.
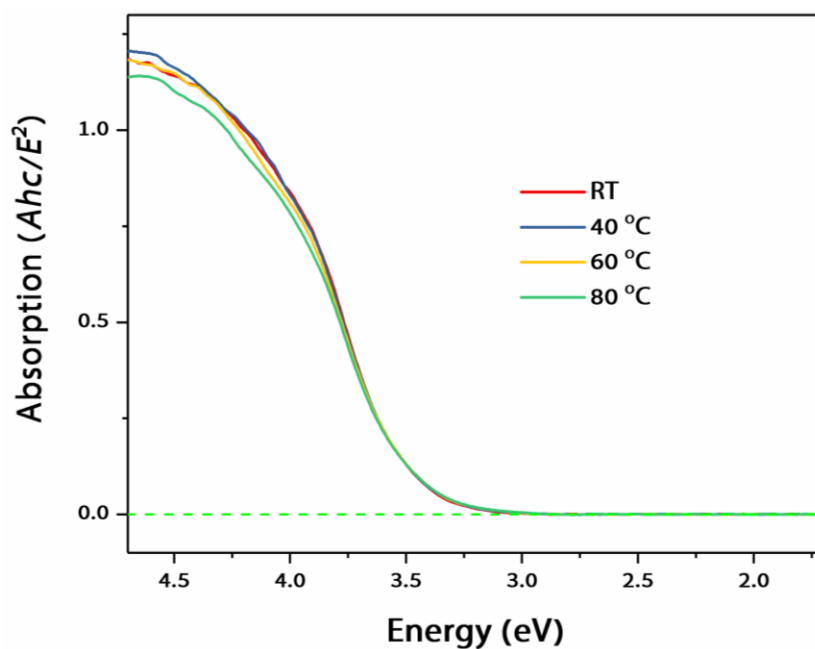
Figure 5.16 The absorption spectra of bare anatase TiO_2 NPs dispersed in aqueous solution, with different temperatures. The spectra were obtained by converting the wavelength into energy from Figure 5.12.
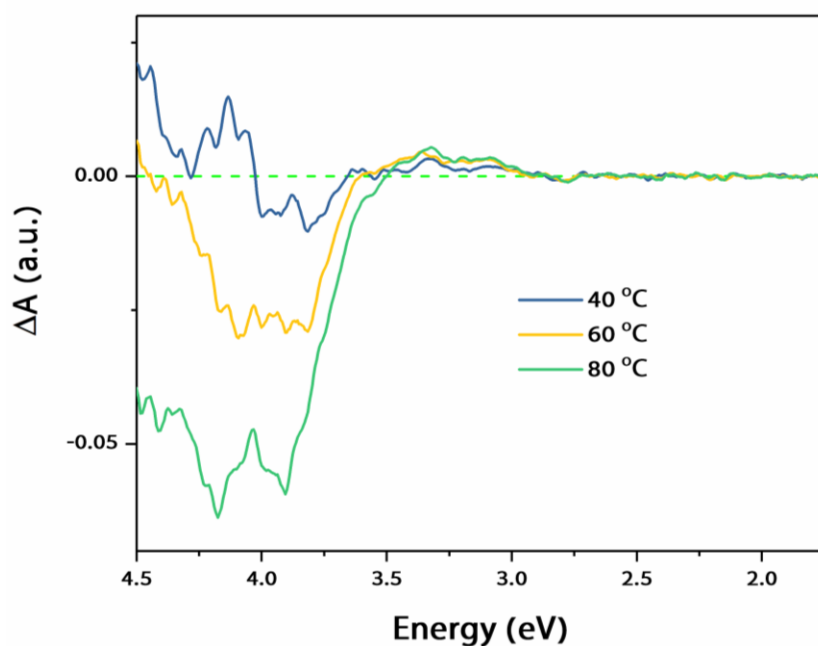
Figure 5.17 Absorption difference spectra of bare anatase TiO_2 NPs, obtained by taking the difference of a spectrum at high temperature minus that at RT (~25 °C), the absorption spectra used here are from Figure 5.13 (scattering background are removed).

In summary, in this Chapter, a temperature-dependence (from RT to 80 °C) investigation of the absorption spectrum of Au/SiO_2 core-shell NPs in the range from the visible (where the LSPR band lies) to the deep-UV (where the interband transitions are found) was presented. A decrease in absorption with temperature over the entire spectral range is observed that is significantly more prominent in the region of the LSPR than that of the interband transitions. These changes are well reproduced by theoretical calculations of the absorption spectra, based on the experimentally measured temperature-dependence of the real (ε_1) and imaginary part (ε_2) of the Au NP dielectric. Comparing the T-induced experimental and simulated absorption spectra, as well as those from the literature, and photoinduced TA spectra, suggests that the red wing of the LSPR band is sensitive to changes of the dielectric function of the NP reflecting a lattice heating. On the other hand the blue wing is also sensitive to the surrounding medium. Finally, in the interband region, the strong deviation of the differential spectra with the TA suggests that the latter is dominated by the response of the charge carriers, confirming the interpretation given in Chapter 4, and therefore the probing of actual charge carrier relaxation.

Chapter 6 Plasmon-mediated two-photon absorption in Au/TiO$_2$ nanoparticles

6.1 Transient response of Au/TiO$_2$ probed in the UV

6.1.1 Spectral features of Au/TiO$_2$

The steady-state absorption spectra of anatase TiO$_2$, Au/SiO$_2$ and Au/TiO$_2$ NPs have been previously shown in Figure 3.9. Figure 6.1 shows the time-energy deep-UV TA maps and corresponding TA spectra at different time delays of the three samples: bare anatase TiO$_2$ NPs excited above the BG excitation at 4.0 eV, Au/SiO$_2$ and Au/TiO$_2$ core-shell NPs excited into the LSPR band at 2.0-2.4 eV. The TA of bare anatase TiO$_2$ NPs (Figure 6.1a) is identical to what was reported in refs [39,196]. At 1, 100 and 800 ps time delays, the TA clearly exhibit a negative (bleach) signal over the entire probe range with a band centred at ~3.83 eV, which is due to the first excitonic transition of anatase TiO$_2$[39]. The bleach signal is due to electrons generated by BG excitation into the CB of TiO$_2$. Figure 6.1c shows the TA map for Au/SiO$_2$ NPs excited with a broadband pulse (2-2.4 eV) at the LSPR and Figure 6.1d shows the TA spectra. The TA maps and spectra for Au/SiO$_2$ NPs exhibit three main features: two negative ones at ~3.83 eV and ~4.4 eV, and a positive one at ~3.5 eV. These features have been discussed in detail in ref.[197]. Briefly, they were interpreted using the band structure diagram of bulk Au, as inter-band transitions from the 5d valence band to the 6sp band above the E$_F$ at the X and L symmetry points for the two negative ones, monitoring the population of electrons and holes, above and below the E$_F$, respectively. The positive band was identified as a transition between valence bands (i.e. an intraband transition), monitoring the population of holes. The overall conclusion was that charge carrier cooling is slow (~150 ps) and commensurate with the time scale for thermal lattice cooling (~250 ps).

Figure 6.1e and f show the TA maps and spectra for the Au/TiO$_2$ NPs, and Figure 6.2 shows the zoom of the TA map within 100 ps. Because of the red shift of the LSPR in TiO$_2$ compared to SiO$_2$ (Figure 3.9, see Chapter 3), the 2-2.4 eV broadband excitation only covers half the LSPR band, when comparing the TA response of these two, a calibration of the actual excitation intensity need to be performed. The used broadband pump pulse covers the 2.0-2.4 eV energy region, thus we calculate the area below the absorption curve with respect to the background baseline in this region, and obtain a ratio of ~1.3 of Au/SiO$_2$: Au/TiO$_2$ of the absorption. Therefore, when plotting the TA results of the Au/SiO$_2$ and Au/TiO$_2$, a factor of 1.3 was multiplied in the case of Au/TiO$_2$. Compared to Figures 6.1c and d, some notable differences, but also some similarities arise: a) The ~3.4 eV positive signal is shorter-lived in Au/TiO$_2$; b) there are obvious oscillations showing up in both Au/SiO$_2$ and Au/TiO$_2$ NPs, but with different frequencies; c) an intensive band shows up centred at ~3.8 eV but dramatically decreased within ~10 ps (Figure 6.2), and it slightly blue shifts by ~0.05 eV after ~10 ps and lasts up to the longest times of our temporal window. In Figure 5.3, we compare the 800 ps transients for the three samples.

For the Au/SiO$_2$ sample, the signal has died away except for the positive feature > 3.6 eV. However, the signal is non-zero for bare anatase TiO$_2$ and Au/TiO$_2$ NPs, which exhibit the same minimum at 3.8-3.82 eV. Given that the equivalent band in the Au core has vanished, we conclude that this bleach is due to electrons in the CB of the TiO$_2$ shell in Au/TiO$_2$ NPs; c) finally, the features >4.1 eV in Au/SiO$_2$ do not show up in the case of Au/TiO$_2$, due to the fact that the Au contribution to the transient is shaded by the strong absorption of TiO$_2$ in this region. The main point here is that the occurrence of the long-lived bleach band at the position (~3.8 eV) of the first excitonic transition of TiO$_2$ is a clear indication that Pauli blocking occurs due to an excess of electrons in the CB, as demonstrated in ref. [89,196]. However, the presence of the intraband transition of Au at ~3.4 eV is also indicative of holes in the Au NP core, due to electrons have been removed from it, as expected in the scenario of plasmon mediated electron injection[51,198]. However, the shorter lived Au hole signal around 3.4 eV in Au/TiO$_2$ is not accompanied by a commensurate decay of the ~3.8 eV signal, implying that hole decay in the Au core is affected by the presence of TiO$_2$, which will also be discussed later.
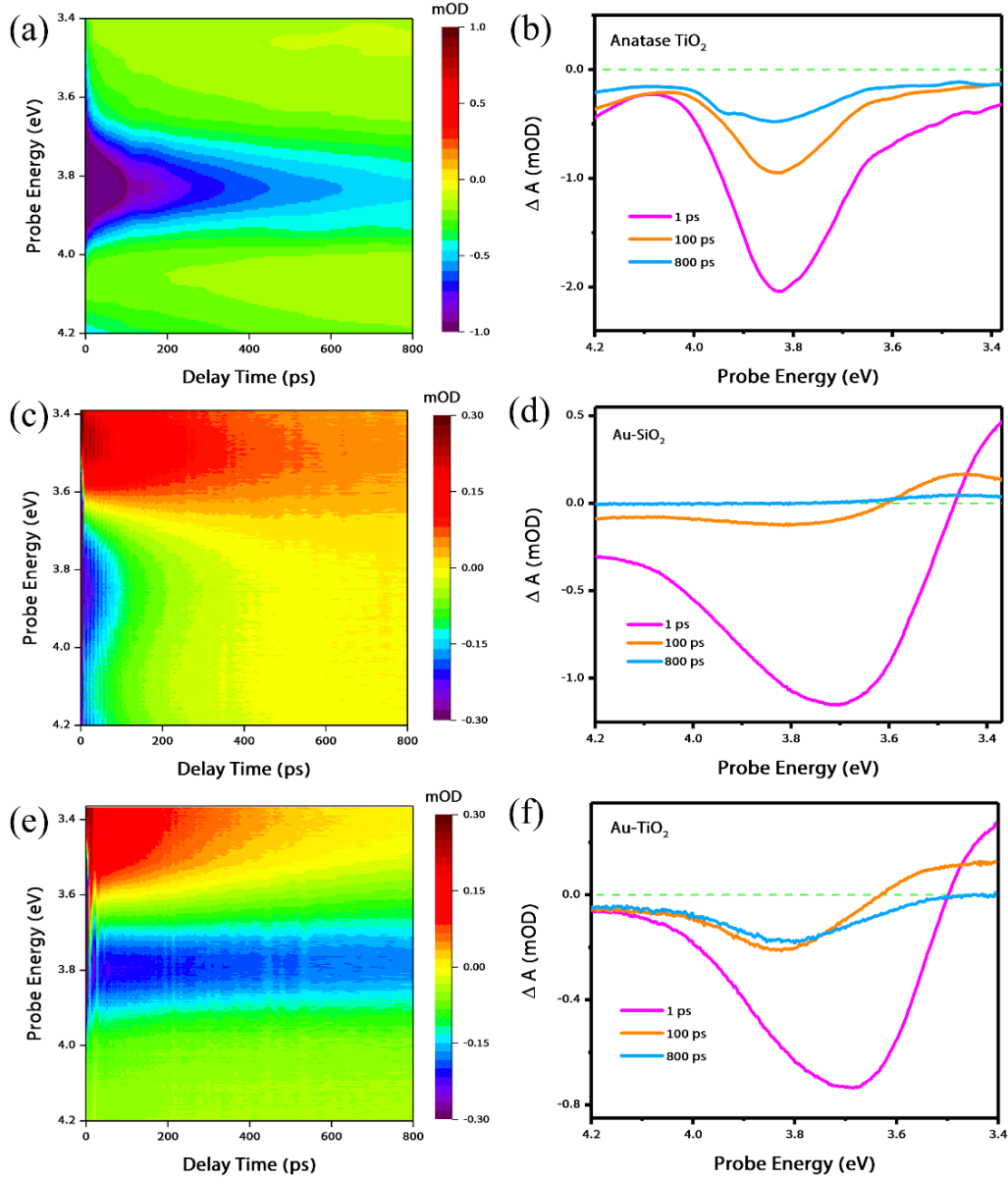
Figure 6.1 Time-energy TA maps and the corresponding spectral traces at 1, 100 and 800 ps. (a, b) bare anatase TiO$_2$ NPs upon above-BG excitation (4.0 eV), (c, d) Au/SiO$_2$ NPs upon plasmon excitation (2.0-2.4 eV), (e, f) Au/TiO$_2$ NPs upon plasmon excitation (2.0-2.4 eV), with pump fluence of ~0.3 mJ/cm^2.
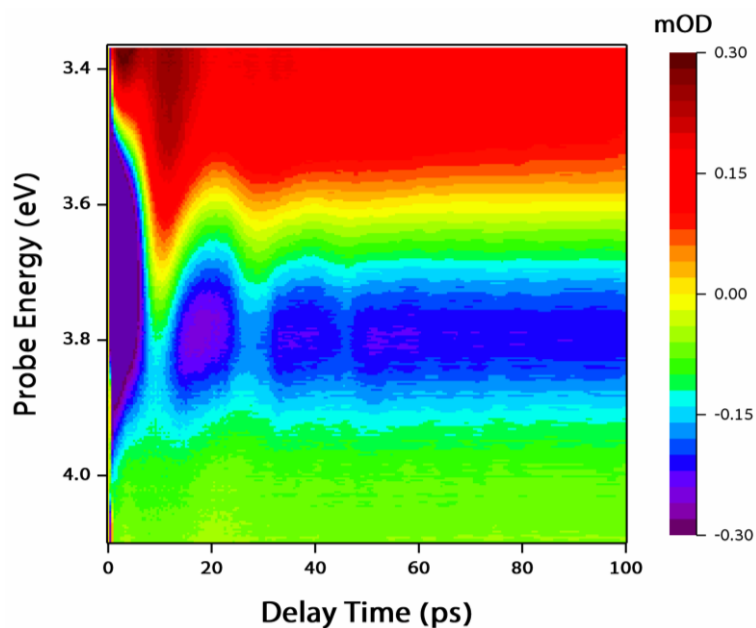
Figure 6.2 Time-energy TA map of the Au/TiO$_2$ NPs upon plasmon excitation (2.0-2.4 eV), within time delay of 100 ps.
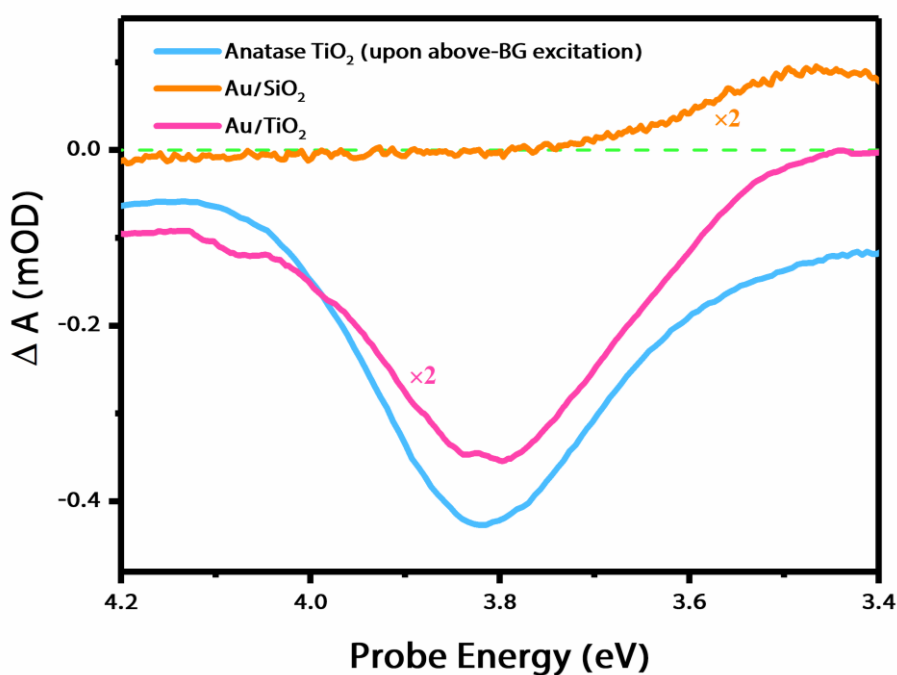
Figure 6.3 Comparison of the TA spectra of the three samples (rescaled for clarity). The blue solid line is the transient response of bare Anatase TiO$_2$ at a delay time of 800 ps upon UV excitation (above-BG excitation, 4.0 eV); The orange and red lines represent the TA spectra of Au/SiO$_2$ and Au/TiO$_2$ at a time delay of 800 ps upon plasmon excitation (below-BG excitation, 2.0-2.4 eV).

6.1.2 Two-photon transition in Au/TiO$_2$

Further insight into the origin of these population and relaxation mechanisms up in the CB of TiO$_2$ is given by the fluence dependence of the various bands at short (10 ps) and long (800 ps) time delays (see Chapter 3 for the method). Figure 6.4 shows log-log plots of the signals of Au/TiO$_2$ at ~3.4 eV and 10 ps time delay (a) and at ~3.8 eV and 10 ps (b) and 800 ps (c) time delays in a range of pump fluences from 0.16 to 0.98 mJ/cm^2. Figure 6.4a exhibits a slope close to 1 (1.13±0.23), which is reasonable, since this band is due to holes in the Au core caused by the LSPR excitation[197]. The slopes of the ~3.8 eV signals are 1.32±0.20 and 1.83±0.21 at 10 and 800 ps time delay, respectively. While the latter points to a two-photon process, the former is intermediate between a one- and two-photon absorption. It can be explained that at 10 ps delay, the interband transition of the Au NP at this probe energy is present (as seen in Figure 6.4c, d and 6.2), which dies away in ~250 ps. The bleach band resulting from the LSPR excitation of Au has a linear dependence with the pump fluence. The ~3.8 eV signal contains the contributions of both the Au NP interband transitions and the excitonic transition of TiO$_2$, the overall signal slopes at this band reflect the fluence dependence of the overlapped behaviour, thus it suggests that the two-photon process coming from the shell of TiO$_2$.

Figure 6.5 and 6.6 also confirm this fact, where the ~3.8 eV signal slopes increase from an ideal minimum value 1 at the beginning to a maximum value 2 at infinite time. Since we have limited data points, the exponential fit model in Figure 6.6 only give us a qualitatively trend with delay time but still this trend seems somehow connected to the decay behavior of Au at ~3.8 eV. Besides, the overlapped signal evolution is also visible in the change in profile of the TA spectra at 10 ps time delay with increasing fluence, shown in Figure 6.7. Whilst for Au/SiO$_2$ the TA profile does not change with pump fluence (Fig. 6.7b), for Au/TiO$_2$ clear changes are observed with the growth of a blue shifted bleach band implying that the TPA induced TiO$_2$ excitionic bleach is taking over the overall bleach contribution with increasing the pump power (Figure 6.7c). Note that for bare TiO$_2$, there is no effect of the pump fluence on the TA spectra, which remain at zero.
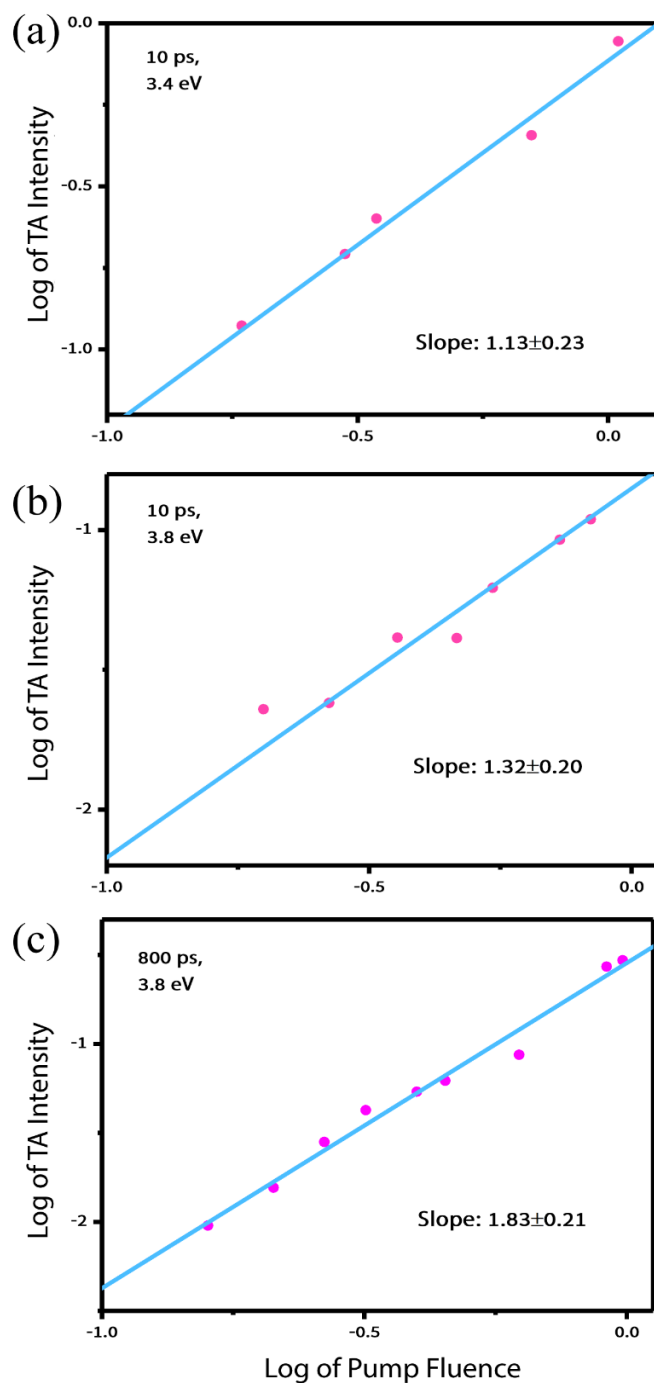
Figure 6.4 Fluence dependence of the Au/TiO$_2$ NPs, displayed as a log-log plot of TA intensity versus pump fluence which varies in a range from 0.16 to 0.98 mJ/cm^2. (a) at 3.4 eV and 10 ps; (b) at 3.8 eV and 10 ps; (c) at 3.8 eV and 800 ps. The red dots are the experimental values, the solid cyan lines represent their linear fits.
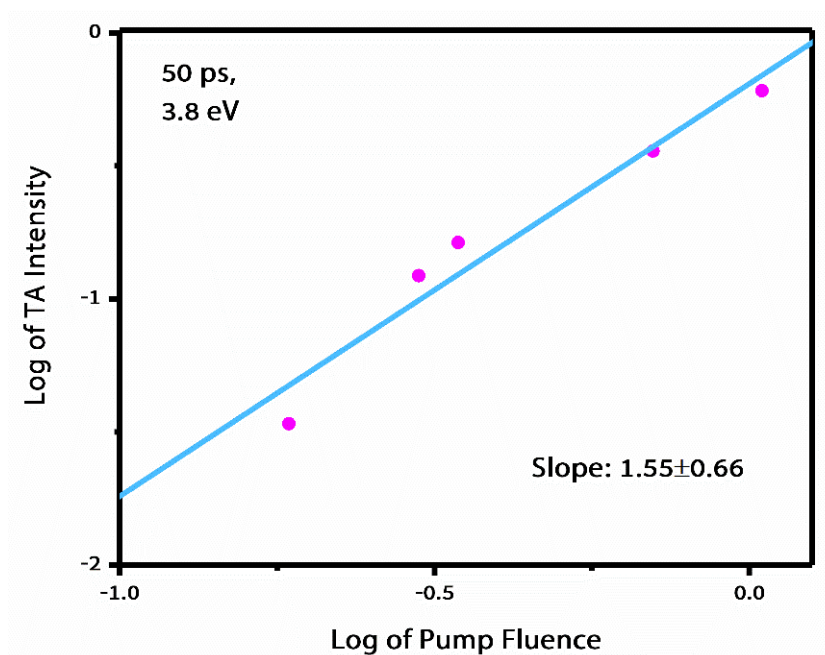
Figure 6.5 Fluence dependence of the Au/TiO$_2$ NPs, displayed as a log-log plot of TA intensity versus pump fluence which varies in a range from 0.16 to 0.98 mJ/cm^2, at 3.8 eV and 50 ps. The red dots are the experimental values, the solid cyan lines represent their linear fits.
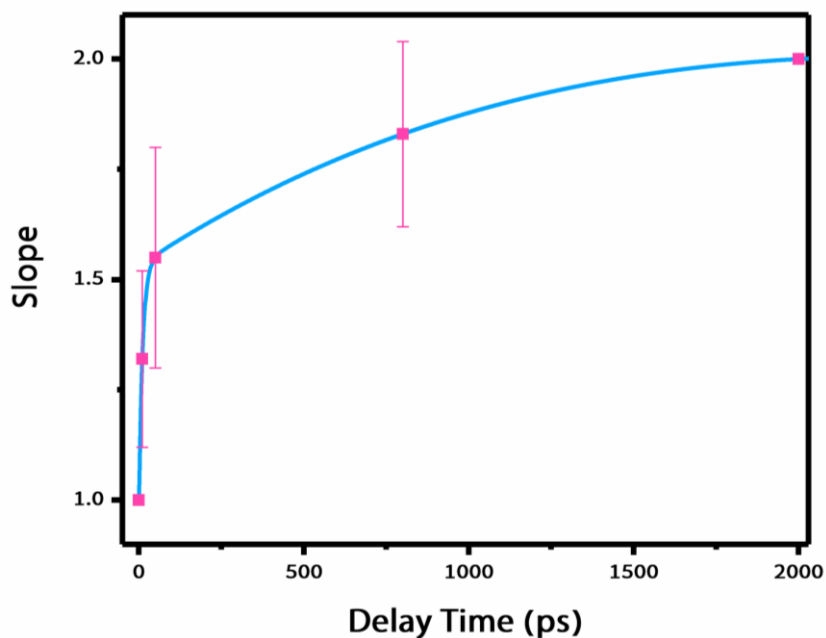
Figure 6.6 Time dependence of the 'log-log' slope of fluence dependence of the Au/TiO$_2$ NPs at 3.8 eV, the cyan solid line relate to the fit which uses an exponential model.
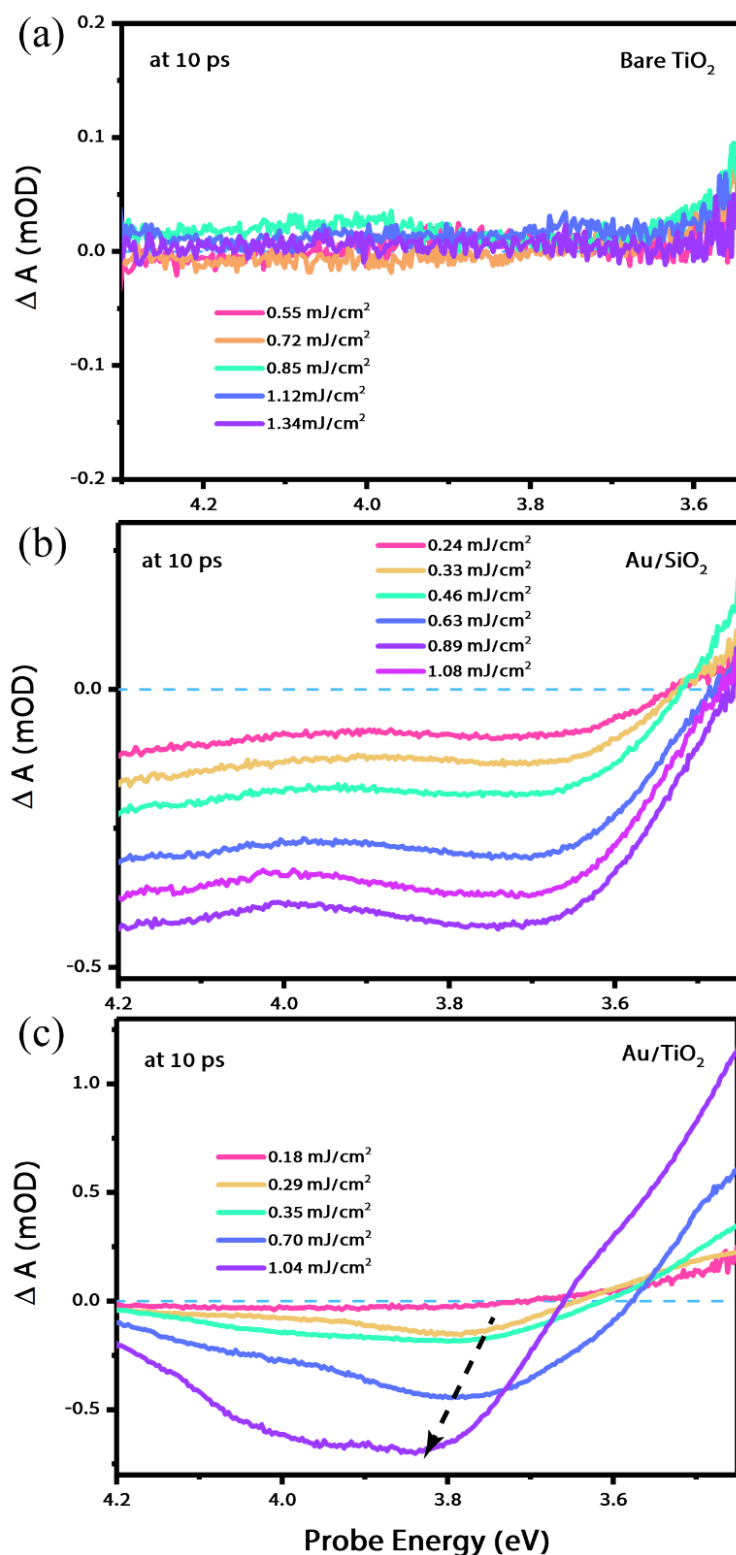
Figure 6.7 Fluence dependence TA spectra at 10 ps of the (a) bare TiO_2 NPs, (b) Au/SiO$_2$ and (c) Au/TiO$_2$, upon plasmon excitation in the visible spectral region (2.0-2.4 eV) with a variety of pump fluences.

At 800 ps time delay, the ~3.8 eV of the Au core is expected to die away and we are left with the signal due to the TiO$_2$ excitonic bleach only. Its slope of 1.83±0.21 reflects the fact that the electrons in the CB of TiO$_2$ are formed by a TPA process, but a smaller proportion of these could also be due to plasmon-induced injected electrons[12,51,199]. Again, we stress that the same range of fluences does not yield any signal due to the presence of electrons in the CB of bare TiO$_2$ NP's (Figure 6.7a). This is in line with previous studies, which used fluences up to 200 mJ/cm^2 of a 10 ps/532 nm laser[139], i.e. two orders of magnitude larger than in the present case, showing no evidence of two-photon excitation. In ref. [89], fs pulse excitation at either 400 nm or 550 nm with fluences up to 53 mJ/cm^2 were used also showing no sign of a multiphoton excitation. On the other hand, in the case of dye-sensitized TiO$_2$ NP, the fluence dependence of the ~3.8 eV band due to injected electrons remained in the linear regime up to ~0.3 mJ/cm^2 of the 550 nm excitation pulse. These observations lead us to conclude that the occurrence of multiphoton excitation of TiO$_2$ in Au/TiO$_2$ core-shell NPs is due to the presence of the Au core and is mediated by the resonance excitation of its LSPR. We next estimated the enhancement factor of the TPA of TiO$_2$ in Au/TiO$_2$ NPs:

The rate of TPA is defined by[200]

$$\frac{dI_0}{dz} = -\beta I_0{}^2 \qquad \text{Eq. 6.1}$$

where I_0 is the laser beam intensity, z is the direction of light propagation, β is the TPA coefficient in cm/W. In the regime of two-photon transition, a quadratic dependence on the laser intensity I_0 appears. The light intensity versus propagation distance becomes:

$$I = \frac{I_0}{1 + \beta l I_0} \qquad \text{Eq. 6.2}$$

I is the intensity of light transmitted through a path length l at a particular wavelength λ and I_0 is the incident light intensity. Thus, the decrease in transmissivity along a path length l in the Z-direction is given by:

$$T = \frac{I}{I_0} = \frac{1}{1 + \beta l I_0} \qquad \text{Eq. 6.3}$$

Therefore, the induced TA signal can be written as:

$$\Delta A = A - A_0 = lg\frac{I_0}{I} = \lg\frac{1 + \beta l I_0}{1} \qquad \text{Eq. 6.4}$$

According to the experimental and theoretical TPA coefficient of titanium dioxide single crystal (rutile), β: 18.6±4.4 cm/GW at 532 nm for c ∥ E configuration; β: 14.8±42.9 cm/GW at 532 nm for c ⊥ E

configuration[201]. Even if Yuichi et al. obtained the β of titanium dioxide with rutile structure, there would not be orders of magnitude difference between anatase and rutile in the visible spectral region. Here, we take 15 cm/GW to simplify the calculation. The optical path length l equals to the thickness of the flow cell: 0.2 mm. The incident light intensity $I_0 = \frac{P}{\pi r^2}$, here we take a power P: 5 mW and a Gaussian laser beam radius r: 100 μm. After adding an enhancement factor n, we obtain:

$$\Delta A \approx \lg \frac{1 + n \cdot 6 \cdot 10^{-9}}{1}$$

Hence,

(1) In pure TiO$_2$ ($n = 1$), $\Delta A \approx 0$, the two-photon process is negligible;

(2) When the enhancement factor $n = 10^9$, $\Delta A \approx 0.85$;

(3) When the enhancement factor $n = 10^8$, $\Delta A \approx 0.20$;

(4) When the enhancement factor $n = 10^7$, $\Delta A \approx 0.03$;

Based on our experimental TA intensity (ΔA: ~0.3), we conclude that in Au/TiO$_2$ NPs, the enhancement factor of the third-order non-linear two-photon process is $\sim 10^8 - 10^9$. This is consistent with the results of surface-enhanced Raman scattering (SERS)[8,9] utilizing LSPR of nano-structured metallic NPs (e.g. Au, Ag, Cu) to amplify Raman signals of molecules at their surface with enhancement factors of $10^6 - 10^{11}$. Besides, simulations show that the local field enhancement of the LSPR to the TPA cross section of the molecular is many orders of magnitude depending on the distance of the NPs and the $|E|^4$ local field[202,203].

6.2 Kinetic traces of Au/TiO$_2$

6.2.1 Trace fitting and comparison

Coming back to Figure 6.1, the simultaneous occurrence of an Au signal at ~3.4-3.5 eV and a signal due to both Au and TiO$_2$ at ~3.8 eV offers additional insights into the fate of charge carriers in the Au/TiO$_2$ NPs. Figure 6.8a, b compares the kinetic traces at ~3.8 eV for bare anatase TiO$_2$, Au/SiO$_2$ and Au/TiO$_2$, and Figure 6.8c, d of the ~3.4 eV band along with their fits (described in Chapter 3). For the signal at ~3.8 eV, both the Au/SiO$_2$ and Au/TiO$_2$ NPs show a similar prompt rise and initial decay, which indicates that the Au response dominates at early times. However, soon after the first few ps, the two traces deviate from each other: the Au/SiO$_2$ shows a decay on a time scale of ~150 ps (see fitting results in Table 6.1), while the decay of Au/TiO$_2$ signal is nearly infinite. To compare the long term behaviour in >200 ps range, we normalize the traces of bare TiO$_2$ and Au/TiO$_2$ at 400 ps (Figure 6.9), it is interesting that the decay of Au/TiO$_2$ is even slower than that of bare TiO$_2$ upon direct above BG

excitation. In addition, oscillations due to coherent acoustic phonon modes are visible, which greatly differ: the Au/SiO$_2$ NPs show an oscillation period of ~10 ps, while the Au/TiO$_2$ NPs exhibit a slower oscillation period of ~18 ps. As far as the ~3.4 eV signal is concerned, again the response is prompt and followed by the phonon oscillations but the decay at longer times is different, with the Au/TiO$_2$ trace fully recovered by ~800 ps, while the Au/SiO$_2$ is still present. The details of the oscillatory patterns will be discussed in Chapter 7. For now, we focus on the exponential parts of the time traces.
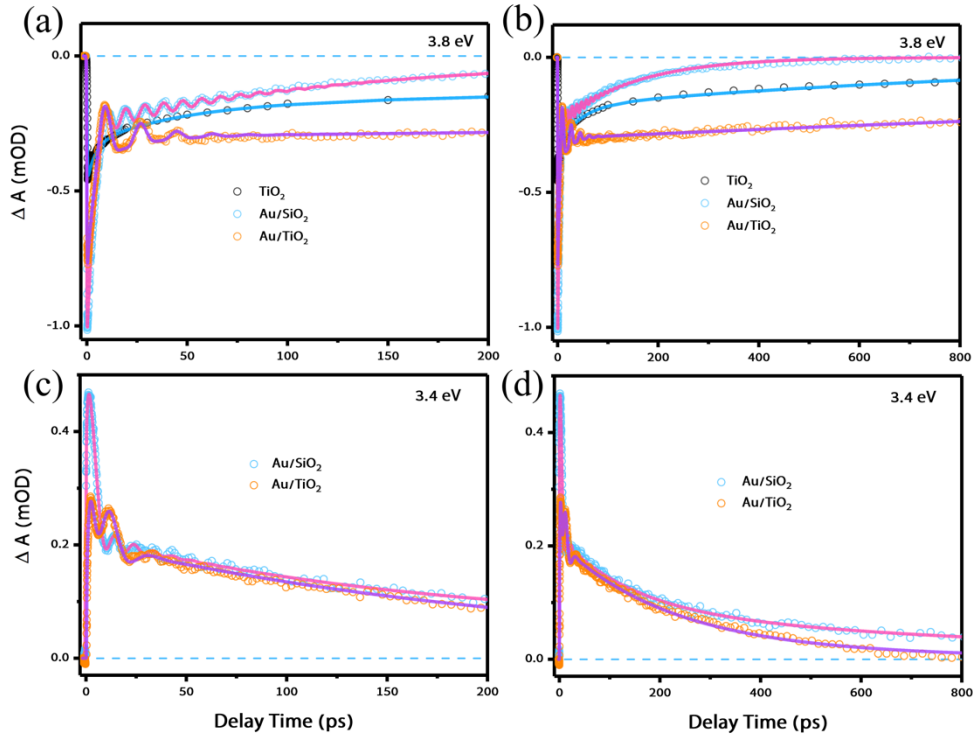
Figure 6.8 Comparison of the TA time traces between bare TiO$_2$, Au/SiO$_2$ and Au/TiO$_2$ NPs at probe energies of (a, b) 3.8 eV; (c, d) 3.4 eV. within (a, c) 200 ps; (b, d) 800 ps. The blue and orange circles are experimental traces, the red and purple solid lines are the fitted time traces.

The results of fitting these traces are given in Table 6.1. They confirm the above described trends. The initial decay time constant τ_1 at ~3.8 eV band is comparable in Au/SiO$_2$ and Au/TiO$_2$, pointing to a common origin of the initial response that is due to the Au core. τ_2 is much larger for Au/TiO$_2$ NPs than for Au/SiO$_2$ ones. The long-lived bleach in Au/TiO$_2$ NPs shows the persistent bleach of the excitonic transition of TiO$_2$, resulting from an excess of electrons in its CB by plasmon-mediated two-photon exciation from the VB and by electron injection from Au NP. This bleach decays slower than that of bare TiO$_2$ upon direct BG excitation (Figure 6.9). One would expect it to be similar or even faster than in the case of bare anatase TiO$_2$ NPs, due to the presence of the Au core. However, in Au/TiO$_2$, as mentioned before, this signal contains the contributions of both TiO$_2$ and Au, the evolution of the overlapped bleach signal basically reflects the decay of electrons originating from both two-photon excited TiO$_2$ and plasmon-excited Au NPs. In addition, the laser induced heating of Au core could

potentially transfer the energy to the TiO_2 lattice, thus the thermal effect of TiO_2 might play a non-negligible role on the transient excitonic behaviour, unfortunately, we cannot directly quantify this in TA experiments, nevertheless, a T-dependent steady-state absorption measurement on bare TiO_2 was investigated and will be discussed later.

Table 6.1: Energies (in eV) and signs of the bands observed by TA spectroscopy, and corresponding exponential decay time constants (τ_1, τ_2, τ_3), amplitudes (A_1, A_2, A_3). All times are in picoseconds.

Sample	Probe band energy (sign)	τ_1	τ_2	τ_3	A_1	A_2	A_3
Au/SiO$_2$	3.8 eV/negative	3.1±0.2	153.5±7.0	-	79%	21%	-
	3.4 eV/positive	-	248.5±11.9	-	-	-	-
Au/TiO$_2$	3.8 eV/negative	2.8±0.2	>3000	-	58%	42%	-
	3.4 eV/positive	-	220.0±5.7	-	-	-	-
Anatase TiO$_2$	3.8 eV/negative	4.1±0.5	44.1±9.0	>800 (~1 ns)	29%	32.0%	39%
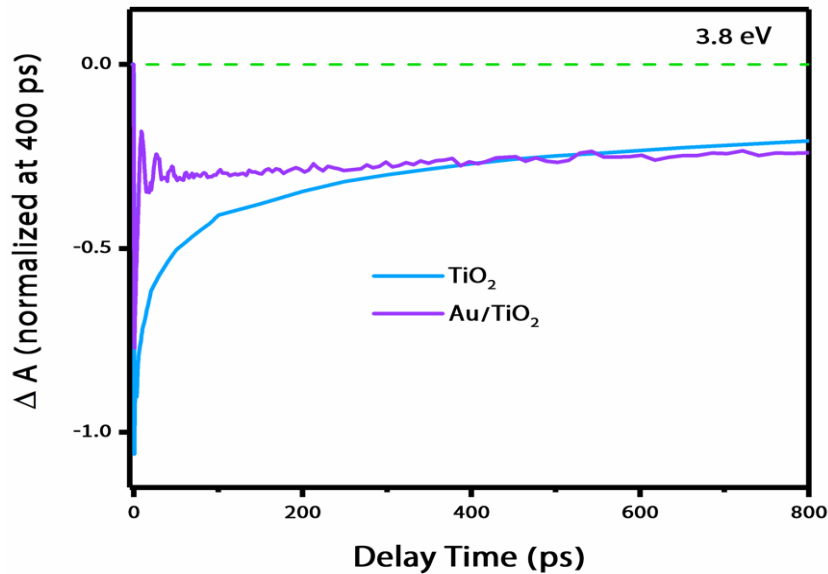
Figure 6.9 TA Time traces of bare TiO_2 upon above-BG excitation (4.0 eV) and Au/TiO$_2$ upon broadband visible excitation (2.0-2.4 eV), normalized at 400 ps.

Here we also have to consider that the kinetic of Au core in Au/TiO$_2$ is different from that of Au/SiO$_2$ because of charge injection, and we may not simply reference the Au kinetic response by comparing the Au/SiO$_2$ sample. Concurrent to this, we note that the signal at ~3.4 eV (due to holes in the Au core) in Au/TiO$_2$ NPs is shorter-lived than in Au/SiO$_2$ NPs. These two observations need to be carefully

correlated. Indeed, the faster decay of the ~3.4 eV band in Au/TiO$_2$ could be due to somewhat different relaxation time within the Au core, due to the presence of the TiO$_2$ shell. Alternatively, it could be due to a back electron transfer from the CB of TiO$_2$. It is well known that the existence of electron injection from Au NP into CB of TiO$_2$ upon LSPR excitation[51,116], thus the charge transfer between Au and TiO$_2$ at the interface reaches an equilibrium after the competition of electron injection and back transfer. According to the reports in UV-excited Au/TiO$_2$ studies[204,205], the Au NPs are regarded to act as an electron sink, the UV light generates free electrons both in the CB of TiO$_2$ and Au NPs, and the electrons migrate from semiconductor to metal which further leads to a E$_F$ equilibration and lift the E$_F$ closer to the CB. The faster decay at ~3.4 eV in Au/TiO$_2$ than that in Au/SiO$_2$ is suggesting that the rate of back electron is larger than electron injection and the overall electron flow is from the CB of TiO$_2$ into Au NP.

In summary, we have performed an anatase TiO$_2$ excitonic bleach related TA spectroscopy in deep-to-near-UV spectral region, monitoring the blocking of the excitonic transition by excess electrons in the CB of TiO$_2$ upon LSPR excitation in Au/TiO$_2$ core-shell NPs. We also compare these results with the charge carrier relaxation in Au/SiO$_2$ and bare TiO$_2$ NPs. We find that the LSPR excitation of the Au core, efficiently induces a two-photon excitation of anatase TiO$_2$, but electrons are also injected into the CB of TiO$_2$ via the one-photon LSPR excitation of the Au NP core. The third-order non-linear process in TiO$_2$ is significantly enhanced due to the presence of Au NP plasmon excitation by a factor of $\sim 10^8 - 10^9$. However, there is also a thermal effect which modifies the excitonic bleach signal in TiO$_2$ at ~3.8 eV (see Chapter 5), resulting in an ultra long-term relaxation behavior at this band in Au/TiO$_2$. The kinetic decay behaviour at the induced absorption band at ~3.5 eV suggests an electron back transfer from two-photon excited anatase TiO$_2$ into Au, implying that the overall electron flow between Au and TiO$_2$ is back electron transfer from the CB of TiO$_2$ to the E$_F$ of Au NPs.

Chapter 7 Phonon coherences in Au NPs

7.1 Vibrational oscillations probed via interband transitions

As already shown in Chapter 4, we observed notable coherent oscillations in Au NPs probing in the interband transition region in deep-UV for the first time. The acoustic vibrations have only been detected previously in the plasmon band, as the signal arises from a LSPR band position periodic shift due to lattice expansion and to hot electron pressure.

Figure 7.1a shows the TA map of Au/SiO_2 NPs, which has three transient bands at ~3.5, ~3.8 and ~4.4 eV, besides the TA signals, all of them display modulations of the TA intensity and last around 100 ps, but with identical frequency at all the bands. Figure 7.1b plots the change of the peak energy position of the ~3.8 eV band with delay time until 400 ps, the relative shift is calculated by subtracting the position of signal maximum at 3.78 eV. It shows that even up to 400 ps, the peak energy position of ~3.8 eV nearly remains the same, which differs with the vibrations reported at the plasmon band[206].

We then extract the oscillation signal by doing a fitting at 3.8 eV band that separate the TA background and the modulations (the methods can be found in Chapter 3), the results are shown in Figure 7.2. The red dots represent the experimental traces while the black solid lines are the fitting curves. We compare the Au NPs with different shell: SiO_2 and anatase TiO_2 (the sample information was given in Chapter 3) and the right panels show the corresponding power spectral density of the oscillations obtained by doing a fast Fourier Transform (FFT). Firstly, both Au/SiO_2 and Au/TiO_2 oscillations can be well reproduced by fitting with a damped cosine function, however, the Au/SiO_2 only show one oscillation component, the Au/TiO_2 NPs have two; secondly, the oscillation frequency of Au/SiO_2 and Au/TiO_2 greatly differ each other, by comparing with the bare Au NPs as described in Figure 1.9 (Chapter 1), the frequency of the breathing model detected at the plasmon band with a similar NP size approximately equals to 3.3 cm^{-1} (~98 GHz) which is close to the Au/SiO_2 NPs (~105 GHz). Although the Au/TiO_2 NPs also show a weak component at ~100 GHz, the dominate oscillation has a frequency of ~ 55 GHz which is almost half of the one in Au/SiO_2. By comparing the power spectral density, the ratio of the two component of ~55 GHz: ~ 100 GHz ≈ 0.78: 0.22. The parameters obtained from the fitting, e.g. oscillation period, decay time are shown in Table 7.1.

Besides, we performed a fluence dependence measurements to investigate the effects of pump power on the coherent oscillations. Figure 7.3a shows that by increasing the excitation fluence, the TA intensity get enhanced but the oscillation frequency has no change (remain ~9.5 ps period). Figure 7.3 b exhibit the relationship between the pump fluences and the TA intensity as well as the oscillation amplitude, while the TA background signal has a linear increase with increasing pump power, the oscillation amplitudes almost remain at the same level. Thus, the excitation intensity seems only affects the TA background but has little influence on the coherent oscillations.

Figure 7.3c plots the TA spectral traces from 20 to 100 ps, the dots at around 3.8 eV represent their TA intensity maximum, and Figure 7.3d shows the normalized spectra. It is clear that the peak of the modulations does not shift with time, suggesting that the vibrations detected in the UV are not sensitive to the NP size change or the size change is small, but there is a slight trend towards a reduction in the overall spectral width especially at < 3.6 eV, this should be due to the spectral overlap between the longer-lived positive (> 3.6 eV) and shorter-lived negative (> 3.7 eV) signals.
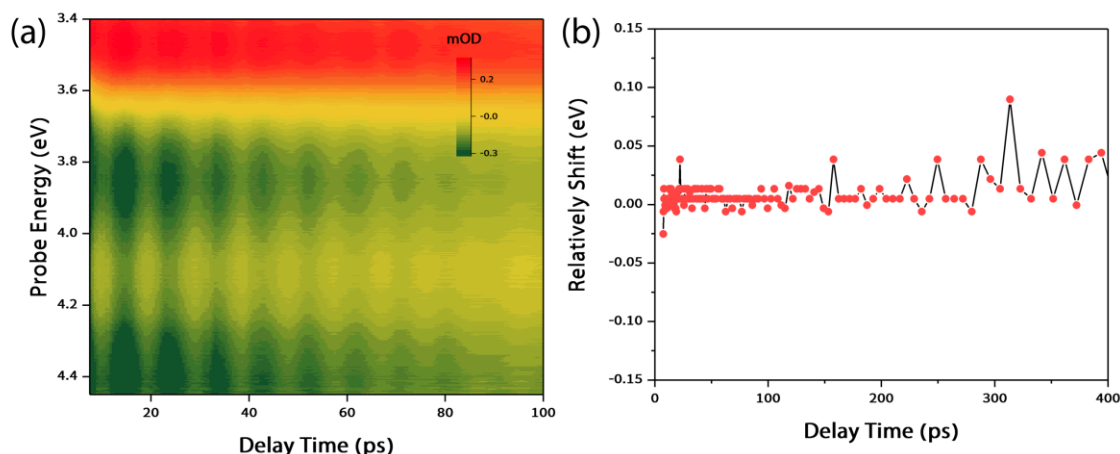
Figure 7.1 (a) TA map of Au/SiO$_2$ NPs, shown as a function of probe pulse energy and time delay between pump and probe; (b) Change in the peak energy position of the ~3.8 eV band with delay time, by looking for the oscillation signal maximum/minimum near the 3.8 eV band at each time delay (the relative shift: peak energy minus 3.78 eV).
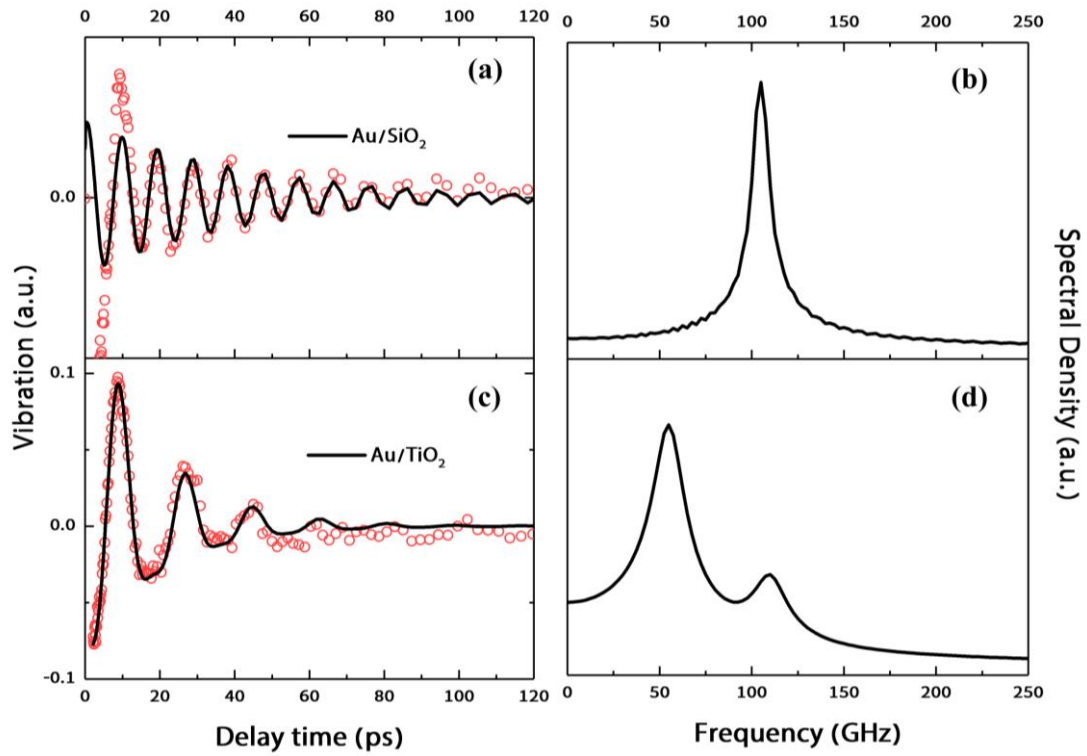
Figure 7.2 (a, c) Acoustic vibration traces of Au/SiO$_2$ and Au/TiO$_2$ NPs, respectively. The NPs are dispersed in water solution, the probe energy lies at 3.8 eV. (b, d) Power spectral density of the oscillations of the vibrational traces in figure a and c.
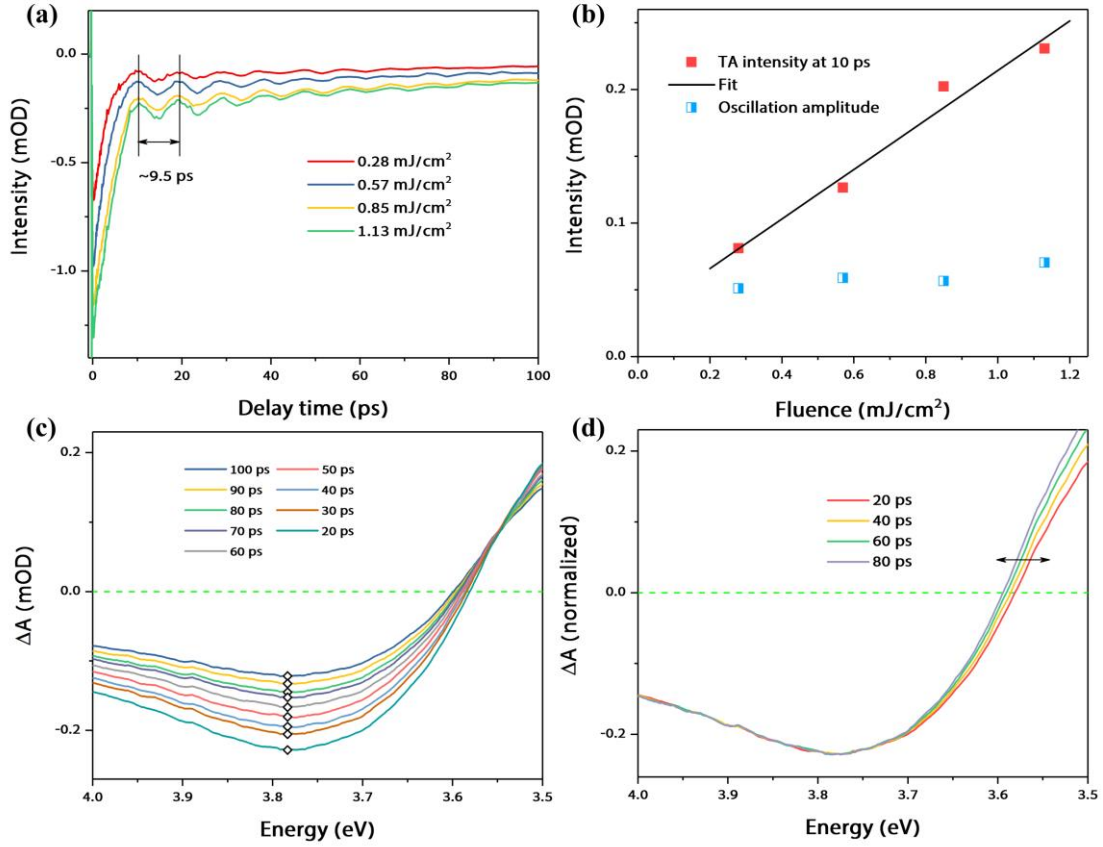
Figure 7.3 (a) the fluence dependence of the Au/SiO$_2$ NP time traces recorded at 3.8 eV, with increasing pump power, the oscillation period remains the same of ~9.5 ps; (b) the relationship between the TA intensity (red squares), oscillation amplitude (blue squares) and pump fluences; (c) the TA spectral traces of Au/SiO$_2$ NPs from 20 to 100 ps, the dots at around 3.8 eV represent the TA intensity maximum; (d) normalized TA spectral traces.

7.2 Lamb theory

To rationalize the differences and similarities between Au/SiO$_2$ and Au/TiO$_2$, we perform a calculation based on Lamb's theory, developed more than a hundred years ago[207], under the approximation of a homogeneous elastic sphere embedded in an infinite elastic medium. Here, we neglect the interactions with environment and the temperature effects on the elastic constants. The size of the Au core is defined by TEM and is around ~25 nm in diameter. Using the extension of the Lamb theory for large NPs[208,209], it provides eigenfrequencies of the n-th order vibrations in an elastic sphere with radius R:

$$\Omega_n = \frac{2\pi R}{\beta_n v_L}$$

Eq. 7.1

Where v_L is the longitudinal sound velocity in Au, β_n can be solved from the transcendental equation:

$$\tan(\beta_n) = \frac{4\beta_n}{4 - \beta_n^2 (\frac{v_L}{v_T})^2}$$
Eq. 7.2

Here, v_T is the transverse sound velocity in the NP. To assign the modulations appearing in the TA signals, we numerically solve the equations and use the values of v_L=3240 m/s and v_T=2030 m/s for sound velocities, and we have used the R=12.5 nm and 30 nm here. The calculated and experimental results are shown in Table 7.1.

Table 7.1 Experimental and theoretical oscillation frequencies of the Au/SiO$_2$ and Au/TiO$_2$ NPs, and their damping time τ_1 τ_2, amplitude ratio A$_1$, A$_2$.

	Sample	Probe band energy (eV)	Ω_1 (GHz)	Ω_2 (GHz)	A$_1$	A$_2$	τ_1 (ps)	τ_2 (ps)
Exp. fitting	Au/SiO$_2$	3.8 eV	101±6.7	-	-	-	17.5±5.1	-
	Au/TiO$_2$	3.8 eV	111±3.4	55.8±6.7	22%	78%	17.1±4.9	18.4±2.7
Lamb. theory	Au NP (R=12.5 nm)	-	103.7 (0-th)	228.2 (1-th)	-	-	-	-
	Au NP (R=30 nm)		41.5 (0-th)	103.4 (1-th)				

7.3 Effects of the shell

Both the Au/SiO$_2$ and Au/TiO$_2$ NPs show a phonon mode with a frequency of around 100 GHz, although the Au/TiO$_2$ has a second stronger oscillating component. Because here the calculation is based on bare Au NPs in an infinite elastic medium, the nearly identical frequency between bare Au and Au/SiO$_2$ NPs suggests that with such thickness (~15-20 nm) of the SiO$_2$ shell, the overall vibration of Au/SiO$_2$ NPs are not significantly affected by the SiO$_2$, this could be due to the fact that SiO$_2$ is transparent in the probe region, or because the Au core and SiO$_2$ shell have similar elastic properties (Young's Modulus for bulk Au: ~79 GPa, Young's Modulus for SiO$_2$: ~75 GPa). In this scenario, if we take the Au/SiO$_2$ core-shell NP as a whole single particle, thus the new radius of the single particle would be ~30 nm, according to the calculation in Table 7.1, the 0-th and 1-th order modes are 41.5 and 103.4 GHz, respectively, what we observed in Au/SiO$_2$ core-shell NPs could be only the first harmonic, n=1. However, the TiO$_2$ shell dramatically alter the oscillation frequency, as the Au/TiO$_2$ sample shows two oscillation modes, surprisingly, these two modes in Au/TiO$_2$ matches well with the calculation in Table

7.1 when computing the particle with R=30 nm, although deviate from them by about ~34% (55.8 vs. 41.5 GHz) and 7.5 % (111 vs. 103.4 GHz), respectively. This means that in Au/TiO$_2$ core-shell NPs, the dominant mode switches from the 1-th to its fundamental one (breathing mode), n=0, compared to Au/SiO$_2$ core-shell NPs, which could be due to the elastic constant of the anatase TiO$_2$ is much larger than Au or SiO$_2$ (Young's Modulus for anatase TiO$_2$: ~250 GPa).

It has been reported that for shell thickness (R$_2$) smaller than or of the order of the core radius, $R_2/R \leq 2$, the fundamental radial mode (0-th) of the full core-shell NP dominates the time-domain data[210], which is in agreement with the measured Au/TiO$_2$ sample but contrary to the Au/SiO$_2$ NPs, suggesting a different contact interface between the Au core and SiO$_2$, anatase TiO$_2$ shells. The SiO$_2$ coating did not involve any chemical binding with the Au core, while the TiO$_2$ is widely reported to have strong interaction in TiO$_2$ supported Au nanostructure, forming Ti-Au, O-Au and Au-Au bonds at the interface[211], and it is more prone to occur on relatively large Au NPs (~9 and ~13 nm diameter) than on small ones (~3 and ~7 nm)[212]. Under this assumption, we conclude that the contact interface is better in Au/TiO$_2$ than that of Au/SiO$_2$ core-shell NPs, which results in this inconsistency with ref[210].

In addition, the damping which is due to energy dissipation in the surrounding medium is most likely inhomogeneous[213], that is, mainly due to the dephasing of the vibrations of the particle induced by its size and shape dispersion[214], this has been confirmed by comparing the computed damping time (~90 ps, R=22.5 nm) assuming a free core-shell nano-spheres with the measured oscillation decay time (~7.5 ps)[210]. Besides, here we exclude any oscillation from the shell, the SiO$_2$ is not excited at all, while anatase TiO$_2$ has much higher oscillation frequency (290 GHz, 620 GHz)[180] than what we observed.

In summary, in visible probe TA experiments, the launch of breathing mode is due to the NP lattice expansion/contraction and is sensitive to the size change, and the energy has a shift with delay time[206], while the vibrations in the deep-UV region only modulate the interband transition intensities but not the energy positions. This might be due to the vibrations in the UV region only change the symmetry and modify the band structure of Au NPs but without large changes in size. For the detection processes, we have observed significant different oscillation frequencies in Au/SiO$_2$ and Au/TiO$_2$ NPs, which we attributed to the different elastic properties and the contact interface of the Au core, SiO$_2$ shell and anatase TiO$_2$ shell.

Chapter 8 Conclusion

In this thesis, we systematically studied Au/SiO$_2$ and Au/TiO$_2$ NPs, using steady-state and time-resolved visible and deep-UV absorption spectroscopies. The research includes the photo-induced charge carrier relaxation probed via interband transitions in Au NPs (chapter 4), disentangling light- and temperature-induced thermal effects in Au NPs (chapter 5), coherent oscillations of Au NPs probed via interband transitions (chapter 7) and photo-induced charge transfer and plasmon-mediated two photon absorption in Au/TiO$_2$ NPs (chapter 6).

The main research presented in this thesis focusing on the photo- and thermally- induced effects on the absorption spectroscopy of Au/SiO$_2$ and Au/TiO$_2$ core-shell NPs. In Au/SiO$_2$, it demonstrates how the Au metal NPs response after absorbing photons or lattice heating, offering a description of disentangling the thermal effects in pump-probe experiments, especially, in different spectral regions both in the UV and visible. By probing in the interband transition region. It identified several transient bands corresponding to inter- and intra- band transitions of Au NPs, which can be used to monitor the decay of electrons and holes upon LSPR excitation. It was found that relaxation of electrons back to the VB is rather slow and commensurate with the thermal evolution of the lattice. Temperature-dependent steady-state absorption measurements and calculations based on T-dependent dielectric function are compared and show great consistency, it shows that while the transient response at LSPR band (visible spectral region) is mostly governed by the temperature effect, the interband transition region (in the UV) is little affected and can be explained in terms of electronic transition. Besides, as far as the wings of the LSPR are concerned, the surrounding medium of the Au NPs can significantly change the behavior at the blue and red sides. In addition, coherent oscillations are observed, which ride on the kinetic traces probed in the high energy UV region, and the oscillation frequencies are dramatically different with the shell of SiO$_2$ or anatase TiO$_2$, this was attributed to the different elastic properties of the Au core and SiO$_2$, anatase TiO$_2$ shell.

In Au/TiO$_2$ NPs, the growing attention in the charge transfer between the Au and TiO$_2$ has driven this research, as the visible to IR probes are ambiguous and not specific to the TMO substrate. The deep-UV TA spectroscopy provides a unique way of probing the excitonic transitions of the substrate material (anatase TiO$_2$), thus it has the ability to detect the signatures of injected electrons based on the excitonic bleach of anatase TiO$_2$. By investigating the bare anatase TiO$_2$, Au/SiO$_2$ and Au/TiO$_2$ NPs upon above and below BG excitation of TiO$_2$, we found that besides the electron injection from the Au core into the CB of TiO$_2$, a two-photon absorption in anatase TiO$_2$ is occurring due to the presence of Au core which has a unique property of LSPR, the enhancement factor of the two-photon absorption cross-section was calculated and found to be over a million. In addition, it was also verified that the overall electron flow in Au/TiO$_2$ core-shell NPs is electron transfer from CB of TiO$_2$ into Au core. However, in the future, more investigations are needed regarding the thermal effects on the exciton behavior of anatase TiO$_2$, to

study the possibility of thermally induced charge transfer and distinguish the contribution of TiO_2 lattice heating from the transient response.

These results provides a more comprehensive understanding of the transient response in Au/SiO_2 and Au/TiO_2 NPs, beneficial in many fields, e.g. electron dynamics in Au NPs, LSPR and interband responses in Au NPs, temperature effects on the absorption spectroscopy of Au NPs will lead us to understand the fundamental and applied aspects of Au NPs in the fields of medical imaging, cancer therapy etc; acoustic vibrations in Au NPs detected in UV could have a bright future for applications in UV-sensitive sensing, optical switching etc.; electron injection and back electron transfer in Au/TiO_2 NPs help us to design and make the use of photovoltaics and solar cells, to solve the problems for their further application with low cost, in a wider sense, it boost the substitution of fossil energy which potentially prevent the global climate change.

Bibliography

1. Freestone, I. & Rehren, T. *From mine to microscope: advances in the study of ancient technology*. (Oxbow books, 2009).

2. Verità, M., Maggetti, M., Saguì, L. & Santopadre, P. Colors of Roman glass: an investigation of the yellow sectilia in the Gorga collection. *Journal of Glass Studies* 39–52 (2013).

3. Polak, A. GLASS: ITS MAKERS AND HIS PUBLIC. (1975).

4. Faraday, M. X. The Bakerian Lecture.—Experimental relations of gold (and other metals) to light. *Philosophical Transactions of the Royal Society of London* 145–181 (1857).

5. Maier, S. A. *Plasmonics: fundamentals and applications*. (Springer Science & Business Media, 2007).

6. Kreibig, U. & Vollmer, M. *Optical properties of metal clusters*. vol. 25 (Springer Science & Business Media, 2013).

7. Kelly, K. L., Coronado, E., Zhao, L. L. & Schatz, G. C. The Optical Properties of Metal Nanoparticles: The Influence of Size, Shape, and Dielectric Environment. *J. Phys. Chem. B* **107**, 668–677 (2003).

8. Le Ru, E. & Etchegoin, P. *Principles of Surface-Enhanced Raman Spectroscopy: and related plasmonic effects*. (Elsevier, 2008).

9. Fang, Y., Seong, N.-H. & Dlott, D. D. Measurement of the distribution of site enhancements in surface-enhanced Raman scattering. *Science* **321**, 388–392 (2008).

10. Mohamed, M. B., Volkov, V., Link, S. & El-Sayed, M. A. Thelightning'gold nanorods: fluorescence enhancement of over a million compared to the gold metal. *Chemical Physics Letters* **317**, 517–523 (2000).

11. Ding, S.-J. *et al.* Magnetic Plasmon-Enhanced Second-Harmonic Generation on Colloidal Gold Nanocups. *Nano Lett.* **19**, 2005–2011 (2019).

12. Du, L., Furube, A., Hara, K., Katoh, R. & Tachiya, M. Ultrafast plasmon induced electron injection mechanism in gold–TiO2 nanoparticle system. *Journal of Photochemistry and Photobiology C: Photochemistry Reviews* **15**, 21–30 (2013).

13. Wood, C. S. & Stevens, M. M. Improving the image of nanoparticles. *Nature* **539**, 505–506 (2016).

14. Baffou, G., Cichos, F. & Quidant, R. Applications and challenges of thermoplasmonics. *Nature Materials* **19**, 946–958 (2020).

15. Harmsen, S. *et al.* Surface-enhanced resonance Raman scattering nanostars for high-precision cancer imaging. *Science Translational Medicine* **7**, 271ra7-271ra7 (2015).

16. Turkevich, J., Stevenson, P. C. & Hillier, J. A study of the nucleation and growth processes in the synthesis of colloidal gold. *Discussions of the Faraday Society* **11**, 55–75 (1951).

17. Linic, S., Christopher, P. & Ingram, D. B. Plasmonic-metal nanostructures for efficient conversion of solar to chemical energy. *Nature materials* **10**, 911 (2011).

18. Pyykkö, P. Additive covalent radii for single-, double-, and triple-bonded molecules and tetrahedrally bonded crystals: a summary. *The Journal of Physical Chemistry A* **119**, 2326–2337 (2015).

19. Heilpern, T. *et al.* Determination of hot carrier energy distributions from inversion of ultrafast pump-probe reflectivity measurements. *Nature Communications* **9**, 1853 (2018).

20. Guerrisi, M., Rosei, R. & Winsemius, P. Splitting of the interband absorption edge in Au. *Physical Review B* **12**, 557 (1975).

21. Christensen, N. E. & Seraphin, B. O. Relativistic band calculation and the optical properties of gold. *Physical Review B* **4**, 3321 (1971).

22. Rangel, T. *et al.* Band structure of gold from many-body perturbation theory. *Physical Review B* **86**, 125125 (2012).

23. Sundararaman, R., Narang, P., Jermyn, A. S., Goddard III, W. A. & Atwater, H. A. Theoretical predictions for hot-carrier generation from surface plasmon decay. *Nature communications* **5**, 5788 (2014).

24. Hansson, G. V. & Flodström, S. A. Photoemission study of the bulk and surface electronic structure of single crystals of gold. *Physical Review B* **18**, 1572 (1978).

25. Guerrisi, M., Rosei, R. & Winsemius, P. Splitting of the interband absorption edge in Au. *Physical Review B* **12**, 557 (1975).

26. Romaniello, P. & de Boeij, P. L. The role of relativity in the optical response of gold within the time-dependent current-density-functional theory. *The Journal of chemical physics* **122**, 164303 (2005).

27. Shahbazyan, T. V. & Stockman, M. I. *Plasmonics: theory and applications*. (Springer, 2013).

28. Palik, E. D. *Handbook of optical constants of solids*. vol. 3 (Academic press, 1998).

29. Juvé, V. *et al.* Cooling dynamics and thermal interface resistance of glass-embedded metal nanoparticles. *Phys. Rev. B* **80**, 195406 (2009).

30. Voisin, C., Del Fatti, N., Christofilos, D. & Vallée, F. Ultrafast Electron Dynamics and Optical Nonlinearities in Metal Nanoparticles. *J. Phys. Chem. B* **105**, 2264–2280 (2001).

31. Jain, P. K., Lee, K. S., El-Sayed, I. H. & El-Sayed, M. A. Calculated Absorption and Scattering Properties of Gold Nanoparticles of Different Size, Shape, and Composition: Applications in Biological Imaging and Biomedicine. *J. Phys. Chem. B* **110**, 7238–7248 (2006).

32. Yeshchenko, O. A., Bondarchuk, I. S., Gurin, V. S., Dmitruk, I. M. & Kotko, A. V. Temperature dependence of the surface plasmon resonance in gold nanoparticles. *Surface Science* **608**, 275–281 (2013).

33. Seol, Y., Carpenter, A. E. & Perkins, T. T. Gold nanoparticles: enhanced optical trapping and sensitivity coupled with significant heating. *Optics letters* **31**, 2429–2431 (2006).

34. Hodak, J. H., Henglein, A. & Hartland, G. V. Coherent Excitation of Acoustic Breathing Modes in Bimetallic Core- Shell Nanoparticles. *The Journal of Physical Chemistry B* **104**, 5053–5055 (2000).

35. Hodak, J. H., Henglein, A. & Hartland, G. V. Photophysics of Nanometer Sized Metal Particles: Electron−Phonon Coupling and Coherent Excitation of Breathing Vibrational Modes. *The Journal of Physical Chemistry B* **104**, 9954–9965 (2000).

36. Crut, A., Maioli, P., Del Fatti, N. & Vallée, F. Acoustic vibrations of metal nano-objects: Time-domain investigations. *Physics Reports* **549**, 1–43 (2015).

37. Hodak, J. H., Henglein, A. & Hartland, G. V. Size dependent properties of Au particles: Coherent excitation and dephasing of acoustic vibrational modes. *J. Chem. Phys.* **111**, 8613–8621 (1999).

38. Fujishima, A. & Honda, K. TiO2 photoelectrochemistry and photocatalysis. *Nature* **238**, 37–38 (1972).

39. Baldini, E. *et al.* Strongly bound excitons in anatase TiO 2 single crystals and nanoparticles. *Nature communications* **8**, 13 (2017).

40. Koch, S. W., Kira, M., Khitrova, G. & Gibbs, H. M. Semiconductor excitons in new light. *Nature materials* **5**, 523–531 (2006).

41. O'regan, B. & Grätzel, M. A low-cost, high-efficiency solar cell based on dye-sensitized colloidal TiO2 films. *nature* **353**, 737 (1991).

42. Nazeeruddin, Md. K., Baranoff, E. & Grätzel, M. Dye-sensitized solar cells: A brief overview. *Solar Energy* **85**, 1172–1178 (2011).

43. Liu, Y., Persson, P., Sundström, V. & Wärnmark, K. Fe N-heterocyclic carbene complexes as promising photosensitizers. *Accounts of chemical research* **49**, 1477–1485 (2016).

44. Kim, Y., Smith, J. G. & Jain, P. K. Harvesting multiple electron–hole pairs generated through plasmonic excitation of Au nanoparticles. *Nature chemistry* **10**, 763 (2018).

45. Hasobe, T. *et al.* Photovoltaic cells using composite nanoclusters of porphyrins and fullerenes with gold nanoparticles. *Journal of the American Chemical Society* **127**, 1216–1228 (2005).

46. Tian, Y. & Tatsuma, T. Mechanisms and Applications of Plasmon-Induced Charge Separation at TiO2 Films Loaded with Gold Nanoparticles. *J. Am. Chem. Soc.* **127**, 7632–7637 (2005).

47. Clavero, C. Plasmon-induced hot-electron generation at nanoparticle/metal-oxide interfaces for photovoltaic and photocatalytic devices. *Nature Photonics* **8**, 95 (2014).

48. Zhang, Y., Wang, Z. & Lang, X. Merging visible light photocatalysis of dye-sensitized TiO 2 with TEMPO: the selective aerobic oxidation of alcohols. *Catalysis Science & Technology* **7**, 4955–4963 (2017).

49. ávan Bokhoven, J. A. Transient mid-IR study of electron dynamics in TiO 2 conduction band. *Analyst* **138**, 1966–1970 (2013).

50. Ratchford, D. C., Dunkelberger, A. D., Vurgaftman, I., Owrutsky, J. C. & Pehrsson, P. E. Quantification of Efficient Plasmonic Hot-Electron Injection in Gold Nanoparticle–TiO2 Films. *Nano letters* **17**, 6047–6055 (2017).

51. Furube, A., Du, L., Hara, K., Katoh, R. & Tachiya, M. Ultrafast plasmon-induced electron transfer from gold nanodots into TiO2 nanoparticles. *Journal of the American Chemical Society* **129**, 14852–14853 (2007).

52. Margaritondo, G. Interface states at semiconductor junctions. *Rep. Prog. Phys.* **62**, 765–808 (1999).

53. Inouye, H., Tanaka, K., Tanahashi, I. & Hirao, K. Ultrafast dynamics of nonequilibrium electrons in a gold nanoparticle system. *Physical Review B* **57**, 11334 (1998).

54. Logunov, S. L., Ahmadi, T. S., El-Sayed, M. A., Khoury, J. T. & Whetten, R. L. Electron Dynamics of Passivated Gold Nanocrystals Probed by Subpicosecond Transient Absorption Spectroscopy. *J. Phys. Chem. B* **101**, 3713–3719 (1997).

55. Ahmadi, T. S., Logunov, S. L. & El-Sayed, M. A. Picosecond Dynamics of Colloidal Gold Nanoparticles. *J. Phys. Chem.* **100**, 8053–8056 (1996).

56. Kruglyak, V. V., Hicken, R. J., Matousek, P. & Towrie, M. Spectroscopic study of optically induced ultrafast electron dynamics in gold. *Phys. Rev. B* **75**, 035410 (2007).

57. Inouye, H., Tanaka, K., Tanahashi, I. & Hirao, K. Ultrafast dynamics of nonequilibrium electrons in a gold nanoparticle system. *Physical Review B* **57**, 11334 (1998).

58. Minutella, E., Schulz, F. & Lange, H. Excitation-Dependence of Plasmon-Induced Hot Electrons in Gold Nanoparticles. *J. Phys. Chem. Lett.* **8**, 4925–4929 (2017).

59. Ahmadi, T. S., Logunov, S. L. & El-Sayed, M. A. Picosecond Dynamics of Colloidal Gold Nanoparticles. *J. Phys. Chem.* **100**, 8053–8056 (1996).

60. Fann, W. S., Storz, R., Tom, H. W. K. & Bokor, J. Electron thermalization in gold. *Physical Review B* **46**, 13592 (1992).

61. Sun, C.-K., Vallée, F., Acioli, L., Ippen, E. P. & Fujimoto, J. G. Femtosecond investigation of electron thermalization in gold. *Phys. Rev. B* **48**, 12365–12368 (1993).

62. Hass, G. & Hadley, L. American Institute of Physics Handbook. *McGraw-Hill, New York* 6–124 (1972).

63. Hodak, J. H., Henglein, A. & Hartland, G. V. *Photophysics of nanometer sized metal particles: electron- phonon coupling and coherent excitation of breathing vibrational modes*. (ACS Publications, 2000).

64. Hodak, J., Martini, I. & Hartland, G. V. Ultrafast study of electron–phonon coupling in colloidal gold particles. *Chemical physics letters* **284**, 135–141 (1998).

65. Hodak, J. H., Martini, I. & Hartland, G. V. Spectroscopy and dynamics of nanometer-sized noble metal particles. *The Journal of Physical Chemistry B* **102**, 6958–6967 (1998).

66. Hartland, G. V. Optical studies of dynamics in noble metal nanostructures. *Chemical reviews* **111**, 3858–3887 (2011).

67. Hartland, G. V. Coherent excitation of vibrational modes in metallic nanoparticles. *Annu. Rev. Phys. Chem.* **57**, 403–430 (2006).

68. Del Fatti, N., Bouffanais, R., Vallée, F. & Flytzanis, C. Nonequilibrium Electron Interactions in Metal Films. *Phys. Rev. Lett.* **81**, 922–925 (1998).

69. Hu, M. & Hartland, G. V. Heat dissipation for Au particles in aqueous solution: relaxation time versus size. *The Journal of Physical Chemistry B* **106**, 7029–7033 (2002).

70. Hu, M., Wang, X., Hartland, G. V., Salgueiriño-Maceira, V. & Liz-Marzán, L. M. Heat dissipation in gold–silica core-shell nanoparticles. *Chemical Physics Letters* **372**, 767–772 (2003).

71. Hodak, J. H., Martini, I. & Hartland, G. V. Observation of acoustic quantum beats in nanometer sized Au particles. *The Journal of chemical physics* **108**, 9210–9213 (1998).

72. Tas, G. & Maris, H. J. Electron diffusion in metals studied by picosecond ultrasonics. *Physical Review B* **49**, 15046 (1994).

73. Kittel, C. Introduction to solid state physics, John Wiley & Sons. *Inc., New York* (2005).

74. Chang, S.-S., Shih, C.-W., Chen, C.-D., Lai, W.-C. & Wang, C. R. C. The Shape Transition of Gold Nanorods. *Langmuir* **15**, 701–709 (1999).

75. Takami, A., Kurita, H. & Koda, S. Laser-induced size reduction of noble metal particles. *The Journal of Physical Chemistry B* **103**, 1226–1232 (1999).

76. Stoll, T. *et al.* Time-resolved investigations of the cooling dynamics of metal nanoparticles: impact of environment. *The Journal of Physical Chemistry C* **119**, 12757–12764 (2015).

77. Katayama, T., Setoura, K., Werner, D., Miyasaka, H. & Hashimoto, S. Picosecond-to-Nanosecond Dynamics of Plasmonic Nanobubbles from Pump−Probe Spectral Measurements of Aqueous Colloidal Gold Nanoparticles. *Langmuir* **30**, 9504–9513 (2014).

78. Del Fatti, N., Vallée, F., Flytzanis, C., Hamanaka, Y. & Nakamura, A. Electron dynamics and surface plasmon resonance nonlinearities in metal nanoparticles. *Chemical Physics* **251**, 215–226 (2000).

79. Voisin, C. *et al.* Size-dependent electron-electron interactions in metal nanoparticles. *Physical review letters* **85**, 2200 (2000).

80. Stoll, T., Maioli, P., Crut, A., Del Fatti, N. & Vallée, F. Advances in femto-nano-optics: ultrafast nonlinearity of metal nanoparticles. *The European Physical Journal B* **87**, 260 (2014).

81. Hulst, H. C. & van de Hulst, H. C. *Light scattering by small particles*. (Courier Corporation, 1981).

82. Bohren, C. F. & Huffman, D. R. *Absorption and scattering of light by small particles*. (John Wiley & Sons, 2008).

83. Jackson, J. D. *Classical electrodynamics*. (AAPT, 1999).

84. Wokaun, A., Gordon, J. P. & Liao, P. F. Radiation damping in surface-enhanced Raman scattering. *Physical Review Letters* **48**, 957 (1982).

85. Plech, A., Kotaidis, V., Grésillon, S., Dahmen, C. & Von Plessen, G. Laser-induced heating and melting of gold nanoparticles studied by time-resolved x-ray scattering. *Physical Review B* **70**, 195423 (2004).

86. Wilson, O. M., Hu, X., Cahill, D. G. & Braun, P. V. Colloidal metal particles as probes of nanoscale thermal transport in fluids. *Physical Review B* **66**, 224301 (2002).

87. Plech, A. *et al.* Time-resolved X-ray diffraction on laser-excited metal nanoparticles. *EPL (Europhysics Letters)* **61**, 762 (2003).

88. Hodak, J. H., Henglein, A. & Hartland, G. V. Photophysics of Nanometer Sized Metal Particles: Electron−Phonon Coupling and Coherent Excitation of Breathing Vibrational Modes. *J. Phys. Chem. B* **104**, 9954–9965 (2000).

89. Baldini, E. *et al.* Interfacial electron injection probed by a substrate-specific excitonic signature. *Journal of the American Chemical Society* **139**, 11584–11589 (2017).

90. Baldini, E., Palmieri, T., Pomarico, E., Auböck, G. & Chergui, M. Clocking the Ultrafast Electron Cooling in Anatase Titanium Dioxide Nanoparticles. *ACS Photonics* **5**, 1241–1249 (2018).

91. Christensen, N. E. High-energy band structure of gold. *Physical Review B* **13**, 2698 (1976).

92. Ramchandani, M. G. Energy band structure of gold. *Journal of Physics C: Solid State Physics* **3**, S1 (1970).

93. Losurdo, M. *et al.* Size dependence of the dielectric function of silicon-supported plasmonic gold nanoparticles. *Physical Review B* **82**, 155451 (2010).

94. Lässer, R. & Smith, N. V. Interband optical transitions in gold in the photon energy range 2–25 eV. *Solid State Communications* **37**, 507–509 (1981).

95. Rangel, T. *et al.* Band structure of gold from many-body perturbation theory. *Physical Review B* **86**, 125125 (2012).

96. Segall, B. Fermi surface and energy bands of copper. *Physical Review* **125**, 109 (1962).

97. Del Fatti, N., Arbouet, A. & Vallée, F. Femtosecond optical investigation of electron–lattice interactions in an ensemble and a single metal nanoparticle. *Applied Physics B* **84**, 175–181 (2006).

98. Ishida, Y. *et al.* Non-thermal hot electrons ultrafastly generating hot optical phonons in graphite. *Scientific Reports* **1**, 64 (2011).

99. Govorov, A. O. & Richardson, H. H. Generating heat with metal nanoparticles. *Nano Today* **2**, 30–38 (2007).

100. Richardson, H. H., Carlson, M. T., Tandler, P. J., Hernandez, P. & Govorov, A. O. Experimental and Theoretical Studies of Light-to-Heat Conversion and Collective Heating Effects in Metal Nanoparticle Solutions. *Nano Lett.* **9**, 1139–1146 (2009).

101. Lukianova-Hleb, E. *et al.* Plasmonic Nanobubbles as Transient Vapor Nanobubbles Generated around Plasmonic Nanoparticles. *ACS Nano* **4**, 2109–2123 (2010).

102. Carlson, M. T., Green, A. J. & Richardson, H. H. Superheating Water by CW Excitation of Gold Nanodots. *Nano Lett.* **12**, 1534–1537 (2012).

103. Fang, Z. *et al.* Evolution of Light-Induced Vapor Generation at a Liquid-Immersed Metallic Nanoparticle. *Nano Lett.* **13**, 1736–1742 (2013).

104.   Neumann, O. *et al.* Solar Vapor Generation Enabled by Nanoparticles. *ACS Nano* **7**, 42–49 (2013).

105.   Yeshchenko, O. A., Kutsevol, N. V. & Naumenko, A. P. Light-Induced Heating of Gold Nanoparticles in Colloidal Solution: Dependence on Detuning from Surface Plasmon Resonance. *Plasmonics* **11**, 345–350 (2016).

106.   Ferrera, M. *et al.* Thermometric Calibration of the Ultrafast Relaxation Dynamics in Plasmonic Au Nanoparticles. *ACS Photonics* **7**, 959–966 (2020).

107.   Hache, F., Ricard, D., Flytzanis, C. & Kreibig, U. The optical kerr effect in small metal particles and metal colloids: The case of gold. *Appl. Phys. A* **47**, 347–357 (1988).

108.   Perner, M. *et al.* Optically Induced Damping of the Surface Plasmon Resonance in Gold Colloids. *Phys. Rev. Lett.* **78**, 2192–2195 (1997).

109.   Sasai, J. & Hirao, K. Relaxation behavior of nonlinear optical response in borate glasses containing gold nanoparticles. *Journal of Applied Physics* **89**, 4548–4553 (2001).

110.   Mohamed, M. B., Ahmadi, T. S., Link, S., Braun, M. & El-Sayed, M. A. Hot electron and phonon dynamics of gold nanoparticles embedded in a gel matrix. *Chemical Physics Letters* **343**, 55–63 (2001).

111.   Link, S. *et al.* Hot Electron Relaxation Dynamics of Gold Nanoparticles Embedded in MgSO4 Powder Compared To Solution: The Effect of the Surrounding Medium. *J. Phys. Chem. B* **106**, 945–955 (2002).

112.   Stoll, T. *et al.* Time-resolved investigations of the cooling dynamics of metal nanoparticles: impact of environment. *The Journal of Physical Chemistry C* **119**, 12757–12764 (2015).

113.   Zhang, X. *et al.* Transient localized surface plasmon induced by femtosecond interband excitation in gold nanoparticles. *Scientific Reports* **8**, 10499 (2018).

114.   Aiboushev, A. *et al.* Spectral properties of the surface plasmon resonance and electron injection from gold nanoparticles to TiO2 mesoporous film: femtosecond study. *Photochem. Photobiol. Sci.* **12**, 631–637 (2013).

115.   Radzig, M. *et al.* Femtosecond Spectroscopy of Au Hot-Electron Injection into TiO2: Evidence for Au/TiO2 Plasmon Photocatalysis by Bactericidal Au Ions and Related Phenomena. *Nanomaterials* **9**, 217 (2019).

116.   Brongersma, M. L., Halas, N. J. & Nordlander, P. Plasmon-induced hot carrier science and technology. *Nature nanotechnology* **10**, 25 (2015).

117.   Groeneveld, R. H., Sprik, R. & Lagendijk, A. Femtosecond spectroscopy of electron-electron and electron-phonon energy relaxation in Ag and Au. *Physical Review B* **51**, 11433 (1995).

118.   Wang, L. *et al.* Slow Charge Carrier Relaxation in Gold Nanoparticles. *The Journal of Physical Chemistry C* **124**, 24322–24330 (2020).

119.   Hu, M., Wang, X., Hartland, G. V., Salgueiriño-Maceira, V. & Liz-Marzán, L. M. Heat dissipation in gold–silica core-shell nanoparticles. *Chemical Physics Letters* **372**, 767–772 (2003).

120.   Hu, M. & Hartland, G. V. Heat dissipation for Au particles in aqueous solution: relaxation time versus size. *The Journal of Physical Chemistry B* **106**, 7029–7033 (2002).

121.   Hartland, G. V., Besteiro, L. V., Johns, P. & Govorov, A. O. What's so hot about electrons in metal nanoparticles? *ACS Energy Letters* **2**, 1641–1653 (2017).

122.   O'Keeffe, P. *et al.* Disentangling the Temporal Dynamics of Nonthermal Electrons in Photoexcited Gold Nanostructures. *Laser & Photonics Reviews* **15**, 2100017 (2021).

123.   Doremus, R. H. Optical Properties of Small Gold Particles. *J. Chem. Phys.* **40**, 2389–2396 (1964).

124.   Kawabata, A. & Kubo, R. Electronic Properties of Fine Metallic Particles. II. Plasma Resonance Absorption. *J. Phys. Soc. Jpn.* **21**, 1765–1772 (1966).

125.   Kruglyak, V. V., Hicken, R. J., Matousek, P. & Towrie, M. Spectroscopic study of optically induced ultrafast electron dynamics in gold. *Phys. Rev. B* **75**, 035410 (2007).

126.   Yeshchenko, O. A., Bondarchuk, I. S., Gurin, V. S., Dmitruk, I. M. & Kotko, A. V. Temperature dependence of the surface plasmon resonance in gold nanoparticles. *Surface Science* **608**, 275–281 (2013).

127.   Ferrera, M. *et al.* Thermometric calibration of the ultrafast relaxation dynamics in plasmonic Au nanoparticles. *ACS Photonics* **7**, 959–966 (2020).

128.   Link, S. & El-Sayed, M. A. Size and Temperature Dependence of the Plasmon Absorption of Colloidal Gold Nanoparticles. *J. Phys. Chem. B* **103**, 4212–4217 (1999).

129.   Magnozzi, M., Ferrera, M., Mattera, L., Canepa, M. & Bisio, F. Plasmonics of Au nanoparticles in a hot thermodynamic bath. *Nanoscale* **11**, 1140–1146 (2019).

130.   Bouillard, J.-S. G., Dickson, W., O'Connor, D. P., Wurtz, G. A. & Zayats, A. V. Low-Temperature Plasmonics of Metallic Nanostructures. *Nano Lett.* **12**, 1561–1565 (2012).

131.   Magnozzi, M., Ferrera, M., Mattera, L., Canepa, M. & Bisio, F. Plasmonics of Au nanoparticles in a hot thermodynamic bath. *Nanoscale* **11**, 1140–1146 (2019).

132.   Du, L., Furube, A., Hara, K., Katoh, R. & Tachiya, M. Ultrafast plasmon induced electron injection mechanism in gold–TiO2 nanoparticle system. *Journal of Photochemistry and Photobiology C: Photochemistry Reviews* **15**, 21–30 (2013).

133.   Du, L. *et al.* Plasmon-induced charge separation and recombination dynamics in gold- TiO2 nanoparticle systems: dependence on TiO2 particle size. *The Journal of Physical Chemistry C* **113**, 6454–6462 (2009).

134.   Furube, A. *et al.* Ultrafast direct and indirect electron-injection processes in a photoexcited dye-sensitized nanocrystalline zinc oxide film: The importance of exciplex intermediates at the surface. *J Phys Chem B* **108**, 12583–12592 (2004).

135.   Benko, G., Kallioinen, J., Korppi-Tommola, J. E. I., Yartsev, A. P. & Sundstrom, V. Photoinduced ultrafast dye-to-semiconductor electron injection from nonthermalized and thermalized donor states. *Journal of the American Chemical Society* **124**, 489–493 (2002).

136. Benko, G., Myllyperkio, P., Pan, J., Yartsev, A. P. & Sundstrom, V. Photoinduced electron injection from Ru(dcbPY)(2)(NCS)(2) to SnO2 and TiO2 nanocrystalline films. *Journal of the American Chemical Society* **125**, 1118–1119 (2003).

137. Nemec, H. *et al.* Influence of the Electron-Cation Interaction on Electron Mobility in Dye-Sensitized ZnO and TiO2 Nanocrystals: A Study Using Ultrafast Terahertz Spectroscopy. *Phys Rev Lett* **104**, (2010).

138. Anderson, N. A. & Lian, T. Ultrafast electron injection from metal polypyridyl complexes to metal-oxide nanocrystalline thin films. *Coordin Chem Rev* **248**, 1231–1246 (2004).

139. Rittmann-Frank, M. H. *et al.* Mapping of the Photoinduced Electron Traps in TiO2 by Picosecond X-ray Absorption Spectroscopy. *Angewandte Chemie International Edition* **53**, 5858–5862 (2014).

140. Ruan, Q., Shao, L., Shu, Y., Wang, J. & Wu, H. Growth of monodisperse gold nanospheres with diameters from 20 nm to 220 nm and their core/satellite nanostructures. *Advanced Optical Materials* **2**, 65–73 (2014).

141. Fang, C. *et al.* (Gold core)/(titania shell) nanostructures for plasmon-enhanced photon harvesting and generation of reactive oxygen species. *Energy & Environmental Science* **7**, 3431–3438 (2014).

142. Long, H., Chen, A., Yang, G., Li, Y. & Lu, P. Third-order optical nonlinearities in anatase and rutile TiO2 thin films. *Thin Solid Films* **517**, 5601–5604 (2009).

143. Portuondo-Campa, E., Tortschanoff, A., van Mourik, F. & Chergui, M. Ultrafast nonresonant response of TiO2 nanostructured films. *J. Chem. Phys.* **128**, 244718 (2008).

144. Sciancalepore, C. *et al.* TiO2nanorods/PMMA copolymer-based nanocomposites: highly homogeneous linear and nonlinear optical material. *Nanotechnology* **19**, 205705 (2008).

145. Iliopoulos, K. *et al.* Nonlinear optical response of titanium oxide nanostructured thin films. *Thin Solid Films* **518**, 1174–1176 (2009).

146. Liao, H. B., Xiao, R. F., Wang, H., Wong, K. S. & Wong, G. K. L. Large third-order optical nonlinearity in Au:TiO2 composite films measured on a femtosecond time scale. *Appl. Phys. Lett.* **72**, 1817–1819 (1998).

147. Xiao-Niu, P., Min, L., Liao, Y., Xian, Z. & Li, Z. Annealing Induced Aggregations and Sign Alterations of Nonlinear Absorption and Refraction of Dense Au Nanoparticles in TiO 2 Films. *Chinese Phys. Lett.* **25**, 4171–4173 (2008).

148. Kyoung, M. & Lee, M. *Z-scan Studies on the Third-order Optical Nonlinearity of Au Nanoparticles Embedded in TiO2*. (1999).

149. Torres-Torres, D. *et al.* Inhibition of the two-photon absorption response exhibited by a bilayer TiO2 film with embedded Au nanoparticles. *Opt. Express, OE* **18**, 16406–16417 (2010).

150. Anija, M. *et al.* Nonlinear light transmission through oxide-protected Au and Ag nanoparticles: an investigation in the nanosecond domain. *Chemical Physics Letters* **380**, 223–229 (2003).

151. Liao, H., Lu, W., Yu, S., Wen, W. & Wong, G. K. L. Optical characteristics of gold nanoparticle-doped multilayer thin film. *J. Opt. Soc. Am. B, JOSAB* **22**, 1923–1926 (2005).

152. Auböck, G., Consani, C., van Mourik, F. & Chergui, M. Ultrabroadband femtosecond two-dimensional ultraviolet transient absorption. *Optics letters* **37**, 2337–2339 (2012).

153. Mooney, J. & Kambhampati, P. Get the Basics Right: Jacobian Conversion of Wavelength and Energy Scales for Quantitative Analysis of Emission Spectra. *J. Phys. Chem. Lett.* **4**, 3316–3318 (2013).

154. Zewail, A. H. Laser femtochemistry. *Science* **242**, 1645–1653 (1988).

155. Slavov, C., Hartmann, H. & Wachtveitl, J. Implementation and evaluation of data analysis strategies for time-resolved optical spectroscopy. *Analytical chemistry* **87**, 2328–2336 (2015).

156. Zhou, L. *et al.* Quantifying hot carrier and thermal contributions in plasmonic photocatalysis. *Science* **362**, 69–72 (2018).

157. Knight, M. W., Sobhani, H., Nordlander, P. & Naomi J. Photodetection with active optical antennas. *Science* **332**, 702–704 (2011).

158. Giannini, V., Fernández-Domínguez, A. I., Heck, S. C. & Maier, S. A. Plasmonic nanoantennas: fundamentals and their use in controlling the radiative properties of nanoemitters. *Chemical reviews* **111**, 3888–3912 (2011).

159. Mukherjee, S. *et al.* Hot electrons do the impossible: plasmon-induced dissociation of H2 on Au. *Nano letters* **13**, 240–247 (2013).

160. Kim, M., Lin, M., Son, J., Xu, H. & Nam, J.-M. Hot-Electron-Mediated Photochemical Reactions: Principles, Recent Advances, and Challenges. *Advanced Optical Materials* **5**, 1700004 (2017).

161. Takahashi, Y. & Tatsuma, T. Solid state photovoltaic cells based on localized surface plasmon-induced charge separation. *Applied Physics Letters* **99**, 182110 (2011).

162. Wang, F. & Melosh, N. A. Plasmonic energy collection through hot carrier extraction. *Nano letters* **11**, 5426–5430 (2011).

163. Mubeen, S. *et al.* An autonomous photosynthetic device in which all charge carriers derive from surface plasmons. *Nature nanotechnology* **8**, 247–251 (2013).

164. Frischkorn, C. & Wolf, M. Femtochemistry at metal surfaces: nonadiabatic reaction dynamics. *Chemical reviews* **106**, 4207–4233 (2006).

165. Inouye, H., Tanaka, K., Tanahashi, I. & Hirao, K. Ultrafast dynamics of nonequilibrium electrons in a gold nanoparticle system. *Physical Review B* **57**, 11334 (1998).

166. Bonn, M. *et al.* Ultrafast electron dynamics at metal surfaces: Competition between electron-phonon coupling and hot-electron transport. *Physical Review B* **61**, 1101 (2000).

167. Narang, P., Sundararaman, R. & Atwater, H. A. Plasmonic hot carrier dynamics in solid-state and chemical systems for energy conversion. *Nanophotonics* **5**, 96–111 (2016).

168.   Zhang, Y. *et al.* Surface-plasmon-driven hot electron photochemistry. *Chemical reviews* **118**, 2927–2954 (2017).

169.   Huang, X. & El-Sayed, M. A. Gold nanoparticles: Optical properties and implementations in cancer diagnosis and photothermal therapy. *Journal of advanced research* **1**, 13–28 (2010).

170.   Baffou, G. & Quidant, R. Thermo-plasmonics: using metallic nanostructures as nano-sources of heat. *Laser & Photonics Reviews* **7**, 171–187 (2013).

171.   Zamponi, F. *et al.* Probing the dynamics of plasmon-excited hexanethiol-capped gold nanoparticles by picosecond X-ray absorption spectroscopy. *Physical Chemistry Chemical Physics* **16**, 23157–23163 (2014).

172.   Kotaidis, V. & Plech, A. Cavitation dynamics on the nanoscale. *Applied Physics Letters* **87**, 213102 (2005).

173.   Auböck, G. *et al.* Femtosecond pump/supercontinuum-probe setup with 20 kHz repetition rate. *Review of Scientific Instruments* **83**, 093105 (2012).

174.   Baum, P., Lochbrunner, S. & Riedle, E. Zero-additional-phase SPIDER: full characterization of visible and sub-20-fs ultraviolet pulses. *Opt. Lett., OL* **29**, 210–212 (2004).

175.   Boriskina, S. V. *et al.* Losses in plasmonics: from mitigating energy dissipation to embracing loss-enabled functionalities. *Advances in Optics and Photonics* **9**, 775–827 (2017).

176.   Irani, G. B., Huen, T. & Wooten, F. Optical properties of gold and α-phase gold-aluminum alloys. *Physical Review B* **6**, 2904 (1972).

177.   Zhao, J. *et al.* A Comparison of Photocatalytic Activities of Gold Nanoparticles Following Plasmonic and Interband Excitation and a Strategy for Harnessing Interband Hot Carriers for Solution Phase Photocatalysis. *ACS Cent. Sci.* **3**, 482–488 (2017).

178.   García, M. A. Surface plasmons in metallic nanoparticles: fundamentals and applications. *Journal of Physics D: Applied Physics* **44**, 283001 (2011).

179.   Mongin, D. *et al.* Ultrafast electron-lattice thermalization in copper and other noble metal nanoparticles. *Journal of Physics: Condensed Matter* **31**, 084001 (2019).

180.   Baldini, E. *et al.* Phonon-driven selective modulation of exciton oscillator strengths in anatase TiO2 nanoparticles. *Nano letters* **18**, 5007–5014 (2018).

181.   Sakai, N. & Tatsuma, T. Photovoltaic Properties of Glutathione-Protected Gold Clusters Adsorbed on TiO2 Electrodes. *Advanced Materials* **22**, 3185–3188 (2010).

182.   Matthey, D. *et al.* Enhanced bonding of gold nanoparticles on oxidized TiO2 (110). *Science* **315**, 1692–1696 (2007).

183.   Ng, C. *et al.* Hot carrier extraction with plasmonic broadband absorbers. *ACS nano* **10**, 4704–4711 (2016).

184.   Lee, Y. K. *et al.* Surface plasmon-driven hot electron flow probed with metal-semiconductor nanodiodes. *Nano letters* **11**, 4251–4255 (2011).

185. Boriskina, S. V., Zhou, J., Hsu, W.-C., Liao, B. & Chen, G. Limiting efficiencies of solar energy conversion and photo-detection via internal emission of hot electrons and hot holes in gold. in *Infrared Remote Sensing and Instrumentation XXIII* vol. 9608 960816 (International Society for Optics and Photonics, 2015).

186. Shiraishi, Y. *et al.* Quantum tunneling injection of hot electrons in Au/TiO2 plasmonic photocatalysts. *Nanoscale* **9**, 8349–8361 (2017).

187. Rühle, S. & Cahen, D. Electron Tunneling at the TiO2/Substrate Interface Can Determine Dye-Sensitized Solar Cell Performance. *J. Phys. Chem. B* **108**, 17946–17951 (2004).

188. Cortés, E. *et al.* Plasmonic hot electron transport drives nano-localized chemistry. *Nature communications* **8**, 1–10 (2017).

189. Link, S. & El-Sayed, M. A. Optical properties and ultrafast dynamics of metallic nanocrystals. *Annual review of physical chemistry* **54**, 331–366 (2003).

190. Wray, J. H. & Neu, J. T. Refractive Index of Several Glasses as a Function of Wavelength and Temperature*. *J. Opt. Soc. Am.* **59**, 774 (1969).

191. Schiebener, P., Straub, J., Levelt Sengers, J. M. H. & Gallagher, J. S. Refractive index of water and steam as function of wavelength, temperature and density. *Journal of physical and chemical reference data* **19**, 677–717 (1990).

192. Brorson, S. D. *et al.* Femtosecond Room-Temperature Measurement of the Electron-Phonon Coupling Constant-Lambda in Metallic Superconductors. *Phys Rev Lett* **64**, 2172–2175 (1990).

193. Mihailidi, M., Xing, Q., Yoo, K. M. & Alfano, R. R. Electron-phonon relaxation dynamics of niobium metal as a function of temperature. *Phys. Rev. B* **49**, 3207–3212 (1994).

194. Groeneveld, R. H. M., Sprik, R. & Lagendijk, A. Femtosecond spectroscopy of electron-electron and electron-phonon energy relaxation in Ag and Au. *Phys. Rev. B* **51**, 11433–11445 (1995).

195. Schoenlein, R. W., Lin, W. Z., Fujimoto, J. G. & Eesley, G. L. Femtosecond studies of nonequilibrium electronic processes in metals. *Physical Review Letters* **58**, 1680 (1987).

196. Baldini, E., Palmieri, T., Pomarico, E., Auböck, G. & Chergui, M. Clocking the Ultrafast Electron Cooling in Anatase Titanium Dioxide Nanoparticles. *ACS Photonics* **5**, 1241–1249 (2018).

197. Wang, L. *et al.* Slow Charge Carrier Relaxation in Gold Nanoparticles. *J. Phys. Chem. C* (2020) doi:10.1021/acs.jpcc.0c07755.

198. Ratchford, D. C., Dunkelberger, A. D., Vurgaftman, I., Owrutsky, J. C. & Pehrsson, P. E. Quantification of Efficient Plasmonic Hot-Electron Injection in Gold Nanoparticle–TiO2 Films. *Nano letters* **17**, 6047–6055 (2017).

199. Hattori, Y., Gutiérrez Álvarez, S., Meng, J., Zheng, K. & Sá, J. Role of the Metal Oxide Electron Acceptor on Gold–Plasmon Hot-Carrier Dynamics and Its Implication to Photocatalysis and Photovoltaics. *ACS Applied Nano Materials* (2021).

200.   Prabhakaran, P., Kim, T. D. & Lee, K. S. 8.09 - Polymer Photonics. in *Polymer Science: A Comprehensive Reference* (eds. Matyjaszewski, K. & Möller, M.) 211–260 (Elsevier, 2012). doi:10.1016/B978-0-444-53349-4.00207-7.

201.   Watanabe, Y., Ohnishi, M. & Tsuchiya, T. Measurement of nonlinear absorption and refraction in titanium dioxide single crystal by using a phase distortion method. *Applied physics letters* **66**, 3431–3432 (1995).

202.   Morton, S. M., Silverstein, D. W. & Jensen, L. Theoretical studies of plasmonics using electronic structure methods. *Chemical reviews* **111**, 3962–3994 (2011).

203.   Hu, Z. & Jensen, L. A Discrete Interaction Model/Quantum Mechanical Method for Simulating Plasmon-Enhanced Two-Photon Absorption. *Journal of Chemical Theory and Computation* **14**, 5896–5903 (2018).

204.   Jakob, M., Levanon, H. & Kamat, P. V. Charge Distribution between UV-Irradiated TiO2 and Gold Nanoparticles: Determination of Shift in the Fermi Level. *Nano Lett.* **3**, 353–358 (2003).

205.   Tan, T. H. *et al.* Understanding plasmon and band gap photoexcitation effects on the thermal-catalytic oxidation of ethanol by TiO2-supported gold. *ACS catalysis* **6**, 1870–1879 (2016).

206.   Uthe, B., Collis, J. F., Madadi, M., Sader, J. E. & Pelton, M. Highly Spherical Nanoparticles Probe Gigahertz Viscoelastic Flows of Simple Liquids Without the No-Slip Condition. *The Journal of Physical Chemistry Letters* **12**, 4440–4446 (2021).

207.   Lamb, H. On the vibrations of an elastic sphere. *Proceedings of the London Mathematical Society* **1**, 189–212 (1881).

208.   Tamura, A., Higeta, K. & Ichinokawa, T. Lattice vibrations and specific heat of a small particle. *Journal of Physics C: Solid State Physics* **15**, 4975 (1982).

209.   Vardeman, C. F., Conforti, P. F., Sprague, M. M. & Gezelter, J. D. Breathing mode dynamics and elastic properties of gold nanoparticles. *The Journal of Physical Chemistry B* **109**, 16695–16699 (2005).

210.   Mongin, D. *et al.* Acoustic vibrations of metal-dielectric core–shell nanoparticles. *Nano letters* **11**, 3016–3021 (2011).

211.   Sun, C. & Smith, S. C. Strong Interaction between Gold and Anatase TiO2(001) Predicted by First Principle Studies. *J. Phys. Chem. C* **116**, 3524–3531 (2012).

212.   Du, X. *et al.* Size-dependent strong metal-support interaction in TiO 2 supported Au nanocatalysts. *Nature communications* **11**, 1–8 (2020).

213.   Del Fatti, N., Voisin, C., Chevy, F., Vallée, F. & Flytzanis, C. Coherent acoustic mode oscillation and damping in silver nanoparticles. *The Journal of chemical physics* **110**, 11484–11487 (1999).

214.   Pelton, M. *et al.* Damping of acoustic vibrations in gold nanoparticles. *Nature nanotechnology* **4**, 492–495 (2009).

Curriculum Vitae

Lijie Wang

Lab. of Ultrafast Spectroscopy (LSU)

EPFL SB ISIC LSU CH H1 545

CH-1015 Lausanne, Switzerland

Citizenship: Chinese

Birth: March 5th, 1991

Phone: +41 786963906

Email: lijie.wang@epfl.ch

wanglijie01@hotmail.com (personal)

Education

PhD in **Photonics**, under the supervision of Prof. Majed Chergui, *École Polytechnique Fédérale de Lausanne (EPFL),* Switzerland (2017.01 ~ present)

M. S. in **Material Science**, under the supervision of Prof. Guosheng Shao and Prof. Junhua Hu, B. S. in **Materials Science and Engineering**, second degree in **Business Management**, *Zhengzhou University*, China (Combined Bachelor-Master's Degree Programme, 2010.09-2016.10)

Fields of Research

Photo-induced processes (charge carrier dynamics, charge transfer, thermal effects etc.) in metal oxide solar materials; Nano material; Time-resolved absorption spectroscopy

Honor and Awards

1. China Scholarship Council (CSC) Scholarship (2017-2020)

2. National Scholarship of Graduate Student in 2015

3. Merit Student of Henan Province in 2013 and 2014

4. Outstanding Graduate Research Award in 2014, 2015.

Publications

1. Wang L., Zare D., Chow T. C., Wang J., Magnozzi M. and Chergui M., 'Disentangling Light- and Temperature-induced Thermal Effects in Colloidal Au Nanoparticles', *submitted*, **2021**.

2. <u>Wang L.</u>, Chow T. C., Oppermann, M., Bauer B., Wang J., and Chergui M., 'Acoustic Vibrations in Gold Nano-sphere Probing via Inter-band Transition', *draft*, **2021**

3. <u>Wang L.</u>, Rossi, T.C., Oppermann, M., Bauer B., Chow T.H., Wang J., Chergui M., 'Plasmon-mediated Two-photon Transition and Charge Transfer in (Au-core)/(TiO$_2$-shell) Nanoparticles', *draft,* **2021**.

4. Rossi T.C., <u>Wang L.</u>, Guo T. and Chergui M., 'Mapping Simultaneously the Electron and Hole Dynamics in Organic-inorganic Lead-halogen Perovskites by Ultrafast Deep-UV spectroscopy', *draft,* **2021**

5. <u>Wang L.</u>, Rossi, T.C., Oppermann, M., Bauer B., Mewes, L., Zare D., Chow T.H., Wang J., Chergui M., 'Slow Charge Carrier Relaxation in Gold Nanoparticles', *The Journal of Physical Chemistry C* 124.44 **2020**: 24322-24330.

5. Rossi, T.C., <u>Wang, L.</u>, Oppermann, M., Chen, P., Chiang, Y.H., Tsai, M.C., Shih, C.H., Guo, T.F. and Chergui, M., 'Cooling dynamics of electrons in MAPbBr$_3$ probed in the deep-UV', *Proceedings of the XXIst International Conference on Ultrafast Phenomena.* **2019**.

6. <u>Wang, L.</u>, Zhang, X., Gao, H., Hu, J., Mao, J., Liang, C., Zhang, P. and Shao, G., '3D CuO Network Supported TiO$_2$ Nanosheets with Applications for Energy Storage and Water Splitting', *Science of Advanced Materials* **2016**, 8, 1256-1262.

7. Hu, J., <u>Wang, L.</u>, Zhang, P., Liang, C., Shao, G., 'Construction of solid-state Z-scheme carbon-modified TiO$_2$/WO$_3$ nanofibers with enhanced photocatalytic hydrogen production', *Journal of Power Sources* **2016**,328, 28-36.

8. Zhang, P., <u>Wang, L.</u>, Zhang, X., Shao, C., Hu, J. and Shao, G., 'SnO$_2$-core carbon-shell composite nanotubes with enhanced photocurrent and photocatalytic performance', *Applied Catalysis B: Environmental* **2015**, 166-167, 193-201.

9. Zhang, P., <u>Wang, L.</u>, Zhang, X., Hu, J. and Shao, G., 'Three-dimensional Porous Networks of Ultra-long Electrospun SnO$_2$ Nanotubes with High Photocatalytic Performance', *Nano-Micro Letters* **2015**, 7(1), 86-95. (cover picture)

Teaching activities

ChE-349 Experimental physical chemistry

– Dr. MER Marcel Drabbels - Spring semester 2018

PHYS-724 Ultrafast phenome

– Dr. Barillot Thomas Roland and Prof. Chergui Majed – Fall semester 2018

ChE-320 Bioreactor modeling and simulation

– Prof. Hatzimanikatis Vassily – Spring semester 2019

CH-417 Optical methods in chemistry

– Prof. Christoph Bostedt- Fall semester 2019

ChE-340 The engineering of chemical reactions

– Prof. Albert Renken – Spring semester 2020

Miscellaneous

Languages – Chinese (mother tongue), English

Computer Skills – Origin Lab, Adobe Illustrator, Matlab etc.